Object Surface Exploration Using a Tactile-Enabled Robotic Fingertip

by

Bruno Monteiro Rocha Lima

Thesis submitted to the
Faculty of Graduate and Postdoctoral Studies
In partial fulfillment of the requirements
For the M.A.Sc. degree in
Biomedical Engineering

School of Electrical Engineering and Computer Science
Faculty of Engineering
University of Ottawa

Abstract

Exploring surfaces is an essential ability for humans, allowing them to interact with a large variety of objects within their environment. This ability to explore surfaces is also of a major interest in the development of a new generation of humanoid robots, which requires the development of more efficient artificial tactile sensing techniques. The details perceived by statically touching different surfaces of objects not only improve robotic hand performance in force-controlled grasping tasks but also enables the feeling of vibrations on touched surfaces. This thesis presents an extensive experimental study of object surface exploration using biologically-Inspired tactile-enabled robotic fingers.

A new multi-modal tactile sensor, embedded in both versions of the robotic fingertips (similar to the human distal phalanx) is capable of measuring the heart rate with a mean absolute error of 1.47 bpm through static explorations of the human skin.

A two-phalanx articulated robotic finger with a new miniaturized tactile sensor embedded into the fingertip was developed in order to detect and classify surface textures. This classification is performed by the dynamic exploration of touched object surfaces. Two types of movements were studied: one-dimensional (1D) and two-dimension (2D) movements. The machine learning techniques - Support Vector Machine (*SVM*), Multilayer Perceptron (*MLP*), *Random Forest*, *Extra Trees*, and k-Nearest Neighbors (*kNN*) - were tested in order to find the most efficient one for the classification of the recovered textured surfaces. A 95% precision was achieved when using the *Extra Trees* technique for the classification of the 1D recovered texture patterns. Experimental results confirmed that the 2D textured surface exploration using a hemispheric tactile-enabled finger was superior to the 1D exploration.

Three exploratory velocities were used for the 2D exploration: 30 mm/s, 35 mm/s, and 40 mm/s. The best classification accuracy of the 2D recovered texture patterns was 99.1% and 99.3%, using the *SVM* classifier, for the two lower exploratory velocities (30 mm/s and 35mm/s), respectively. For the 40 mm/s velocity, the *Extra Trees* classifier provided a classification accuracy of 99.4%.

The results of the experimental research presented in this thesis could be suitable candidates for future development.

Acknowledgements

I would like to acknowledge Dr. Emil Petriu for all his insights and for giving me the opportunity to work at the BioIn Robotics lab. I also would like to express my sincere gratitude to all the members of the BioIn Robotics lab. In special Thiago, that guided me with the experiments and with my thesis, and Vinicius that provided me thoughtful ideas and profound discussions. I am extremely appreciative of Alicia, my girlfriend, that stayed up with me, proofreading every word that I wrote in this thesis. She also gave me the emotional support that I needed to finish this work. I am thankful for my mother, Penha, that never stopped believing in me. Without her, I would not have grown so much. Thanks to my brothers and my father, that I know that love me. I cannot forget about Matheus and Hugo, that helped me with the dynamic exploration experiments, and Luiz, that helped me with the heart rate codding. I also would like to recognize Chase, that helped with my entry application process at the University of Ottawa.

Table of Contents

List of Tables

List of Figures

Nomenclature

Abbreviations

ANNs	Artificial Neural Networks
DOF	Degrees of Freedom
DWT	Discrete Wavelet Transform
ECGs	Electrocardiograms
GMM	Gaussian Mixture Models
IMU	Inertial Measurement Unit
kNN	k-Nearest Neighbors
MAE	Mean Absolute Error
MARG	Magnetic, Angular Rate, and Gravity
MEMS	Micro-Electro-Mechanical Systems
MLP	Multilayer Perceptron
PCA	Principal Component Analysis
RBF	Radial Basis Function
REB	Research Ethics Board
ROS	Robotic Operating System
SVM	Support Vector Machine

Chapter 1

Introduction

> “ *In a way, touch can be constructed as the most reliable of the [human] sensor modalities. When the senses conflict, touch is usually the ultimate arbiter. [...] Touch sensations can arise from stimulation anywhere on the body surface. Indeed, the skin can be characterized as one large receptor surface for the sense of touch. [...] The English neurologist H. Jackson paid homage to the wonderful and complex abilities of the human hand by calling it the most intelligent part of the body. The skin on the human hand contains thousands of mechanoreceptors (sensitive to mechanical pressure of deformation of the skin), as well as a complex set of muscles to guide the fingers as they explore the surface of an object. The mechanoreceptors play a key role in analyzing object detail such as texture; the muscles make their big contribution when grosser features such as size, weight, and shape are being analyzed. But, whether exploring gross or small details, the hand and the finger pads convey the most useful tactile information about objects. In this respect, the hand is analogous to the eye's fovea, the region of the retina associated with keen visual acuity. There is, however, a flaw in this analogy: fovea vision is most acute when the eye is relatively stationary, but touch acuity is best*

> *when the fingers move of the object of regard.* ”
>
> [1] R. Sekuler, R. Balke, *Perception*, 2nd edition, McGraw-Hill, 1990, NY, Chapter 11. Touch, pp. 357-383

Touch is a critical component in the functionality of human physiology. The capacity of the somatosensation (sense of touch), allows for an organism to respond accordingly within a given environment to various stimuli. Without a sense of touch, animals are not able to perform specific tasks effectively. From a study conducted in 1982, researchers investigated the manual motor functions in a man that had incomplete afferent connections with his central nervous system; thereby, rendering his motor skills ineffective. The study conducted by this study were considered a success; however, without the ability of touch feeling, he was unable to perform simple daily tasks such as buttoning a shirt, writing with a pen, or holding a cup [2]. In 1984, another study provided evidence on how a human's grasping performance is directly related to tactile feedback. In this study, human subjects had their fingertips anesthetized and were asked to perform a stable grasp by holding an object. The researchers determined that a subject's performance was dependent on tactile feedback [3]. A common consensus remains from which newer and older studies agree that somesthetic loss can result in catastrophic impairments. For instance, dexterity, limb position, and haptic capabilities can directly impact daily tasks. Additionally, an interesting question was proposed: "What would be worse, losing your sight or your sense of touch?". The article discusses that vision alone cannot wholly compensate for the loss of touch, suggesting that tactile sensing functions are significant in both virtual and real environments [4].

Evidence from previous and recent studies have demonstrated that humans perform poorly without tactile feedback. Similarly, robotic systems appear to have limitations that could be solved by introducing a tactile feedback system. For robots to perform similarly, or at a more optimal level than humans, new biology-inspired tactile sensing and perception technologies are under development. This area of research is often called *biomimetics* or *biology-inspired*. In this thesis, an experimental biology-inspired tactile-enabled robotic finger technology was developed and used for different static and dynamic surface exploration applications.

1.1 Motivation

1.1.1 Why Exploring Surfaces is important?

From birth, the initial sensory exploration that a human performs is through touch. Humans are interacting with their environment every day, gathering and processing data by touching various objects. Distinctions between objects can be defined by feeling the object's texture and surface. When exploring objects, a human's innate response is to use touch. Hence, the process of exploring objects can be compared to processing and analyzing the haptic sensor data. Following on this idea, this thesis put into practice the concept of sensory feedback by gathering, processing, and analyzing data from human skin and textures.

Exploring surfaces is an essential physiological response for humans to effectively and accurately perceive objects within their environment. These biological functions can also be extended to robotic system operations. Such applications are directly related to how the robot will perceive and interact with its surroundings, aiding in various types of tasks. The exploration of surfaces can be used in static and dynamic tasks. The perception of surfaces by static touch helps in stable grasping tasks, manipulation control, and gathering geometrical information of objects. Dynamic tactile interactive tasks aid in texture classification and surface profiling. However, the type of movement and velocity of motion are essential variables that must be studied in an exploration task.

Lastly, the inspiration of many tactile technologies stems from actual biological sensory processes. Thus, inspired by human haptic perception, this dissertation proposes a tactile-enabled robotic fingertip that is able to explore the environment. Furthermore, a study about static and dynamic explorations using the robotic fingertip is done by examining the surfaces of the human skin (heart rate measurement) and by investigating and classifying a set of commonly used textures.

1.1.2 Role of Tactile-Enabled Robotic Fingertips

In general, robotic arms consist of arm links connected by joints and end effectors, which are often rudimentary grippers. There are numerous situations that tactile feedback would be more advantageous than vision. For example, if a subject is asked to grasp a coin in a pocket containing a key, a piece of paper, and a coin, the vision system is of no use. In contrast, tactile feedback would allow the subject to differentiate between the three objects.

A tactile-enable robotic fingertip provides a complementary way to interact with the environment other than vision. Essentially, it is useful because of its various applications in robot-object interactions. Such applications include object recognition, surface profiling, textures classification, and stable grasping control by collecting its tactile feedback.

1.2 Problem definition

Currently, there are not yet commercially available robotic haptic systems that can be used for complex tasks. Moreover, the literature presents only early stages of haptic systems. Therefore, the following problems are addressed:

1. In general, robots, especially humanoid robots, need to have multi-modal tactile information about their environment to perform tasks with better accuracy.
2. Static and dynamic explorations are the basis of perceiving the robot surroundings and, therefore, need to be studied.
3. Experimental trials with multi-modal tactile systems need to be carried out in order to develop more efficient haptic technologies.

1.3 Objectives

The objectives of this dissertation are as follows:

1. Build an efficient tactile-enabled robotic fingertip;
2. Statically explore the skin-surface vibrations in order to measure the heart rate;
3. Dynamically explore and classify surface textures by performing a:
    - linear (1D sliding) motions;
    - bidimensional (2D sliding) motions.

1.4 Thesis Contributions

In this thesis, a multi-modal tactile-enabled robotic fingertip was built and used to explore surfaces. To create this system, a recently developed multi-modal tactile sensor [5] was built and later upgraded in order to perform a wider variety of tasks.

All contributions are directly related to the area of biological inspired robotic haptics.

1. A new miniaturized version of the multi-modal tactile sensor was built.
2. Two tactile-enabled robotic fingertips (distal finger phalanges) were designed and built. One fingertip had the first version of the multi-modal tactile sensor [5], embedded into it. The second fingertip had the miniaturized version of the new miniaturized tactile sensor.
3. The tactile-enabled robotic fingertips were used to measure the heart pulse rate by statically exploring the human skin vibrations while the fingertip maintains a fix relative position (not moving) on the human subject's skin.
4. A two-phalanx articulated robotic finger was designed and built with the miniaturized tactile sensor embedded into the fingertip. The robotic fingertip was used to detect and classify the textures of the dynamically explored object surface.

- Two types of fingertip movements were studied: a linear (one-dimensional) surface texture exploration, and a two-dimensional surface texture exploration.
- A hemispherical shape of the fingertip was used in order to enable a smoother 2D surface explorations.
- The influence of the velocity of the exploratory movements on the classification algorithm was studied.
- Different machine learning techniques were tested to classify the textures: Support Vector Machine (*SVM*), Multilayer Perceptron (*MLP*), *Random Forest*, *Extra Trees*, and K-Nearest Neighbors (*kNN*).

1.4.1 Publications Arising from this Thesis

The following conference proceedings publications have arisen from work presented in this thesis.

(1) Bruno Monteiro Rocha Lima, Thiago Eustaquio Alves de Oliveira, Vinicius Pradoda Fonseca, Qi Zhu, Miriam Goubran, Voicu Z. Groza, and Emil M. Petriu, "Heart Rate Detection Using a Miniaturized Multimodal Tactile Sensor," Proceedings of the 2019 IEEE International Symposium on Medical Measurements and Applications (MeMeA) [6] .

(2) Bruno Monteiro Rocha Lima, Luiz Claudio Carlos Ramos Sampaio, Thiago Eustaquio Alves de Oliveira, Vinicius Prado da Fonseca, and Emil M. Petriu, "Heart Rate Detection Using a Multimodal Tactile Sensor and a Z-score Based Peak Detection Algorithm," Proceedings of 2019 CMBEC42 - The 42nd Conference of the Canadian Medical and Biological Engineering Society, vol.42 [7].

(3) Bruno Monteiro Rocha Lima, Vinicius Prado da Fonseca, Thiago Eustaquio Alves de Oliveira, Qi Zhu, and Emil M. Petriu, "Dynamic Tactile Exploration for Texture Classification using a Miniaturized Multi-modal Tactile Sensor and Machine Learning." Submitted to the 2020 IEEE International Systems Conference (SysCon).

Furthermore, the author has also contributed to the following conference publications:

(4) Thiago Eustaquio Alves de Oliveira, Bruno Monteiro Rocha Lima, Ana-Maria Cretu, and Emil M. Petriu, "Tactile Profile Classification Using a Multimodal MEMs-Based Sensing Module," Proceedings of the 3^{rd} International Electronic Conference on Sensors and Applications (ECSA), 2016. [8] - this contribution was published before the research in this dissertation started.

(5) Vinicius Prado da Fonseca, Bruno Monteiro Rocha Lima, Thiago Eustaquio Alves de Oliveira, Qi Zhu, Voicu Z. Groza, and Emil M. Petriu, "In-Hand Telemanipulation Using a Robotic Hand and Biology-Inspired Haptic Sensing," Proceedings of the 2019 IEEE International Symposium on Medical Measurements and Applications (MeMeA). [9]

(6) Thiago Eustaquio Alves de Oliveira, Vinicius Prado da Fonseca, Bruno Monteiro Rocha Lima, Ana-Maria Cretu, and Emil M. Petriu, "End-Effector Approach Flexibilization in a Surface Approximation Task Using a Bioinspired Tactile Sensing Module," Proceedings of the 2019 IEEE International Symposium on Robotic and Sensors Environments (ROSE). [10]

(7) Qi Zhu, Vinicius Prado da Fonseca, Bruno Monteiro Rocha Lima, Mirian Goubran, Thiago Eustaquio Alves de Oliveira, and Emil M. Petriu, "Teleoperated Grasping Using a Robotic Hand and a Haptic-Feedback Data Glove," Submitted to the 2020 IEEE International Systems Conference (SysCon).

1.5 Thesis Organization - Summary of Chapters

In this section, an overview of the methodology, experimental tools, and devices are discussed.

Chapter 1: Introduction. The motivation, problem definitions, objectives, and a list of contributions are presented in this chapter. A list of the author's published and submitted papers is also provided.

Chapter 2: Literature Survey. This chapter starts with a list of essential definitions, followed by a comprehensive literature review on artificial tactile sensing. The human tactile sensing is discussed alongside the human's haptic perception, showing the functions of the four main mechanoreceptors located in the human hand. Afterwards, specific types of tactile exploratory movements are introduced. A literature survey regarding tactile sensors is presented, which provides information about the multi-modal tactile sensor used in this thesis. A discussion of the machine learning methodologies used for texture classification is also described. Finally, the research conducted by the BioIn Robotics lab concerning surface exploration and other approaches available in the literature used for texture recognition are displayed.

Chapter 3: Multi-modal Tactile-Enabled Robotic Finger for Static and Dynamic Exploration. This chapter discusses the components of the tactile-enabled robotic fingertip built for static exploration and the elements of the articulated tactile-enabled robotic finger used for dynamic explorations.

Chapter 4: Static Surface Exploration for Heart Rate Detection. Experiments on static exploration of the human skin, using two versions of a tactile-enabled fingertip, were conducted in this chapter. The heart rate was measured by placing the robotic fingertips on the carotid artery located on the neck. The heart rate measured provided a mean absolute error of 1.47 bpm, suggesting that the fingertips built are notably accurate.

Chapter 5: Dynamic Surface Exploration for Texture Classification. The dynamic exploration of commonly used fine textures was done in this chapter. The experiments were divided into two scenarios: one-dimensional and two-dimensional explorations. The first experiment used an articulated tactile-enabled robotic finger with a flat fingertip. The second experiment used the same finger, but with a semi-spherical fingertip. Three velocities were studied during the 2D exploration. Traditional machine learning techniques were used, producing highly accurate classification results.

Chapter 6: Conclusions and Future Work. Summarizes the results and contributions of the work presented in this dissertation: A detailed list of future work suggestions is also provided.

Chapter 2

Literature Survey

This chapter presents an overview of the relevant literature, the theoretical background, and the methodology that was used in this dissertation along with prior work contributions.

2.1 Important Definitions

Before discussing the relevant subjects pertaining to this thesis, the following relevant definitions are defined.

Biomimetics: the word derives from life and imitation. It refers to the transfer of ideas from biological models and systems to technology [11]. For instance, researchers focusing on tactile sensor development are trying to mimic human touch.

Phalanges: are the bones located in the human fingers. Three bones compose the phalanges: distal phalanx, middle phalanx, and proximal phalanx.

Distal Phalanx: is the most extreme bone located in the finger.

Middle Phalanx: is the bone that connects the distal phalanx to the proximal phalanx.

Robotic Fingertip (distal phalanx): is considered in this thesis as the extremity part of a robotic finger, similar to a distal phalanx.

Robotic Finger (middle/distal phalanges): is considered in this thesis as the middle and extreme part of a robotic finger, similar to the combination of a middle phalanx and a distal phalanx.

Haptic system: is a complex perceptual system, composed of two subsystems: *cutaneous* and *kinesthetic*. Haptic systems are typically related to manual explorations [12].

Cutaneous information: consists of pressure, vibration, and thermal sensor data. For instance, the data provided by the mechanoreceptors located in the skin can be translated as information about the surface of objects (shape, elasticity, texture) [13].

Kinesthetic information: consists of sensor data about the position and movement from muscles – for example, the information about velocity and position of the kinematic structure of the hand [13].

Touch: "sense by which the texture and other qualities of objects can be experienced when they come in contact with a part of the body surface, especially the tips of the fingers" [14].

Tactile Sensors: a device that provides information and measures properties of an object based on the contact between the sensor and the touched object [15].

Machine learning: is a subcategory of artificial intelligence. Its idea is to use algorithms in order to enhance the ability to identify patterns and make decisions with minimal human interaction.

Supervised Learning: part of machine learning that the target label is given. For example, in texture classification, each set of training data corresponds to a specific texture and, hence, has a specific label. The target label identifies the texture for the training process.

Unsupervised Learning: part of machine learning that the target label is not a priori given. This process examines the data and determines, by itself, which classes are present.

2.2 Sense of Touch

The sense of touch is responsible for the perception of objects through physical contact, mainly with the fingers. Unlike other senses, where the sensory organs are found in a specific area, the sense of touch can be perceived by sensory organs all over the skin [16]. Essentially, the information from the environment is perceived by mechanoreceptors located in the skin. The tactile information is sent to the brain via the peripheral nervous system. Depending on the area that the touch was perceived, the data travels to a specific location in the brain. The brain, then, transforms the signals into what humans understand as the sense of touch. A diagram summarizing how humans perceive the environment is displayed in Figure 2.1. The various areas of the brain dedicated to tactile processing data of each area of the body are presented in Figure 2.2.

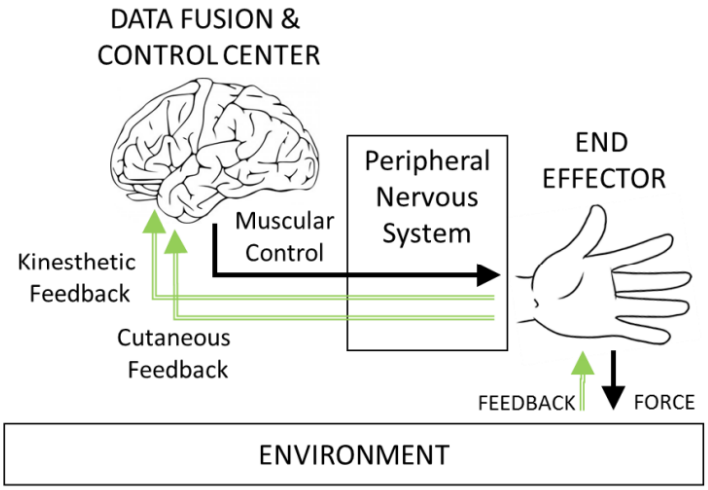

Figure 2.1: Tactile data flow [17].

2.3 Human Haptic Perception

Haptics is defined as a perceptual system, composed of the following subsystems: cutaneous and kinesthetic. Typically it is related to manual exploration [12]. The cutaneous system is responsible for the sense of touch and uses mechanoreceptors (sensory receptors) embedded

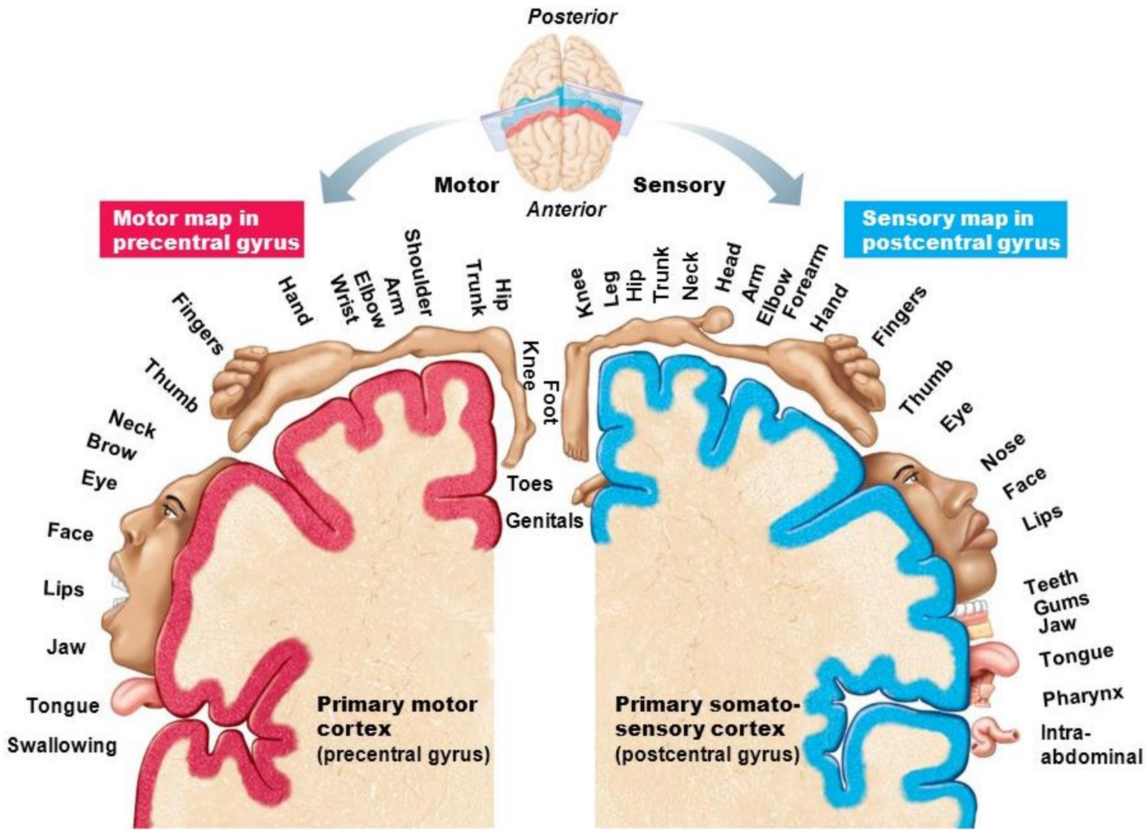

Figure 2.2: Body maps in the motor cortex and somatosensory cortex of the cerebrum [18].

in the skin to detect force, deformation, skin stretch, vibration, temperature, and pain. The kinesthetic system refers to the recognition of an individual's position and movement of various areas of their body. It uses the information from the mechanoreceptors in muscles, tendons, and joints to accurately measure the position and movement of the limb. A summary of each haptics subsystem functions and the mechanoreceptors associated with it is illustrated in Figure 2.3.

There are four main types of mechanoreceptors distributed within the skin that are responsible for cutaneous sensing [19]: Meissner?s corpuscles, Merkel?s discs, Pacinian corpuscles, and Ruffini corpuscles.

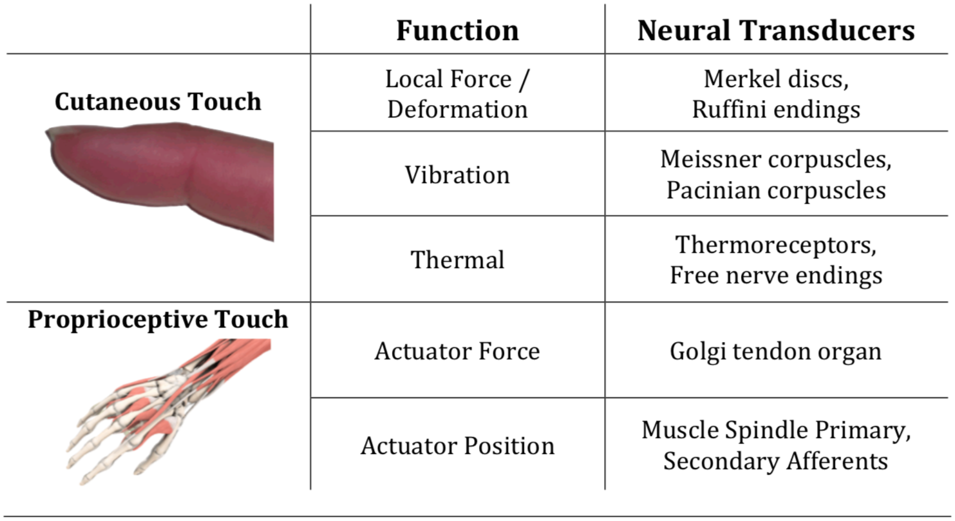

	Function	Neural Transducers
Cutaneous Touch	Local Force / Deformation	Merkel discs, Ruffini endings
	Vibration	Meissner corpuscles, Pacinian corpuscles
	Thermal	Thermoreceptors, Free nerve endings
Proprioceptive Touch	Actuator Force	Golgi tendon organ
	Actuator Position	Muscle Spindle Primary, Secondary Afferents

Figure 2.3: Human haptic subsystems, its functions and mechanoreceptors [20].

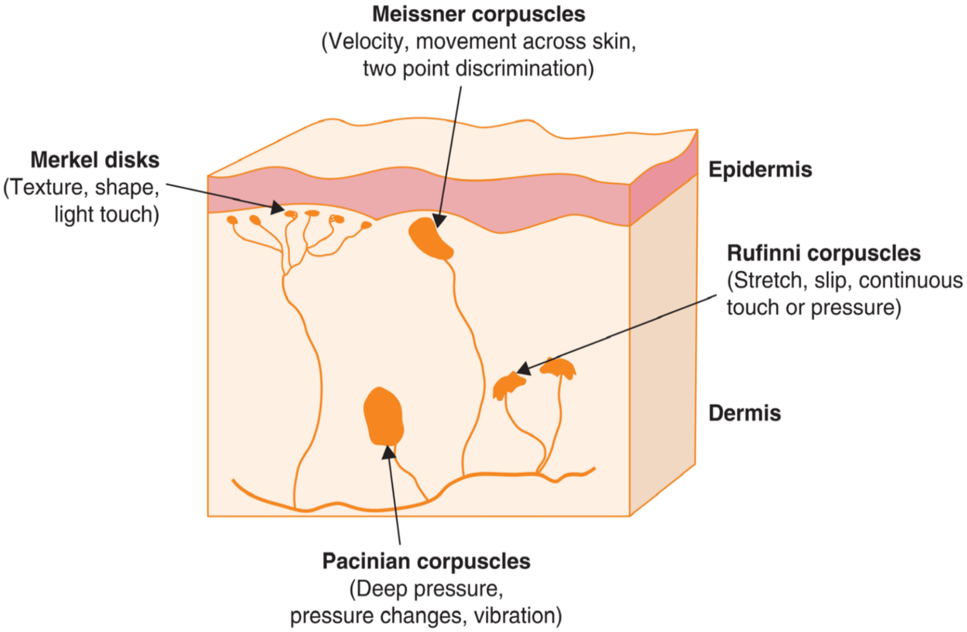

Figure 2.4: Location of the four main cutaneous mechanoreceptors in the skin (adapted from [15] and [21].

Meissner?s corpuscles are responsible for the detection of motion, velocity, slippage, low-frequency vibration, and local skin deformation. For the detection of shape, texture, and discrimination of fine surface detail discrimination, Merkel?s discs are used. The Pacinian corpuscles detect deep pressure, change of pressure, and high-frequency vibration. Finally, Ruffini corpuscles detect directional (lateral) skin stretch. Figure 2.4 illustrates the location of each of mechanoreceptors in the skin and Table 2.1 summarizes the functions of each mechanoreceptor. The knowledge about the physiology of cutaneous tactile sensing is highly relevant for the work presented in this thesis, as the tactile sensor used in this dissertation is biology-inspired.

Table 2.1: Properties and Functions of Mechanoreceptors [5]

Receptor	Location	Size	Functions
Merkel	Epidermis (shallow)	Small (2-3mm)	Detection of form, shape, texture, curvature, presence, constant pressure; fine details discrimination; location and static deformation at points and edges.
Meissner	Epidermis (shallow)	Small (3-5 mm)	Detection of motion, velocity, slippage, low frequency vibrations, local skin deformation, grip control, dynamic deformation; two-point discrimination; encode normal (horizontal) strain forces
Ruffini	Dermis (middle/ deep)	Large ($>$ 10 mm)	Directional (lateral) skin stretch; direction of object motion; position of hand and fingers; slip detection; stable grasp; tangential force estimation; tension (continuous touch or pressure)
Pacinian	Subcutis (deep)	Large ($>$ 20 mm)	Deep pressure; pressure change; unlocalized high frequency vibration; body contact when grasping an object (tool use)

It is clear by now that the mechanoreceptors are tightly bound to the haptic perception of surface and object properties. Humans can perform different exploratory movements in order to make contact and retrieve information about object shape, surfaces, textures, or the environment in general. The relation between the type of exploration and the object properties was studied by [22] and are summarized in Figure 2.5.

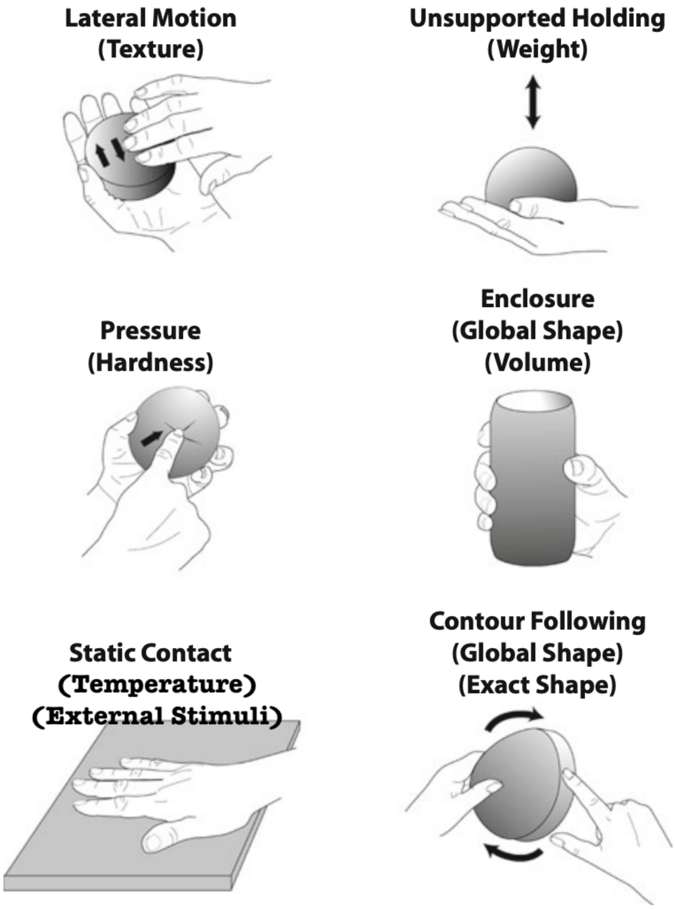

Figure 2.5: Six types of tactile exploratory movements (adapted from [23]).

The object exploration discussed in Chapter 4 used static contact to measure an external stimulus (the heart rate). The dynamic exploration and classification of textures, discussed in Chapter 5, performed a lateral motion. Dynamic exploration was conducted in two different experiments: one using a one-dimensional movement, and the other using a two-dimensional movement (following along the X and Y coordinates).

Different versions of a tactile-enabled robotic fingertip using a multi-modal tactile sensor (discussed in Section 2.4.3) and its miniaturized version (discussed in Section 3.1) were developed based on the cutaneous mechanoreceptors functions. Moreover, an articulated robotic finger was developed for dynamic exploration. The design of the robotic fingertip was based on the human distal phalanx, and the middle to the extremity of the finger (middle phalanx with distal phalanx) inspired the robotic finger, as shown in Figure 2.6.

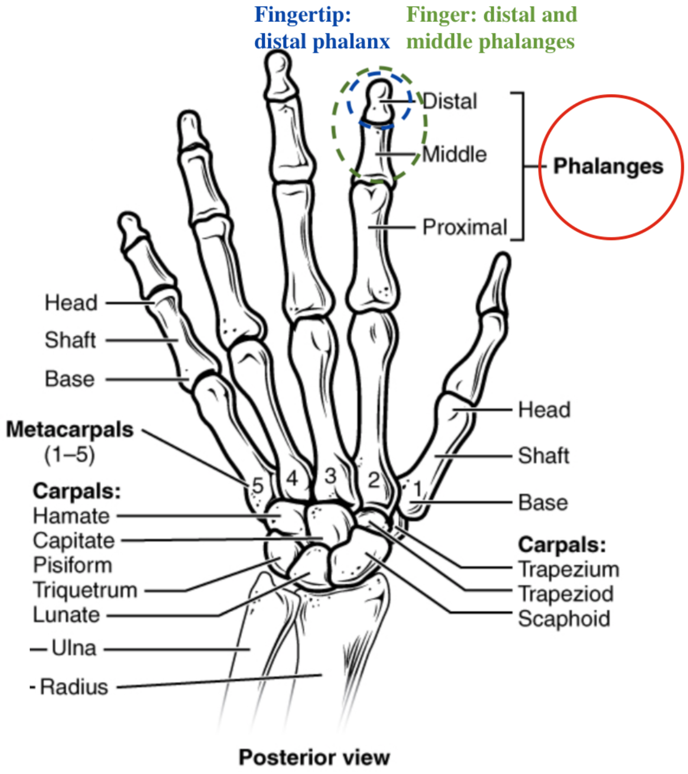

Figure 2.6: Fingers consist of the phalanx bones. The robotic fingertip was inspired in the distal phalanx, shown in the blue circle. The middle/distal phalanx inspired the articulated robotic finger, shown in the green circle. (adapted from [24]).

2.4 Artificial Tactile Sensing

2.4.1 Tactile Sensing in Robotics

Research regarding image processing has had great strides towards technology development, and it is widely used in many applications (e.g. object tracking, image processing, vision-guided systems). However, for decades, tactile sensing was lagging and just began to expand in the 1980?s [25, 26]. Its importance, however, should not be underestimated.

Within a given environment, human interaction is based on the feedback of different sensing modalities. For example, in order to perform a task such as grasping a key in a pocket full of coins, tactile feedback is required. Meanwhile, for differentiating two objects based on coloration, vision is needed. Tactile sensing needs to be explored in order to complement the interaction experience that robots have within its surroundings and allow it to perform more efficient tasks.

Tactile sensing is considered essential for survival, even for the simplest organisms. With a large number of mechanoreceptors, humans can react to stimuli within a given environment. The most important activities in sensing are manipulation, exploration and response [26].

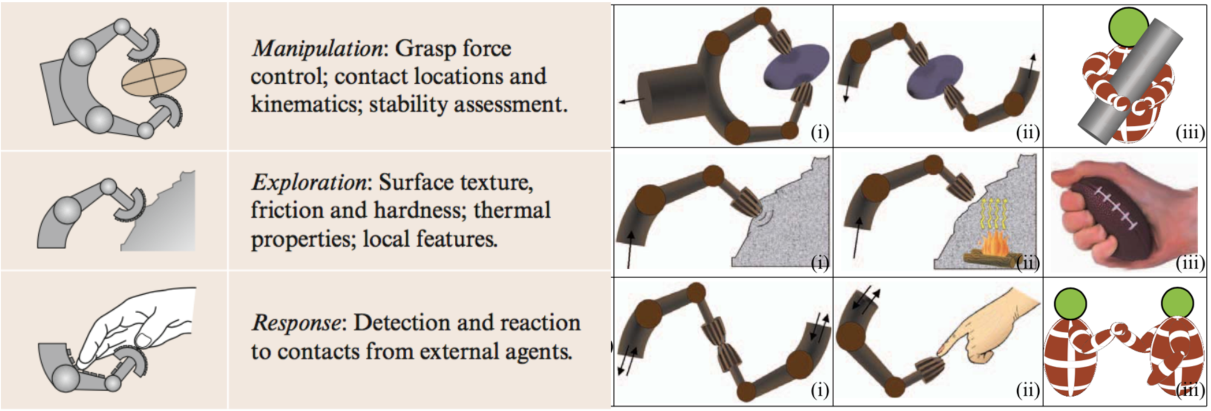

Figure 2.7: Tactile sensing in robotics. Manipulation: object manipulation by a robot or multiple robots with sensors over smaller (i), (ii) or larger areas (iii). Exploration: exploring objects to measure tactile features such as texture (i), temperature (ii), and softness/hardness (iii) etc. Response: where a robot or multiple robots react to a stimuli applied at a single contact point (i), (ii) or over larger areas (iii) (adapted from [25] and [26]).

As shown in Figure 2.7, the interaction is directed from the gripper towards the object in the manipulation phase. However, in exploration, the tactile information moves from the object towards the end-effector. In the response phase, the action-reaction cycle involves a bi-directional flow of the signal.

According to [27], controlling a robotic system may be simple if the robot actuators could move flawlessly, and if a complete model of the environment would be provided.

However, information about the environment is not often available and perfect control of motion is not realistic. Sensing is used for gathering information needed from the environment and the state of the robot system.

Robotic tasks often require physical contact with objects. Tactile sensing is fundamental for gathering action-related information (e.g. slip detection), manipulation parameters (e.g. grasping) and contact parameters (e.g. normal and shear contact forces, hardness, texture, temperature and slip) [25].

The process of robotic artificial tactile sensing is represented in Figure 2.8. Artificial sensing data is collected by the tactile systems embedded into the robot. Thereafter, the data are decoded and artificially perceived. The robot's actuator receives the tactile information and interacts with the environment accordingly. Sensor fusion is possible in artificial perception, but this thesis is focused only on artificial touching.

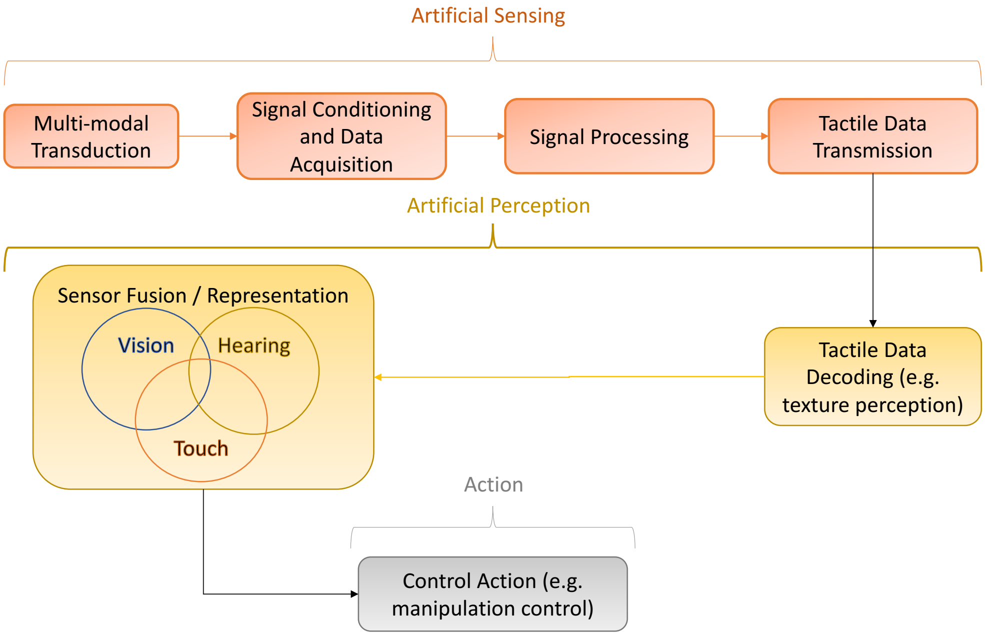

Figure 2.8: Representation of the robotic tactile sensing system (adapted from [28]).

It has been suggested that tactile feedback is essential for control, decision making and interaction with other agents in the environment and, therefore, has to be considered an important area of research in robotics [27].

2.4.2 Tactile Sensors

In recent years, a wide variety of tactile sensors using different materials, structures, and technologies have been proposed. Tactile sensors can be classified within three categories: (1) the transductor used; (2) the sensor material; and (3) the sensor structure [25].

Table 2.2: Tactile Sensor Classification [25]

Transduction	**Material**	**Structure**
Resistive [29–33]	Conductive Composites [34]	MEMS [35–37]
Capacitive [38–40]	Carbon Nano Tubes [41]	Silicon Transistors [42]
Optical [43–45]	Force Sensing Resistor [30]	Extended Gate Transistors [46]
Magnetic [47, 48]	Conductive Gels [49]	Organic Field Transistors [50]
Ultrasonic [51, 52]	Conductive Fibers [53]	Flexible Circuit Boards [43]
Piezoelectric [54–56]		
Electrorheological [57,58]		
Magnetorheological [59]		

Although different methods have been proposed for building tactile sensors, as shown in Table 2.2, their performance individually is not yet sufficient to be considered indispensable in robotic tasks. However, a tactile sensor's efficiency can be increased if the sensor has (1) high performance, e.g. sensitivity, (2) compliance, (3) reliable data processing & acquisition, and (4) efficient integration with the robot's structure.

Few tactile sensing technologies are commercially available. For instance; (a) Interlink Force Sensing Resistor®(FSR) are robust polymer thick film devices, that when force is applied to the surface of the sensor, it is inversely proportional to its resistance [60] (b) Teskan FlexiForce$^{\text{TM}}$ Force Sensors, uses pressure ink technology [61] (c) Peratech uses Quantum Tunnel Composites (QTC$^{®}$) technology [62] (d) RoboTouch and Digitacts capacitive touch sensors from Pressure Profile Systems (PPS) using non-silicon technology [63, 64] (e) SynTouch LLC BioTac SP conductive fluid-based that can measure skin deformation, vibration and temperature. [65].

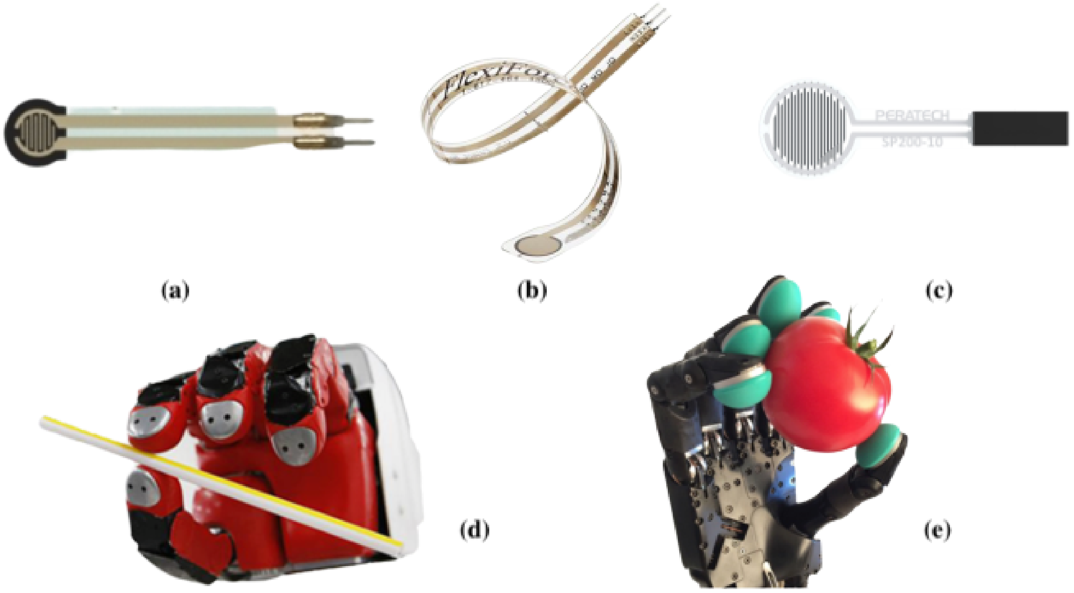

Figure 2.9: Commercially available tactile sensors. (a) FSR 400 model from Interlink [60] (b) Force Sensor from Teskan [61] (c) SP200-10 model from Peratech [62] (d) RoboTouch sensors integrated into a Human Symbiotic Robot [64], and (e) BioTac SP (Single Phalanx) sensors into an anthropomorphic robotic hand [65].

Besides these commercially available tactile sensors, some sensors were proposed in academic research. It should be noted that each sensor overcame a specific challenge in designing and prototyping a sensing module. A summary of challenges in designing a tactile sensor can be found in [25].

The work in [66] has proposed a bio-inspired tactile sensor with a spherical shell and a compliant structure made of silicone rubber. The purpose of its sensor was to measure the normal and shear forces from contact responses. The sensor has an embedded magnet on the top of the hollow hemisphere and four Hall-effect sensors arranged in a 2-by-2 matrix at the base of the dome. The Hall effect sensor output is used to calculate the height of the magnet (z-axis) and the displacements in the y-axis and x-axis. A study of the radius of the sensor was done in order to apply in different applications (e.g. smaller sensors for fingertips and bigger sensors for robot's forearm). The results indicated that an increase in the radius would increase the stiffness of the module, which results in less sensitivity. Hence, a smaller radius indicates higher sensitivity, allowing applications in robot fingertips. On the other hand, a greater radius indicates smaller sensitivity; thus, this sensor could be used on robotic arms. These results reinforce the reason for miniaturizing the sensor used in this dissertation (discussed in Section 3.1).

Other alternative methods were used to build tactile sensors. For instance, [30] developed a new type of tactile sensor using pressure-conductive rubber and a stitch technique in the electrical wires. A series of grasping operations were performed using a 4-fingered robot hand to test the sensor's applicability. Each finger had a matrix of 16-by-3 of pressure sensing modules. The objects used during the tests were a sphere and a cone.

A capacitive tactile sensor was implemented using polydimethylsiloxane (PDMS) layers for flexibility and compliance [38]. The sensor module consisted of a 16-by-16 matrix of tactile cells with a spatial resolution of 1 mm. Interconnection lines connected the modules. The authors presented an expanded version of the sensor by stitching four sensor modules using anisotropic conductive paste (ACP). Hence, these sensors could be potentially used in robotic arms.

Other proposed tactile sensors can be accessed in Table 2.2. However, a fully functional tactile sensor, able to recreate all the functions of the human skin, has not yet been done.

2.4.3 The Multi-Modal Tactile Sensor

The Multi-Modal Tactile sensor described in [5] was used for static exploration, discussed in Chapter 4. Moreover, based on its components, structure and functions, a Miniatured Multi-Modal Tactile Sensor, discussed in Chapter 3, was built and used for static and dynamic exploratory experiments.

The multi-modal tactile sensor is composed of a 9-DOF MARG (Magnetic, Angular Rate, and Gravity) sensor (also categorized as an Inertial Measurement Unit (IMU)), a flexible compliant structure similar to the human skin, and a deep pressure sensor. Its design was inspired by the location and functions of the cutaneous mechanoreceptors in the human skin.

The IMU sensors emulate the Merkel cells, Meissner corpuscles and Ruffini corpuscles.

Force magnitude, contact points and a rough orientation of the surface (measured by Merkel cells) are calculated by the IMU gravity field sensor (IMU). Vibrations can be calculated by the angular rate sensor embedded in the IMU. Form and stretch (measured by Ruffini corpuscles) can be calculated by the magnetic field sensor also embedded in the IMU. Finally, the pressure (measured by Pacinian corpuscles) are calculated by the barometer located in the lower level of the tactile module. It is crucial to notice that the transfer of pressure between the surface and the deep barometer is only possible because of the compliant cone structure of the sensor. Figure 2.10 shows the structure and components of the tactile module prototype. Tactile arrays, originally located on the top of the module, were not used in the experiments and, therefore, were removed from the prototype.

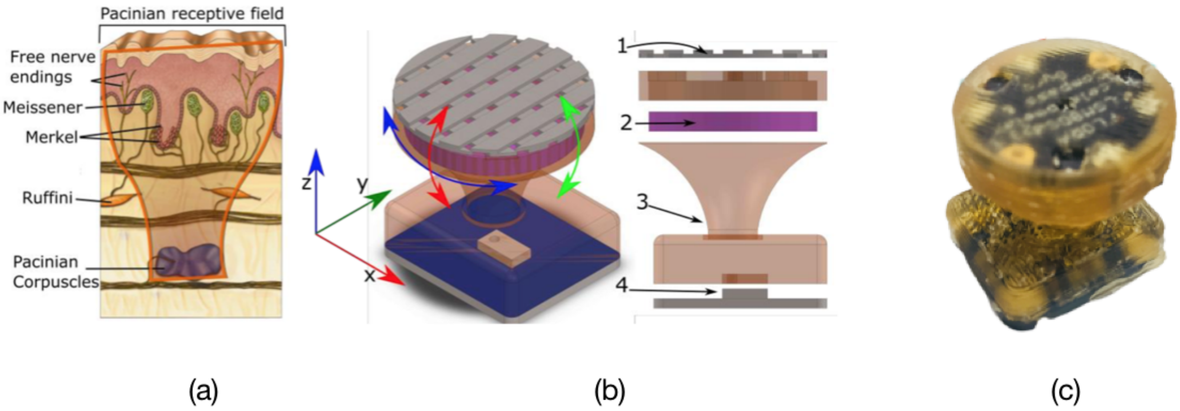

Figure 2.10: (a) Skin mechanoreceptors (b) Multi-Modal Tactile Sensor. 1 - tactile array; 2 - inertial measurement unit (IMU); 3 - cone compliant structure, and 4 - deep barometer; (c) Multi-modal sensor prototype (adapted from [5]).

The module has a compliant structure comprised of polyurethane rubber with the IMU and the barometer embedded into it. The tactile inverse problem [67] was solved by the cone structure that conducts the forces applied from the shallow sensors to the ventilation window of the deep pressure sensor. The compliant design allows the measurement of any stimuli inflicted on the top of the module.

Experiments with stimuli at a rate of 10 Hz, 0.5 Hz and 3 Hz were conducted in order to validate the sensor's performance. The presence of hysteresis was noticeable because of the compliance structure. Other experiments demonstrated the sensor?s capability to estimate surface angles and orientation.

Among all the sensors presented in Section 2.4.2, the device proposed by [5] proved to be the best candidate for emulating the mechanoreceptors functions and, hence, for being used on a robotic fingertip. The main advantage of this tactile module is its multi-modal sensing capacity, while most of the other tactile sensors are limited to the measurement of pressure. However, its application is still limited since the technique for expanding the module has not been yet developed. In this thesis, this module was miniaturized, upgraded and embedded in a robotic fingertip (discussed in Chapter 3).

2.5 Machine Learning - Classifiers

Artificial Neural Networks (ANNs) are becoming more popular in data-driven processes. Its idea is based on the human capability of acclimating to different circumstances within the environment. The initial objective of ANNs was to mimic some abilities of the human brain and has shown high potential in artificial learning [68]. Their application has become popular in fields like classification [69–71], which is the scope in this thesis, and other exciting areas like prediction of the power and energy needed to meet the demand and supply equilibrium [72–80], and medical applications and pattern recognition [81–83].

The classifiers used in this thesis are Multilayer Perceptron (*MLP*), Support Vector Machine (*SVM*), *Random Forest*, *Extra Trees*, and K-Nearest Neighbors (*kNN*). Even though not all classifiers listed are formally included in the ANNs category, its functionality is the same, and they all fall into the process of knowledge extraction through data-driven processes.

The process of knowledge extraction through data-driven processes is the core of the classification method used for texture discrimination in Chapter 5.

Data-driven classification process can be defined as the process of hierarchical classifications spurred from data and not from intuition or speculation. Its process is to analyze datasets by extracting information in the form of relationships and patterns. [84] Different methods and techniques can be used because many patterns exist in a database. Among the list of techniques known to be used (association, classification, clustering, summarization, and trend analysis), the one used is the classification method [85].

The classification method process is the following: given a set of objects, the method will organize each object into a class based on its attributes. In the case of the experiment presented in Chapter 5, a set of commonly used textures is given and labelled. Tactile data from the robotic fingertip is collected after a determined experiment, and this data is divided into two different sets: the training set and the testing set. Artificial learning is achieved when a classification function (known as a classifier) analyzes the training dataset to find relations between the data and the classes of each texture. Afterwards, the classifier is able to predict the texture's classes based on the testing dataset. The classification process using tactile data is illustrated in Figure 2.11.

2.5.1 Support Vector Machine (SVM) Classifier

Initially proposed by [86], the Support Vector Machine (SVM) classifier has been highly accepted in the area of classification methods and successfully demonstrated work on various classification applications. The algorithm is derived from guaranteed risk bounds [68].

Given the two groups of data points, as shown in Figure 2.12, the SVM selects a set of hyperplanes that separates one or more classes of objects. Among these, the classifier will select a hyperplane that has the most significant distance between the two sets of data, keeping an equal distance from each dataset.

Assuming that N data points samples are given in couples as $(\vec{x_1}, y_1), (\vec{x_2}, y_2), ...(\vec{x_N}, y_N)$, where $y_i \in \{1, -1\}$, representing the class that x_i belongs to.

The equation that represents a hyperplane for a set of points x_i is:

$$\vec{W} \cdot \vec{x} + b = 0 \tag{2.1}$$

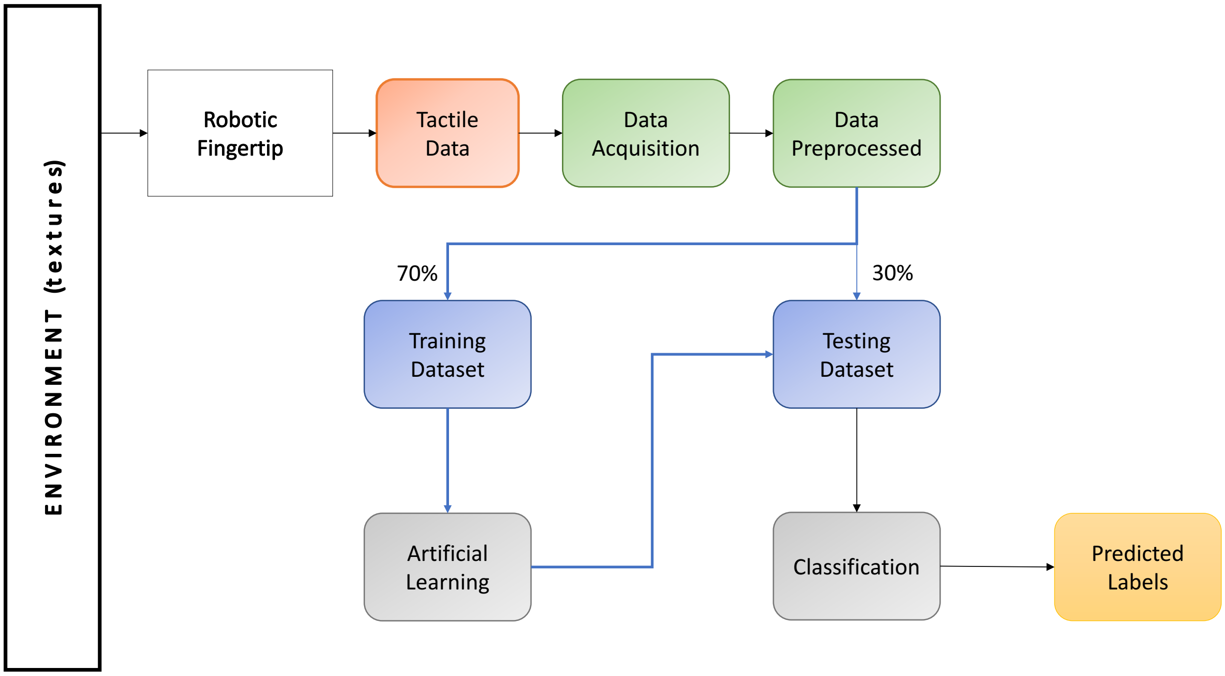

Figure 2.11: Classification process using tactile data. The information is gathered from the tactile module, then it is preprocessed and split in two groups: training (70%) and testing data (30%). The training data is used to teach the classifier and the testing data is used to make the predictions.

Where $\vec{W}$ is the normal vector to the hyperplane (hyperplane H), $\vec{x}$ is the training sample, and b is the bias. As said before, the margin between the two datasets should be maximized. Hence, the method requires to find the hyperplane that divides the group of data $y_i = 1$ from $y_i = -1$ for which the distance between the hyperplane and the nearest point $\vec{x_i}$ is maximized.

The solution to this problem can be accessed by [68] and more detailed in [87].

The *SVM* classifier is conveniently available in the *Scikit-Learn* Python library [88]. The Kernel functions (decision functions) available in the Python package are linear, polynomial, Radial Basis Function (RBF), and sigmoid. Figure 2.13 shows some examples of *SVM* classifications using the *Scikit-Learn* package. The SVM library has two important parameters to be defined when using the default kernel function (RBF): gamma, which is the parameter determining the range (radius) of the RBF, and C representing the weight

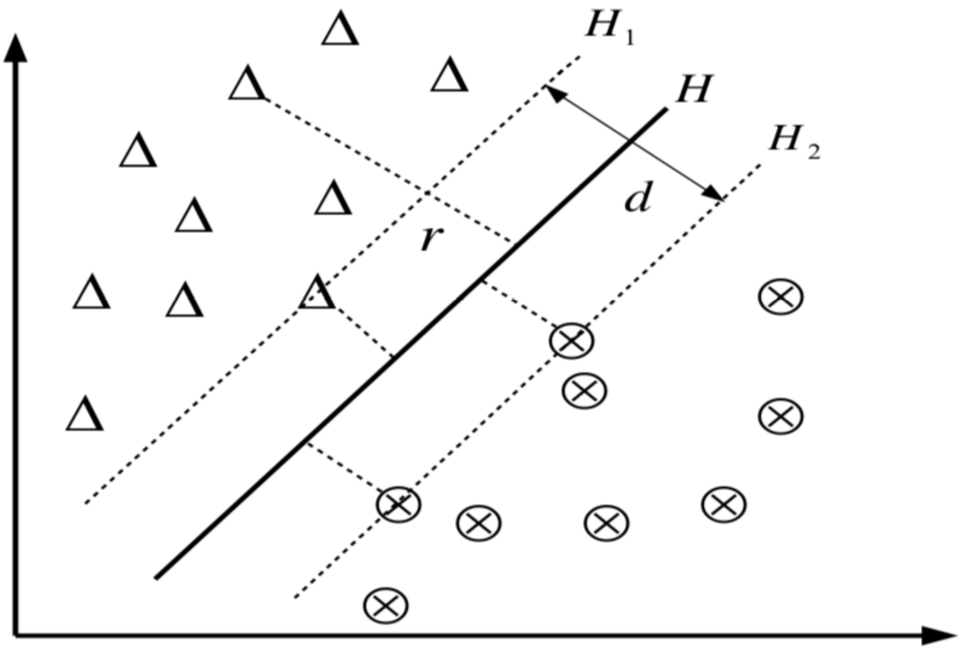

Figure 2.12: Linearly separable datasets. The Hyperplanes H_1 and H_2 are the margin of each dataset. Hyperplane H is the hyper plane chosen to separate the data [68].

of the error penalty term (regularization term).

Support Vector Machine classifiers are used for a variety of practical applications: texture classification [89], image classification [90], fingerprint classification [91], text classification [92, 93], general classifications [94–99], classification of magnetic resonance brain images [100] and medical applications, e.g. breast cancer diagnosis [101].

The advantages and disadvantages in using SVM classifier are [102]:

Advantages:

1. effective in high dimensional spaces;
2. effective if number of dimensions is greater than number of samples;
3. memory efficient;
4. different options can be used for the decision function (kernel functions).

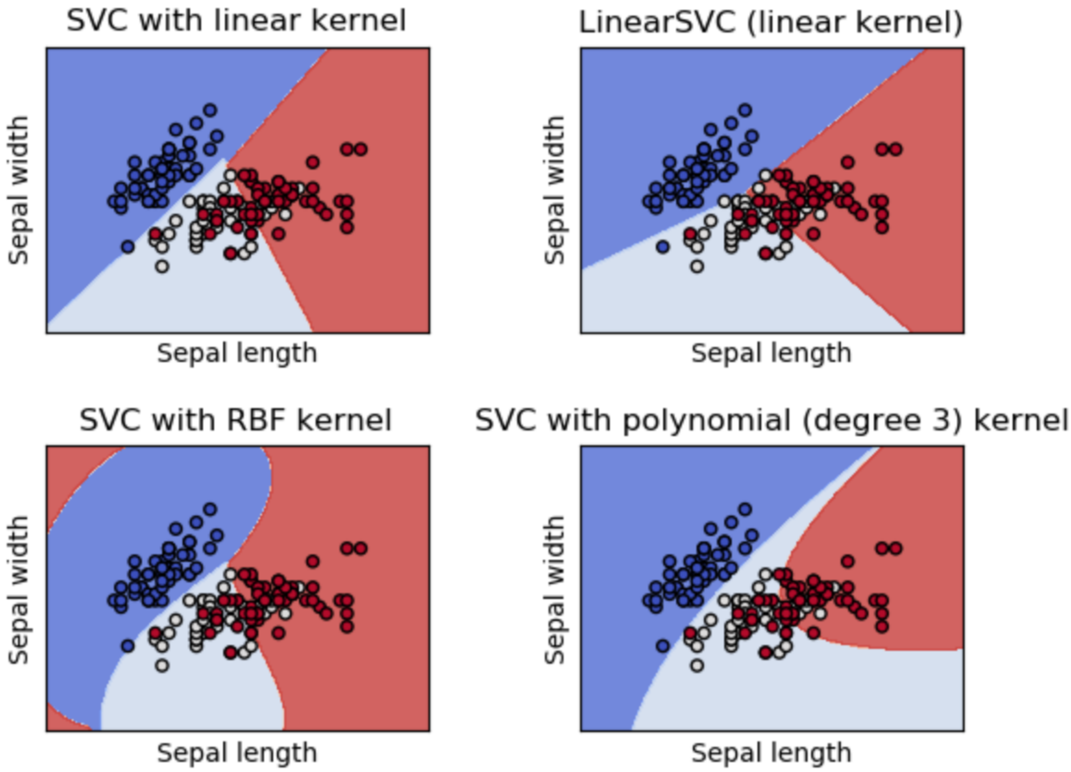

Figure 2.13: Multi-class classification of a dataset using SVM and different kernels functions [88].

Disadvantages:

1. choosing Kernel functions and regularization terms is crucial to avoid over-fitting.

2.5.2 Multilayer Perceptron (*MLP*) Classifier

The Multilayer Perceptron classifier is a Neural Network method that can be virtually trained to approximate any measurable function, by selecting a suitable set of connecting weights and transfer functions [103,104]. One advantage of using *MLP* is that no assumptions about the datasets are required, and it is applied with non-linear functions, which makes the *MLP* approach an attractive method in comparison to the traditional statistical techniques [105].

The *MLP* is a supervised learning algorithm that works by doing a non-linear mapping between the input dataset (features or input layer) and the output result (output layer) connected by artificial neurons (nodes), often called hidden layers of neurons. This configuration is shown in Figure 2.14. Each neuron is a weighted linear summation of its previous layer, and modified by a non-linear activation function (e.g. the hyperbolic tangent, $\frac{e^x - e^{-x}}{e^x + e^{-x}}$). This characteristic results in the superposition of several non-linear functions that enables the method to closely approximate to non-linear functions [105].

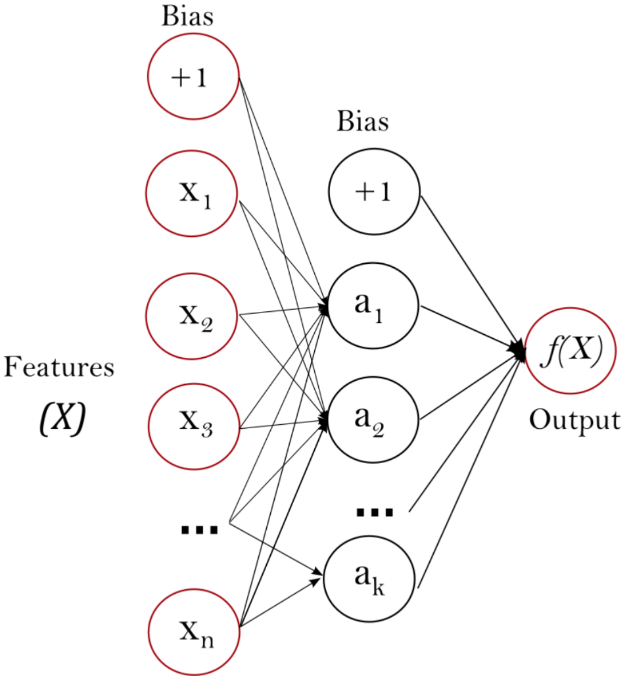

Figure 2.14: Multilayer Perceptron Neural Network with one hidden layer [106].

Given the input dataset (x_i) with its targets (y_i), $(x_1, y_1), (x_2, y_2) ... (x_n, y_n)$, where $y_i \in \{0, 1\}$, the neuron *MLP* learns by the following function [106]:

$$f(x) = W_2 g(W_1^T x + b_1) + b_1 \tag{2.2}$$

where W_1 and W_2 are weights of the input and hidden layer, respectively, b_1, b_2 are the bias added, and g is the activation function given by $g(x) = \frac{e^x - e^{-x}}{e^x + e^{-x}}$.

One of the *MLP* parameters is the L2 regularization, α, which determines the size of the weights, preventing overfitting or underfitting. A higher alpha induces smaller weights and prevents overfitting, while a smaller alpha translates to higher weights and prevents underfitting.

A convenient way to use the *MLP* method is offered by the Python *Scikit-Learn* library. Figure 2.15 displays the usage of the *MLP* technique with different values of the regularization term, α.

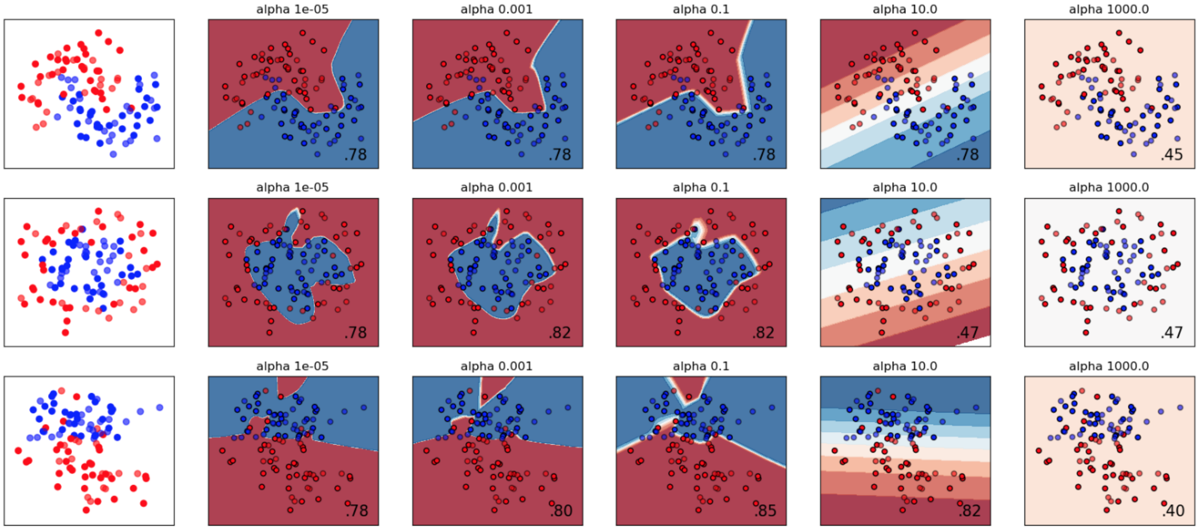

Figure 2.15: Different values of regularization parameter α from the *MLP* method being used to classify a set of data. Adapted from [106]

The advantages and disadvantages of the *MLP* classifier are the following:

Advantages:

1. easy to work with non-linear models.

Disadvantages:

1. different initialization weights can lead to different results.

2. selecting parameters (crucial for accurate classifications) such as the number of hidden layers, number of neurons in each layer, and number of interactions can be challenging.

In order to prevent overfitting, the *Scikit-Learn* library allows a regularization term (α or L2 penalty) to be added to the loss function. Its default value is 0.0001.

2.5.3 k-Nearest Neighbours (*kNN*) Classifier

The K-Nearest Neighbours (*kNN*) classifier is a non-parametric learning algorithm, which means that it does not require any prior knowledge about the dataset. It assumes that the dataset are identically distributed and, hence, the data that are close to each other belong to the same category [107]. It is known as a *Lazy Learning* technique, since it uses the entire training dataset for its prediction, without learning something about it first.

Assuming that the entire training dataset is being used and that its class is known, the idea behind the *kNN* algorithm is to find the majority classes of the k-nearest instances. The k-nearest instances can be calculated by the Euclidean geometric distance between two tuples x and y, where x is from the training dataset and y is from the testing dataset, which class is unknown:

$$D(x, y) = \sqrt{\sum_{i=1}^{k} (a_i(x) - a_i(y))^2} \tag{2.3}$$

where a is the value of the attribute (available input variables). The majority class will be the prediction of the *kNN* classifier.

Other metric distances could be used in the *kNN* algorithm depending on the type of training dataset, such as Hamming Distance [108]. However, for texture classification, the Euclidian distance is an appropriate choice.

Figure 2.16 shows the class prediction of an unknown instance based on its 4-Nearest Neighbours ($k = 4$). Since three of its neighbours are from a red class and one is from a blue class, its class is assigned to red.

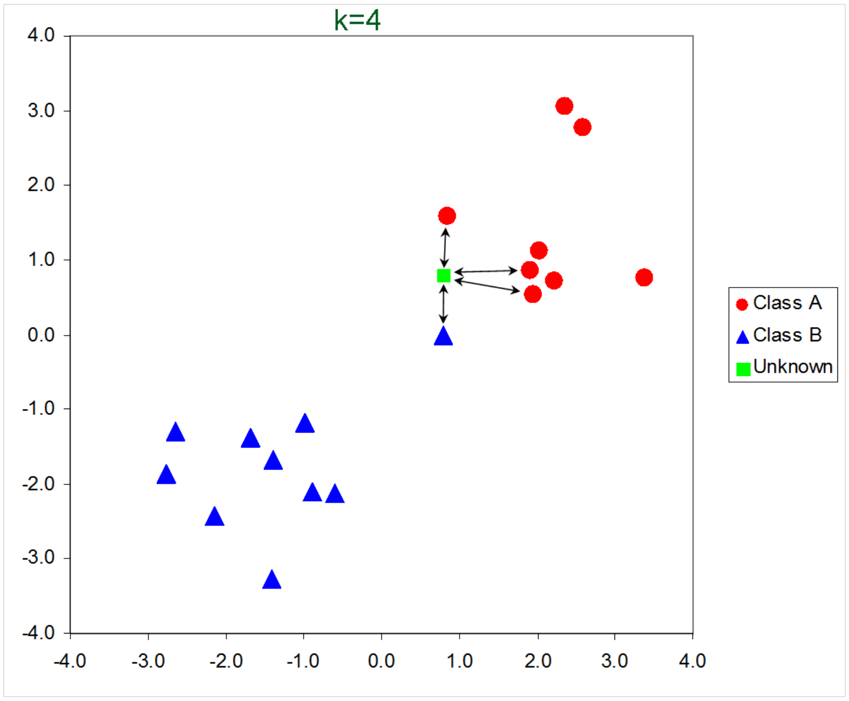

Figure 2.16: Prediction using *kNN*: the 4 nearest neighbors are 3 red and 1 blue. The most frequent class is red, hence, the test sample is assigned to the red class. Adapted from [109].

The *Scikit-Learn* package provides a *kNN* classifier, and it was used for the texture classifications.

2.5.4 Decision Trees

To introduce the concepts of Extremely Randomized Trees (*Extra Trees* classifier) and *Random Forest* classifier, the concept of a Decision Tree Model is essential. The idea behind decision trees, as the name suggests, is based on a decision-making procedure by obeying a set of rules. For instance, if various binary questions were made regarding the training dataset, it would be possible to classify it based on the answers. Figure 2.17 illustrate an example of a decision tree algorithm.

The tree is comprised of nodes, which are the points of the tree in which the questions are asked. The first node is called the root node. The depth of the three is related to the

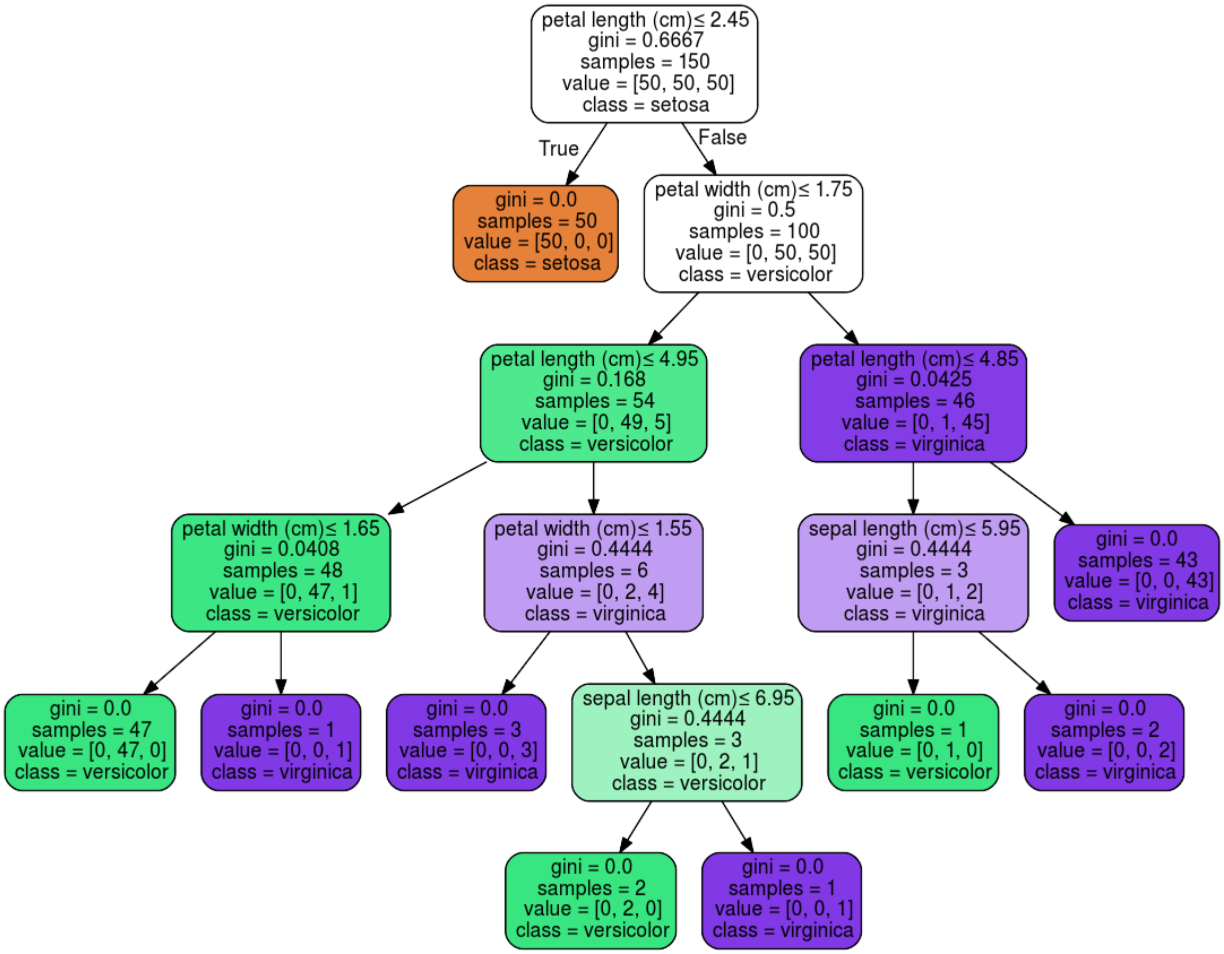

Figure 2.17: Example of Decision Tree Algorithm [110].

number of nodes that a tree has. Hence, for instance, the depth of the tree in Figure 2.17 is 5, since the root node starts at depth 0. Not limiting the depth of a decision tree may lead to over-fitting results. The last boxes, called leaves, are the class labels that represent a classification decision. The arrows represent logical conjunctions and are called branches.

An example is given in Figure 2.17, where three classes are considered: *setosa*, *versicolor*, and *virginica*. The root node "asks" if the input data has a length smaller or equal 2.45. If the statement is true, then the input will be classified as *setosa*. If not, the next node will make another question, and so on. The metric function called *gini* is used to quantify how impure the node is. For example, in the root node, ‘$gini = 0.6667$, since there are 100/150 ‘*setosa* class. Highly accurate predictions are achieved when the leave is pure. In other words, the lesser the '*gini* value, the better the prediction. Therefore, the decision tree algorithm selects the parameters that minimize impurity.

2.5.5 ***Random Forest*** **Classifier**

The *Random Forest* classifier consists of a set of Decision Trees (hence the name Forest). The classifier selects data samples randomly and creates a decision tree for each selection. By means of majority voting between the decision trees, the *Random Forest* method chooses the best classification. By combining the results of the trees, the accuracy is improved by reducing their individual errors.

The *Random Forest* algorithm can be determined as [111]:

1. determine N trees from the training data;
2. for each sample, grow a classification tree;
3. predict testing data by using the majority vote of predictions from the N trees.

A more complete and detailed mathematical formulation can be found in [112]. The *Random Forest* classifier can also be found in the Scikit-Learn Python library [113].

Advantages:

1. robust method with high accuracy;
2. reduce the bias by using the forest of decision trees.

Disadvantages:

1. the method is slow because of the high number of decision trees;
2. more complex to be interpreted rather than a simple decision tree.

2.5.6 Extremely Randomized Trees (*Extra Trees* Classifier)

Similarly to the *Random Forest* Classifier, the Extremely Randomized Trees, also known as *Extra Trees* Classifier, builds a forest of decision trees. The difference lies in the fact that while the Randon Forest method computes the best split combination, the *Extra Trees* technique selects a random value for the split and does not replace the samples. The randomness of the *Random Forest* comes from bootstrapping the samples, but the *Extra Trees* builds its randomness in the split process [114].

2.6 Surface Exploration

The sense of touch provides information about the environment and objects. Static and dynamic explorations can be used to gather information from an object or a surface. Static exploration is done by pressing the robotic fingertip against the object surface. Temperature, object profile, and external stimuli are properties that can be estimated with this type of exploration. The dynamic exploration is done by laterally sliding the robotic fingertip on the object?s surface. Friction, smoothness, and slippage are some of the object's properties that can be measured by this kind of exploration [115]. The static and dynamic explorations are not mutually exclusive, and they complement each other.

2.6.1 Related Work

This section presents relevant work done over the years in the BioIN Robotics Lab at the University of Ottawa, including research conducted by the author of this thesis.

A robotic finger was used to perform object recognition by static touch and a surface profiling by dynamic touch [116]. The static exploration was done by a high sampling resolution tactile sensor array [117] mounted on two opposing fingers of the robot's gripper. The geometric shape of the object?s surface grasped by the gripper could be identified using a Neural Network interface with an average recognition rate of up to 96%. The dynamic exploration used a robotic finger comprised of four motors and an IMU attached to the most extreme motor. Seven different well-defined profile shapes were explored using a soft and rigid fingertip. The classification of shapes resulted in an average recognition rate of up to 98.9% using the IMU magnetometer feedback. The experiment setup is illustrated in Figure 2.18.

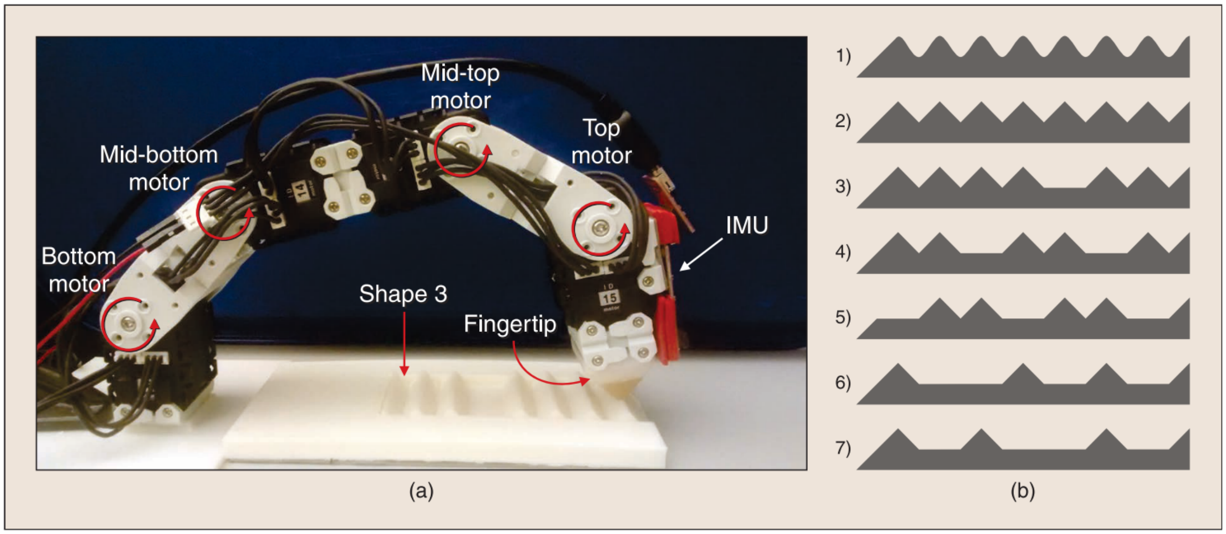

Figure 2.18: (a) Robot finger exploring a shape, (b) Seven shape profiles. [116].

A pyramidal multi-modal tactile sensor was developed and mounted on the fingertip of a robotic finger, illustrated in Figure 2.19, in order to perform dynamic exploration tasks [8, 118]. The pyramidal sensor is made an IMU and deep barometer embedded in Urethane Rubber Compound. Seven surfaces with clearly distinctive shapes were explored.

Seven surfaces similar to the experiments reported in [116] were used. The finger completed one hundred sliding exploration movement on each surface. A total of 700 samples were saved. From these, 25 % were randomly selected to be part of the training dataset. Prepossessing the training data can be summarized in three steps. First, the data collected passed through a Discrete Wavelet Transform (DWT) decomposition [119] in order to reduce the signal noise. Second, the values resulted from the DWT decomposition were subjected to a Principal Component Analysis (PCA) [120] to reduces the number of variables in the dataset. Third, a Multilayer Perceptron (MLP) neural network was used to classify the surfaces' profiles. The classification resulted in accuracy up to 98.9 % using

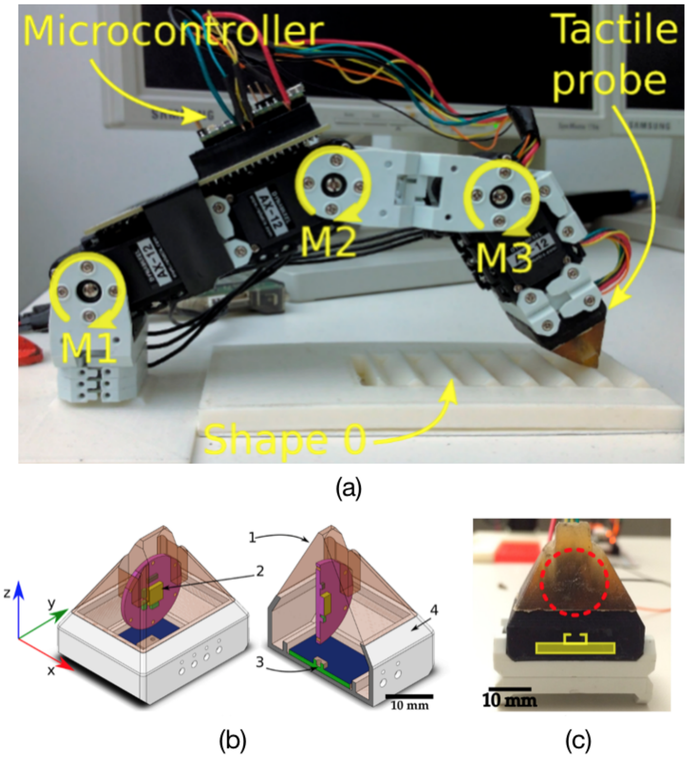

Figure 2.19: (a) Robot finger composed of three motors (b) Tactile module: 1 - pyramidal compliant structure; 2 - IMU on printed circuit board (PCB); 3 - deep pressure sensor; and 4 - supporting collar. (c) Tactile probe front view: the barometer is located under the yellow overlay in the black 3D printed collar and the IMU under the red circle. Adapted from [8] and [118].

the data from the barometer. When combining the data from the IMU and the barometer, a classification with an accuracy of 100 % was achieved.

The pyramidal multi-modal tactile sensor could not be integrated with an anthropomorphic robotic hand, mainly because of physical constraints. Hence, inspired by the form and functions of the main four mechanoreceptors located in hand, a biologically inspired tactile sensor was created by [5] and discussed in Section 2.4.3. This sensor was miniaturized and enhanced in this thesis (discussed in Chapter 3).

It is important to note that the explored surfaces had clean, well-defined low-frequency profiles, which are easier to identify comparatively to the more complex high-frequency surface textures (utilized in the experiments in Chapter 5).

2.6.2 Other Approaches

An extensive literature review about texture classification using tactile sensing systems can be accessed in [28]. Relevant studies are presented below.

A tactile probe comprised of a small metallic rod with a single-axis accelerometer attached near its tip was utilized to identify surfaces in the circumstances of all-terrain low-velocity mobile robotics [121]. Ten different surfaces were used: wood bench; tiled linoleum flooring; untiled linoleum flooring; terrazzo; short hair carpet; large tiles for raised computer floors; grass; paving made of concrete bricks similar to Interblock; large gravel; and small gravel on packed dirt. According to the group, one essential factor in surface identification is the frequency response of the transducer. Fine surfaces have a high frequency of vibrations. Hence, the transducer, used to capture its vibrations, must have a large bandwidth. The experiments were conducted at a constant speed of 70 cm/s, and the signals were recorded at a rate of 4 kHz. Eight features were selected for the classification process, seven in the temporal domain and one in the frequency domain. The features in the temporal domain were: (1) mean; (2) variance; (3) skewness; (4) kurtosis; (5) fifth moment; (6) number of times 20 uniformly separated thresholds are crossed; (7) sum of the variation over time. The feature in the frequency domain was: (8) sum of higher half of the amplitude spectrum. Combining features in the temporal and spectral domain is beneficial because spectral analysis may ignore essential cues that are available in the temporal domain (and vice-versa). The data collected was split in 70% as a training dataset and 30% as a testing set. A neural network with two hidden layers with 20 neurons each was used using the NETLAB library [122]. The testing success rates were 94.6%, considering all the ten surfaces.

A triple-axis Micro-Electro-Mechanical Systems (MEMS) accelerometer mounted near the tip of a stylus was used to gather data from 28 different surfaces [123]. The tactile sensor was configured to collect data at a rate of 800 Hz. The tactile probe was placed on a record player, where the surfaces were attached. The experiment was conducted at a constant relative speed of 45.0 rpm (58.9 cm/s at the stylus' tip). Different materials were used: hard surfaces (ceramic tile, aluminum, and steel), soft surfaces (artificial wadding and cotton fabric), hard texture (kitchen towel and grass carpet)), light texture (wood panel and fiberglass), natural materials (leather, cork panel and paper board), and synthetic materials (leatherette and soft vinyl cover). Similarly to [121], the group used features extracted from the temporal (mean, variance, skewness, kurtosis, fifth moment, number of times 20 uniformly separated thresholds are crossed, and the sum of the variation over time) and frequency domain (sum of higher half of the amplitude spectrum). The data collected was divided into two equal sets and used as training and testing datasets. The *SVM* classifier from the LIBSVM library [124] was used with gamma = 0.0186 and C = 16 as parameters, obtained by stratified 10-fold cross-validation. The classification resulted in an overall success rate of 99.95%. Furthermore, the best feature was determined by analyzing its performance individually. The feature that produced the best success rate (97.4%) was the feature extracted from the frequency domain (sum of higher half of the amplitude spectrum).

A humanoid robot with a 3D printed artificial fingernail composed of a three-axis accelerometer was used to explore 20 different surfaces (cloth, leather, wood, rubber, paper, and plastic materials) with five different dynamic exploratory movements [125]. The accelerometer collected the data at a rate of 400.0 Hz. Three types of lateral explorations from right to left were performed in slow, medium and fast velocities. The other two movements were done in a perpendicular direction concerning the first three in fast and medium velocities. The discrete Fourier transform was applied to find the frequencies over time; however, its spectrogram displayed a high dimensionality. A 2D spectrotemporal histogram was used to overcome this issue. Hence, the data was transformed into a vector of dimensions 5-by-25. Two machine learning algorithms were used to classify the surfaces: *kNN* and *SVM* classifiers. The *kNN* classifier used k = 3 neighbours as a parameter and was implemented using the WEKA machine learning library [126]. The *SVM* classifier utilized a polynomial function of second degree available in the WEKA library. The robot classified the surfaces with 80.0% accuracy. This work confirmed that multiple exploratory movements (different directions and velocities) are essential to improve the classification of surfaces. A similar outcome was obtained in a prior work done by the same group [127].

An artificial fingertip, comprised of a three-axial MEMS-based force sensor, was used to gather data from 10 different kinds of fine papers [128]. The exploratory movements were conducted in two dimensions (X and Y axis) using two different velocities (3.8 cm/s and 7.6 cm/s). Only one axis of the sensor was used for the classification process. Three features were used in the temporal domain: friction coefficient, calculated as the mean tangential force necessary to slide; variance; and kurtosis. The spectrum slope of the samples characterizes the frequency domain component. The *MLP* technique and the minimum Euclidean distance to the mean spectrum were used to classify the textures.

A robotic fingertip, 2.5 times the size of an average human thumb, with a semi-spherical shape at its extremity, was used to classify seven different fine textures [129]. Eight commercially available force sensors and five three-axis accelerometers, embedded to the robotic fingertip, tries to mimic the mechanoreceptors in the human hand. The exploratory movement was made in one dimension, where the robotic finger slid in reverse and forward directions. The Fourier coefficients obtained by the Fast Fourier Transform were used as features for a neural network with one hidden layer. The classification produced an accuracy of 65 %.

An underactuated human-size tendon-driven robotic finger integrated with a 2-by-2 tactile array in the distal phalanx was used to classify three different fine surfaces [130]. Experiments were conducted by passive and active touch. According to the group, passive touch is defined as keeping the finger static, while moving the texture beneath it. Whereas, active touch is determined by sliding the fingertip while keeping the texture motionless. The passive touch exploration was performed in velocities of 6.7 mm/s and 10 mm/s, while a velocity between 22 to 31 mm/s was used in the passive touch. The wavelet-coherence package from MATLAB was used to modulate the active touch exploration dynamically, and the Cross-Wavelet Transform was applied to the passive exploration to discriminate the gratings via vibratory cues. The classification from the passive touch was given by comparing the fundamental experimental frequencies to the fundamental theoretical frequencies, producing a success rate of 100 %. The *kNN* classifier was used to discriminate the textures in the active exploration, resulting in an accuracy of 97.6 % in the worst-case classification.

A silicone robotic fingertip, with randomly distributed strain gauges and polyvinylidene fluoride (PVDF) films embedded into it, was used to explore nine textures [131]. Tactile data were collected 50 times for each texture at three different speeds (41, 51, and 62 mm/s). Thereafter, the Fourier components from the PVDF sensor and the mean from the strain gauges were extracted and used as features. The classification was done by a majority voting algorithm, resulting in 95% accuracy. The group concluded their work by stating that the variation of data over time is an essential factor in distinguishing textures, but the Fourier transform does not provide such information.

The work done by [132] proposed the extraction of vibration and thermal information to compose the feature dataset. Their research used Gaussian Mixture Models (GMM) for the classification process, performing better than conventional machine learning processes (*kNN*, ANN and *SVM*).

In summary, many tactile sensing systems were proposed to classify textures. A variety of preprocessing methods, using the tactile data in the temporal and frequency domain, were applied. The most popular techniques used were the extraction of features in the temporal domain using statistical formulas (e.g. mean, variance, skewness, kurtosis) and the extraction of the coefficients from the Fourier Transform (frequency domain). Different types of machine learning techniques were used for the classification process: *SVM*, *MLP*, GMM, majority voting algorithm and *kNN*. As of yet, no method regarding the best preprocessing approach nor machine learning technique for texture classification has been concluded. Moreover, the tactile technologies in the literature still lack to provide complete tactile information about the robot's surroundings. The robot's environment can be better perceived by using the tactile-enabled fingertips developed in this thesis since it provides ten different types of tactile feedback.

In this dissertation, the raw data in the temporal domain, from each transducer (IMU and barometer), was used directly as entry data for the classification method. Hence, the dimensionality of the features was extremely high. As stated by [125], features with high dimensions can be challenging to be used in standard machine learning algorithms.

However, using the tactile data presented in this dissertation produced results with high accuracy.

Chapter 3

Multi-modal Tactile-Enabled Robotic Finger for Static and Dynamic Exploration

This chapter presents in chronological order: the new miniaturized version of the multi-modal tactile sensor; a tactile-enabled robotic fingertip, similar to a distal phalanx, for static exploration; and an articulated tactile-enabled robotic finger for dynamic explorations of textures;

3.1 The Miniaturized Multi-Modal Tactile Sensor

Section 2.4.3 presented the first version of the multi-modal tactile sensing developed in the BioIn Robotics lab [5].

The first version of the Multi-modal Tactile Sensing Module was discussed in Section 2.4.3. Unfortunately, the size of this module makes it unsuitable for skin-like applications, which require a higher spatial resolution. In order to solve this significant problem, a second, miniaturized version had been developed. The difference between the sizes of the first and second versions is shown in Figure 3.1. The specifications of both versions of the tactile sensing module are summarized in Table 3.1.

The miniaturized version uses two commercially available transducers: the deep barometer and the IMU. The specifications are listed below.

The pressure transducer is a commercially available Freescale MPL115A2 Barometer with the following specifications: dimensions of 5 mm x 3 mm x 1.2mm; a range of 50 kPa to 115 kPa; an accuracy of ±1 kPa; communication type I2C; and supply voltage of 3.3 VDC. The barometer emulates the functions of the Pacinian corpuscles.

The IMU model is a LSM9DS1 MARG system with the following specifications: dimensions: 3.5 mm x 3 mm x 1.0mm; gravity field sensor (accelerometer): ±2/±4/±6/±8/±16 g full scale; magnetic field (magnetometer): ±4/±8/±12/±16 Gauss full scale; angular velocity (gyroscope): ±245/±500/±2000 degree per second full scale; resolution: 16-bit; communication: I2C; supply voltage: 3.3 VDC. The accelerometer, the magnetic field, and the angular velocity emulate the functions of the Merkel cells, Meissner cells, and the Ruffini endings, respectively.

A Printed Circuit Board was designed for the barometer and the IMU because there are no commercially available PCBs available for the size required.

Table 3.1: First and second version of the Multi-Modal Tactile Sensor specifications

	Multi-modal Tactile Sensor (version 1)	Miniaturized Multi-modal Tactile Sensor (version 2)
Communication	I2C	I2C
Supply Voltage	3.3 VDC	3.3 VDC
Baro Dimensions	5 mm x 3 mm x 1.2mm	5 mm x 3 mm x 1.2mm
IMU Dimensions	4 mm x 4 mm x 1.0mm	3.5 mm x 3 mm x 1.0mm
Baro PCB Dimensions	17 mm x 14 mm x 1 mm	13 mm x 13 mm x 1 mm
IMU PCB Dimensions	R = 8.5 mm, w = 0.5 mm	R = 4.5 mm, w = 1 mm
Acceretometer	±2/±4/±6/±8/±16 g	±2/±4/±6/±8/±16 g
Gyroscope	±245/±500/±2000 °/s	±245/±500/±2000 °/s
Magnetometer	±2/±4/±8/±12 Gauss	±4/±8/±12/±16 Gauss
Barometer	50 to 115 kPa (± 1kPa)	50 to 115 kPa (± 1 kPa)

Analyzing the Table 3.1, one can notice that while the barometer dimensions did not change between both versions, the IMU version is 35 % smaller. A redesign was made to the barometer and IMU PCBs, so the sizes were 29 % and 72 % smaller than the original version, respectively.

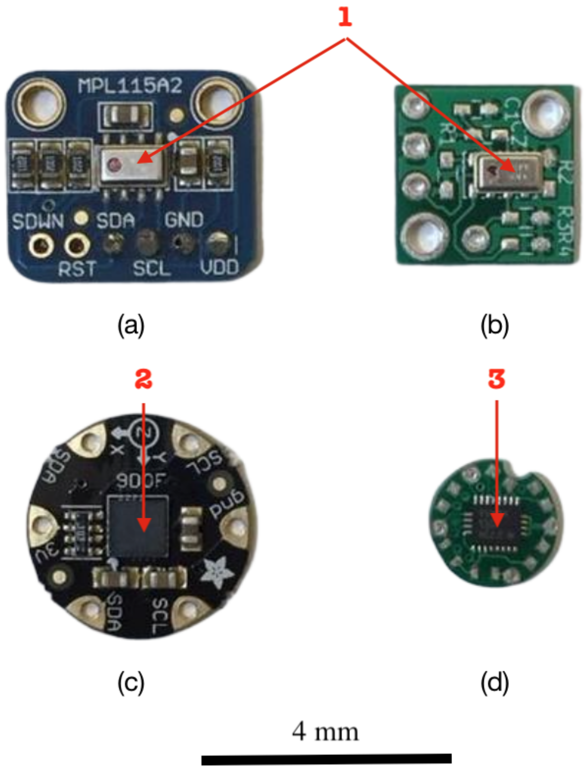

Figure 3.1: The elements of the Tactile Sensor. (a) the first version of the barometer its PCB; (b) the second version of the barometer its PCB (29 % smaller); (c) the first version of the IMU and its PCB, and (d) the second version of the IMU and its PCB (72 % smaller). 1 - MPL115A2 barometer. 2 - LSM9DS0 IMU. 3 - LSM9DS1 IMU

The overall size of the multi-modal tactile sensor module was reduced to approximately 68% relative to the original one. While the first version had 14 mm x 16 mm x 20 mm and a diameter of 18.5 mm, the newer version had 13 mm x 13 mm x 18 mm and a diameter of 10.5 mm.

The final prototypes built can be seen in Figure 3.2.

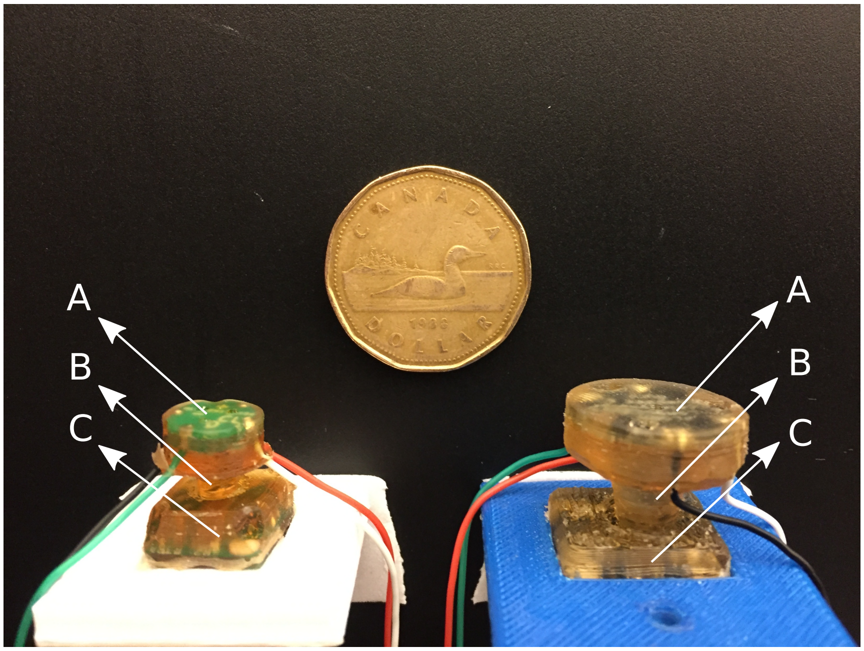

Figure 3.2: Left: the miniaturized multi-modal tactile sensor module (version 2); Right: the multi-modal tactile sensor (version 1). A - IMU; B- conic compliant structure; C - deep barometer

3.2 Tactile-Enabled Distal Phalanx for Static Object Exploration

A tactile-enabled distal phalanx fingertip was developed for the static exploration of the skin in order to measure the heart rate, as further discussed in Chapter 4. The design of its structure and the final prototypes are shown in Figure 3.3 and Figure 3.4. Its structure resembles a medical device easy to be manipulated, similar to a pen and the distal phalanx. The purpose of the ergonometric shape was so that the pulse measurement would be an easy task to perform.

The distal phalanx has dimensions of 10 cm in height and 3.4 cm and 2.5 cm in diameter, for the first and second versions of the tactile module. The square hole was designed to fit perfectly each version of the tactile prototype. An "L" shaped hole was made to enable the barometer wires to pass through the model, while four circular holes were made for the IMU wires. The depth of the square hole was made in such a way that only a small portion of the module's tip touches the skin. This strategy is valid because high external pressure stimuli are prevented. For instance, if the user presses the device too hard against the skin, the tactile sensor would not deform more than it should, since the 3D-printed base would act as a barrier. Hence, the module is protected from potential damage caused by a user.

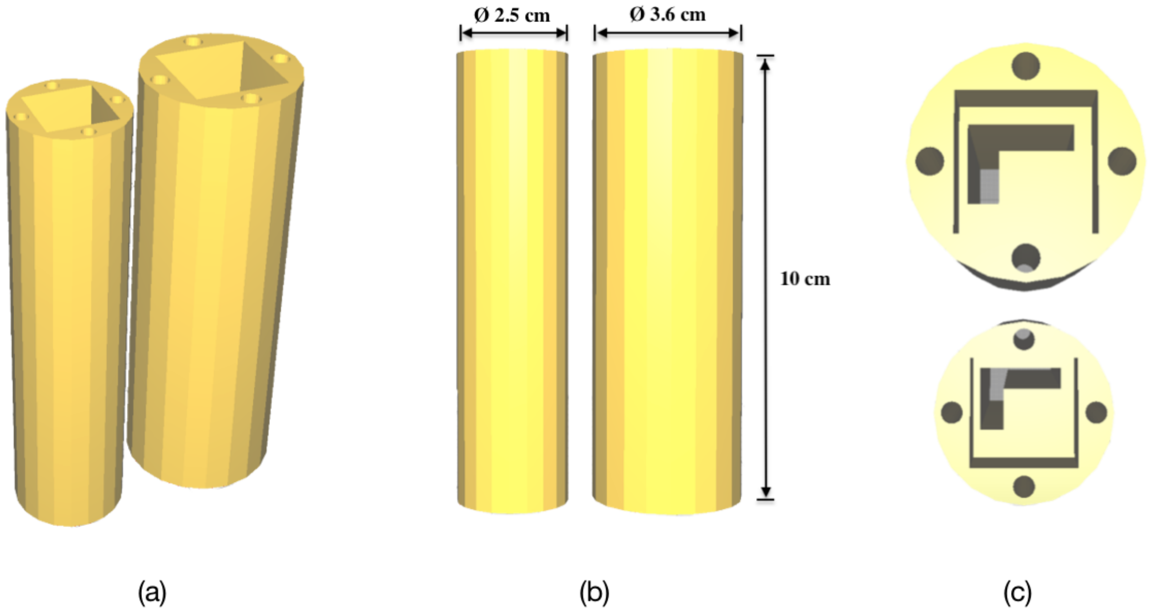

Figure 3.3: The distal phalanx design for the first and second version of the tactile module. (a) 3D view, (b) front view, and (c) top view.

3.3 Articulated Tactile-Enabled Robotic Finger for Linear Dynamic Exploration

The fingertip base was specially redesigned for the dynamic exploration conducted in Chapter 5. The 3D model of the fingertip structure is shown in Figure 3.5.

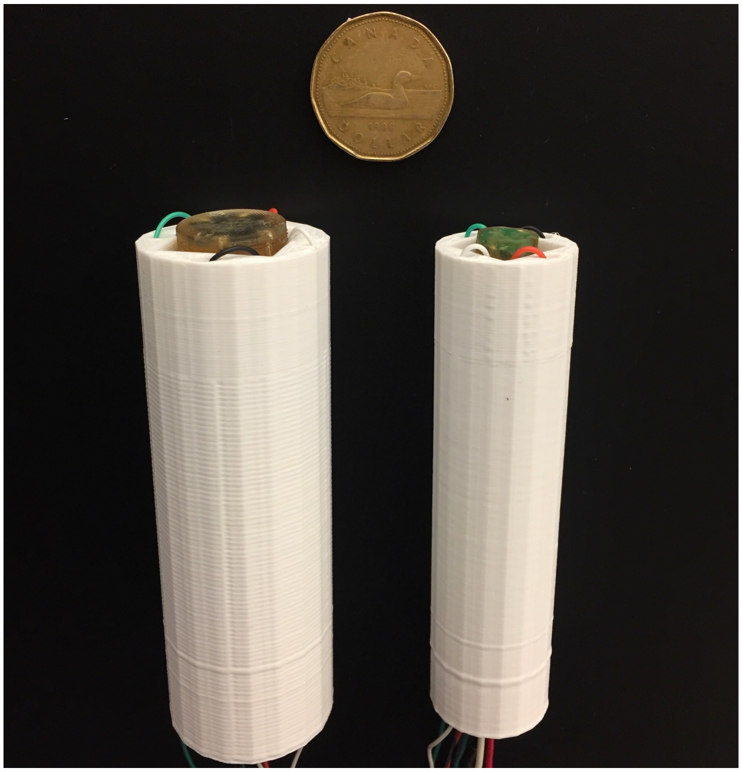

Figure 3.4: The tactile-enabled robotic distal phalanges used for static exploration

The new version of the distal phalanx has an angulation of twenty degrees, enabling the tactile sensor to touch the textured surface properly. Its dimensions are a length of 4.9 cm, a width of 4.5 cm, a lower height of 3.1 cm, and a larger height of 4.6 cm. Four circular holes were made for the IMU wires, and one "L" shaped hole was made for the barometer wires. A Dynamixel motor was screwed in the square cavity located at the bottom of the structure with the motor's dimensions. The motor functions as the finger's middle phalanx and its rotation as the distal joint.

The final prototype resembles the extremity of a humanoid finger, where the robotic joint represents the distal joint and the robotic fingertip, the distal phalanx, as shown in Figure 3.6.

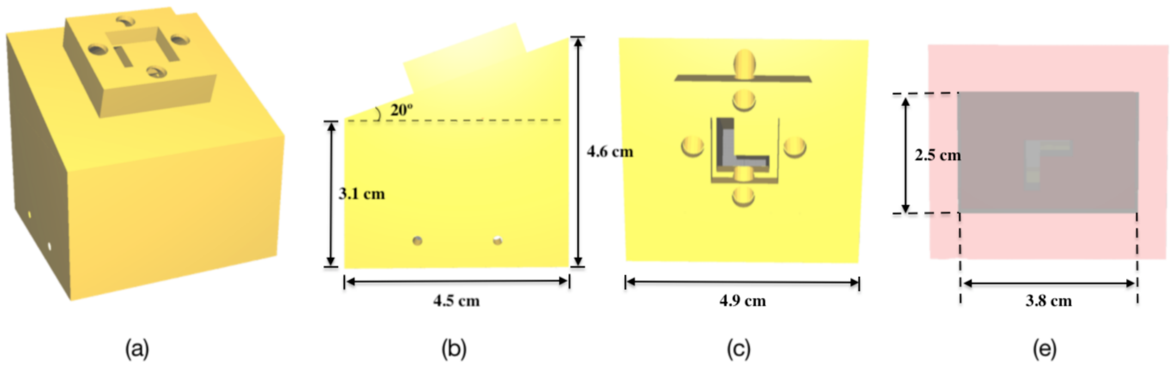

Figure 3.5: Fingertip base for dynamic exploration. (a) 3D view, (b) lateral view, (c) top view, and (d) bottom view.

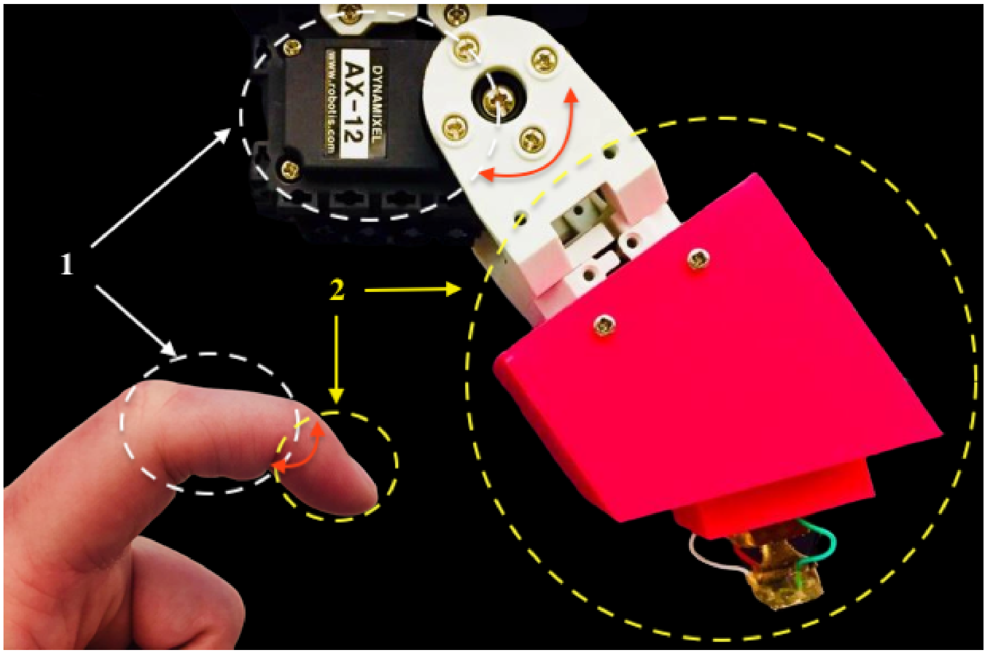

Figure 3.6: Articulated tactile-enabled robotic finger used for dynamic exploration. 1 - middle phalanx, and 2 - distal phalanx. The distal joint is represented in red.

3.4 Articulated Tactile-Enabled Robotic Finger for 2D Dynamic Exploration

Experiments obtained in Section 5.3 had clearly shown that the flat-shaped fingertip, described in the previous subsection, used for the linear exploration, is not suitable for 2D dynamic surface exploration. Its small area of contact when exploring the textures (only the edge of the sensor touching the surfaces) makes the exploration less efficient. Therefore, in order to tackle this problem, another version of the tactile sensor fingertip was developed. A semi-spherical tip, made of the same compliant material, was introduced at the tip of the module. Along these lines, a 2D exploratory movement could be performed, since the contact force is radial.

A mould was designed in the shape of a semi-sphere with the same diameter as the miniaturized version. The final prototype is illustrated in Figure 3.7.

With the new version of the tactile sensor, a new articulated robotic finger was created and is shown in Figure 3.8.

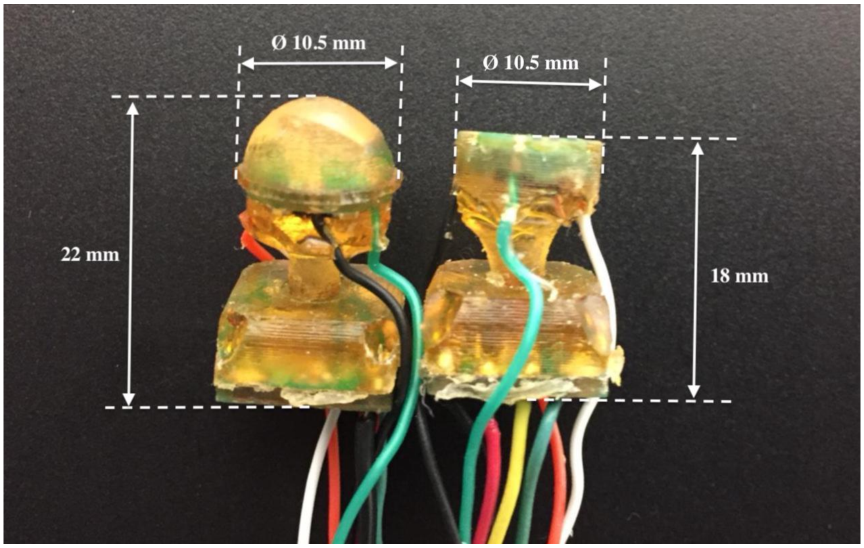

Figure 3.7: Left: semi-spherical fingertip on top of the miniaturized multi-modal tactile sensor. Right: flat fingertip.

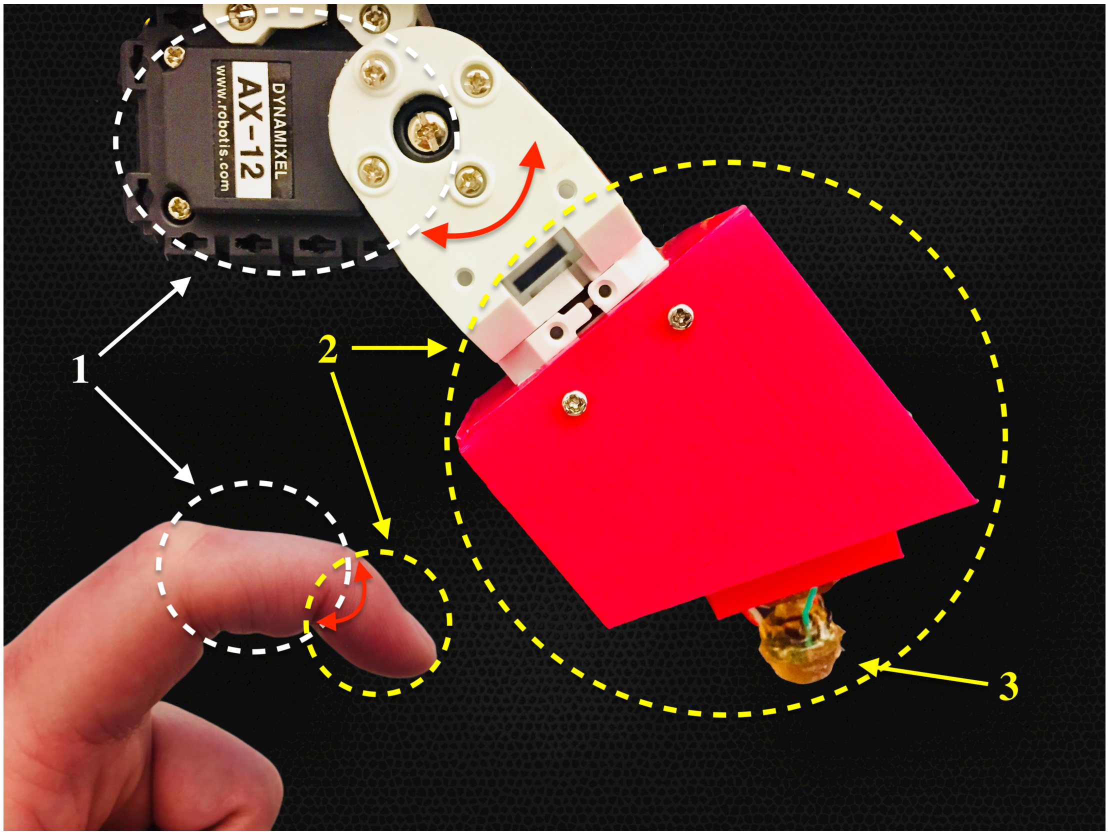

Figure 3.8: Articulated tactile-enabled robotic finger with the sensor modified with a semi-spherical tip. 1 - middle phalanx, 2 - distal phalanx, and 3 - tactile sensor with semi-spherical tip. The distal joint is represented in red.

Chapter 4

Static Exploration for Heart Rate Detection

This chapter discusses a new procedure to measure the heart rate by statically exploring the human skin vibrations while the tactile-enabled robotic fingertip maintains a fixed relative position on the human subject's skin. Research contributions that arose from this chapter can be found in [6] and in [7].

4.1 Heart Rate Detection

The heart rate is defined as a recurrence of the cardiac cycle. It begins with an atrial contraction and ends with a ventricular relaxation [133]. Pressure changes in the heart chamber conduct the blood flow in the circulatory system. This results in the deformation of the veins and arteries. Subsequently, the skin is slightly deformed, and natural electric signals are triggered. The resulting skin deformations and electric signals can be measured in order to monitor the heart.

The pulse is a convenient parameter to test a person's health status [134, 135]. It is used as a parameter for medical diagnosis, fitness evaluation, and recognition of emotions. Two traditional heart rate measurement techniques are electrocardiograms (ECGs) - where electric signals are measured by attaching electrodes to the patient; and pulse oximeter - where the sensor is applied to the hand or wrist [136, 137].

Other studies used alternative techniques that do not require skin contact, e.g.. Doppler Radars [138, 139], vision based detection [140], and impulse radar [141]. Heartbeats were measured with 95% to 99% accuracy using video analysis from a camera-based photoplethysmography [140]. Other research measured the heart rate by monitoring the frequency variation of an un-modulated wave that was transmitted by a Doppler radar and reflected by a human's chest [**?**].

Although skin-contact devices can be inconvenient, it is still a necessary feature to have in some scenarios. For instance, a health care robot can use tactile systems to measure vital signs even when its vision system is not functioning.

4.2 Heart Rate Measurement Using a Tactile-Enabled Robot Finger

The tactile response to external stimuli is one of the three most important activities in human tactile sensing [25, 142]. In this case, the external stimuli are produced by the local skin vibrations due to the heartbeat. Considering that the measurement of heartbeats using multi-modal tactile sensors is not commonly found in the literature, a new technique was developed in order to measure heartbeats using a multi-modal tactile-enabled robotic fingertip.

As explained in Section 3.2, a distal phalanx robotic finger was designed and used for the experiments conducted in this chapter. Its ergonomic shape makes it easy to apply it in direct contact with the skin surface. The design was made in such a way so that only a small portion of the top of the sensor touches the skin.

The calibration process, illustrated in Figure 4.1, was done by manually pressing the device down until it reached its minimum value, and then pulling it up until it reached its maximum value. Both the maximum and minimum values were computed in order to normalize the graphs shown in Section 4.4.

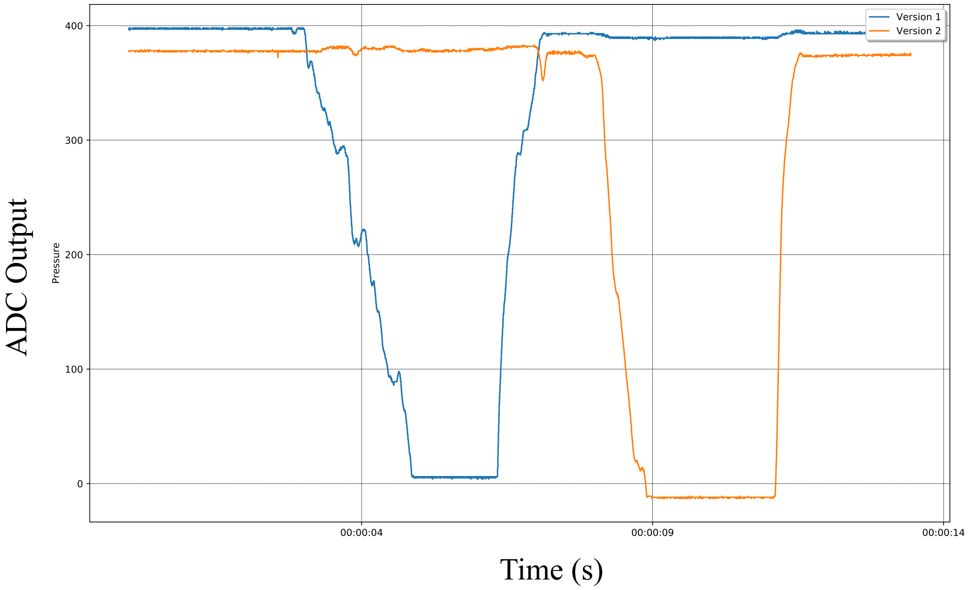

Figure 4.1: Calibration of both versions of the fingertip: the output signal from the first version is presented in blue, and the output signal from the second (miniaturized) version is shown in orange

4.3 Experimental Setup

The first experiment used the robotic fingertip with the original version of the tactile module. The second experiment used both versions of the robotic fingertip. A commercially available device that calculates the heart rate by attaching it to the wrist, a pressure wrist monitor, was used as control. A comparison was made between the versions of the robotic fingertip and the wrist monitor to determine the effectiveness of the fingertip developed.

The author's carotid artery was located by manually feeling the pulse with the researcher's hand. In order to facilitate the experiment procedure, a "X" mark was made on the subject's neck. The devices were controlled by a micro-controller and a multiplexer. The devices were placed perpendicularly on the "X" mark, as shown in Figure 4.2.

In the first experiment, the first version of the robotic fingertip was placed on the right neck's side. In the second experiment, one of the devices was placed on the right side of

Figure 4.2: Tactile-enabled fingertip being placed on the author's carotid artery

the subject's neck, while the other on the left neck's side. In order to prevent bias, the sensors were placed alternately on each side of the neck. The wrist monitor was attached to the author's wrist. The tactile data only started to be recorded after the wrist monitor was turned on. Each trial lasted approximately 30 seconds; that was the time required for the wrist monitor to calculate the pulse.

Ten trials were conducted in the first experiment. The first five trials were done while the author was in a rest position (sitting on a chair) and rested. The last five trials were completed after five minutes of regular aerobic exercises, but yet in a rest position.

Fifteen trials were conducted in the second experiment. All the trials were done while the author was rested and in an upright position.

4.3.1 Data Acquisition

The Robotic Operating System (ROS) [143], was used for data acquisition and to run multiple tasks synchronously.

The signals recorded during these tests had a frequency of 400 Hz, which is amply sufficient to cover the data acquisition of even the highest known pulse rate of 600 bpm (10 Hz) reported in the case of a quadriplegic male suffering of tachyarrhythmia [144].

For both experiments, only the data from the deep barometer was recorded and processed. However, the IMU data could be used to infer unexpected movements and discard unwanted data.

It was noted that the pressure signal fluctuated not only because of the pulse but also because the user was holding the robotic fingertip. The pressure output had a decreasing or increasing trend, which is not related to the pulses, but the pressure inflicted by the experimenter. Therefore, a reliable method was developed to compensate for this issue. The method tracks the trend of the measurement signals by identifying the peaks, as explained in the following section.

4.3.2 Smoothed Z-score Peak Detection algorithm

The Smoothed Z-score Peak Detection algorithm uses a moving mean to track the signal's trend and calculates standard deviations to create a threshold around the signal. The algorithm selects the points that are outside this threshold and identifies them as peaks. The algorithm is based on the principle of dispersion: if the distance from the data point to the mean is a certain number of standard deviations, the point is classified as a peak [145]. Most peak detection algorithms have a large number of parameters, making it harder to implement. The Z-score algorithm was chosen for having only a few constraints.

The algorithm uses three parameters: lag (l), influence (I_n) and threshold (th). The lag dictates how adaptive (regarding long-term average of the data) the algorithm is and also how smoothed the data will be. The lag will improve the robustness of the algorithm. For instance, if a lag is set to 100, the algorithm will adapt to the trend every 100 samples. The influence is the impact that the signals have on the threshold. Influence zero means that data has no influence on the threshold (that assumes a stationary process). If the signal is not stationary, the influence should be set between 0 and 1. An influence of 0.1 means that signals have 10% of influence that normal data points have over the threshold.

The threshold is the parameter that determines if the data point is a peak or not. It is the number of standard deviations from the moving mean. This parameter will determine how sensitive the algorithm is.

The Z-score based adaptive peak detection are given by the following equations (adapted from [146]).

$$\mu_i = I_n x_i + (1 - I_n)\mu_{i-1} \tag{4.1}$$

$$\bar{\mu_i} = \frac{1}{l}\sum_{i}^{i+l} \mu_i \tag{4.2}$$

$$\sigma_{\mu_i} = \sqrt{\frac{\sum_i^{i+l}(\mu_i - \bar{\mu_i})^2}{l-1}} \tag{4.3}$$

$$z_i = \frac{x_i - \bar{\mu}_{i-1}}{\sigma_{\mu_i}} \tag{4.4}$$

$$y_i = \begin{cases} \pm 1 & \text{if } |z_i| \geq th \\ 0 & \text{if } |z_i| < th \end{cases} \tag{4.5}$$

where l is the lag, I_n is the influence, th is the threshold, x_i is the barometer signal, μ_i is the signal after influence was applied, $\bar{\mu_i}$ is the mean, σ_{μ_i} is the standard deviation, and y_i is the output signal.

For the first experiment, the following parameters were used: $th = 2.5$, $l = 100$ and $i_n = 0.1$. A lag of 100 implied that the last 100 observations were used to smooth the data. A threshold of 2.5 will determine if a data point is 2.5 standard deviations away from the moving mean. An influence of 0.1 means that the signal has 10% of the influence that normal data points have.

For the second experiment, a threshold of 3.0, an influence of 0.1 and a lag of 100 were set. These values were chosen based on the result of empirical tests.

A pseudocode is provided below (adapted from [145]):

Algorithm 1 Smoothed Z-score Peak Detection pseudocode

```
**Input:** $y \geq lag + 2$
$lag \leftarrow 100$
$threshold \leftarrow 2.5$
$influence \leftarrow 0.1$
$signals(i) \leftarrow [0, ..., 0]_{||y||}$
$filteredY \leftarrow y(1), ..., y(lag)$
$avgFilter(lag) \leftarrow mean(y(1), ..., y(lag))$
$stdFilter(lag) \leftarrow std(y(1), ..., y(lag))$
for $i = lag + 1, ..., t$ do
    if $absolute(y(i) - avgFilter(i-1)) > threshold * stdFilter(i-1)$ then
        if $y(i) > avgFilter(i-1)$ then
            $signals(i) \leftarrow +1$
        else
            $signals(i) \leftarrow -1$
        end if
        $filteredY(i) \leftarrow influence * y(i) + (1 - influence) * filteredY(i-1)$
    else
        $signals(i) \leftarrow 0$
        $filteredY(i) \leftarrow y(i)$
    end if
    $avgFilter(i) \leftarrow mean(filteredY(i - lag), ..., filteredY(i))$
    $stdFilter(i) \leftarrow std(filteredY(i - lag), ..., filteredY(i))$
end for
return $signals$
```

4.4 Results

4.4.1 First Experiment

The first version of the multi-modal tactile sensor was used and compared to the commercially available wrist watch monitor. The raw data from one of the trials are shown in Figure 4.3

Figure 4.4 shows the threshold (in green) and peak signals (in blue) of the processed data after using the Z-score algorithm.

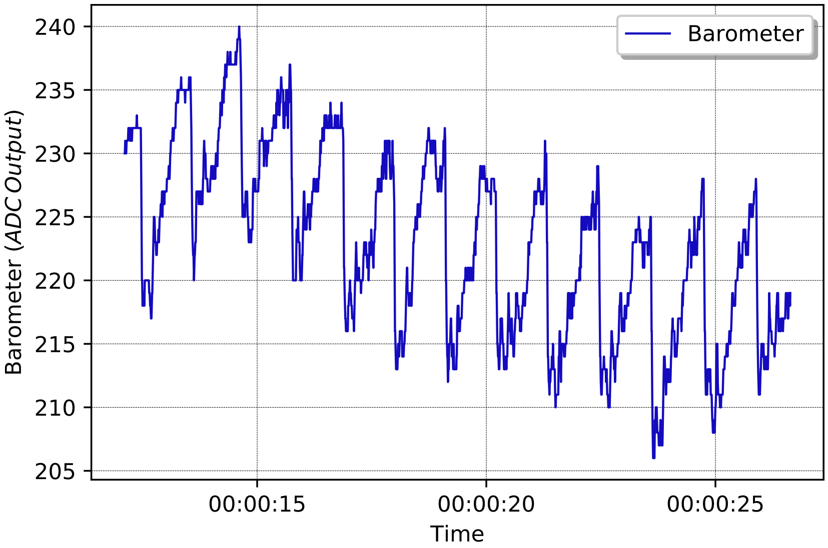

Figure 4.3: First experiment: raw data with a decreasing trend from the first version of the multimodal tactile sensor's barometer

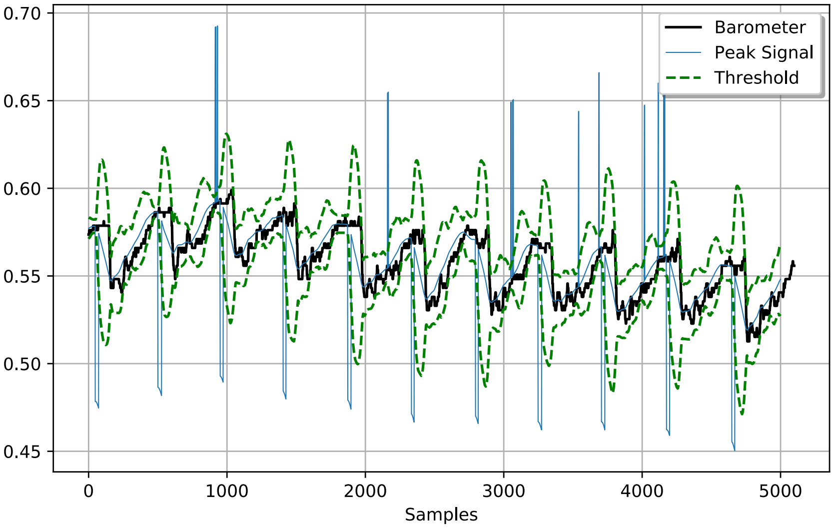

Figure 4.4: First experiment: Z-score algorithm was applied to detect the peaks from the raw data

The pulse rate (f_b) can be calculated by Equation 4.6, where Δs is the distance (in samples) between two peaks and f_s is the sampling frequency.

$$f_b = \frac{60 f_s}{\Delta s} \tag{4.6}$$

The median of the values was used in order to prevent possible outliers. Table 4.1 summarizes the heart rates calculated in rested condition and after 5 minutes of aerobic exercises, respectively, at upright position.

Table 4.1: Heart rate measured by the first version of the Multi-modal Tactile Sensor and a commercially available pressure monitor. Trials 1-5: performed at rested state. Trials 6-10: performed after 5 min of aerobic exercises

Trial	Wrist Monitor (bpm)	Tactile Module V1 (bpm)	Trial	Wrist Monitor (bpm)	Tactile Module V1 (bpm)
1	56	56	6	93	100
2	53	53	7	90	94
3	53	54	8	78	77
4	55	55	9	73	72
5	56	57	10	71	65

4.4.2 Second Experiment

The raw data obtained from the 15 trials conducted during the second experiment are shown in Figure 4.5.

The corner of the graphs shows a horizontal line that indicates when the robotic fingertip is not yet touching the subject's neck. The contact between the sensor and the neck is indicated by the signal drop. Several small spikes that represent the peaks of the heartbeats can be seen in the midsection of the graphs. The distance between two spikes was used to calculate the heart rate. Trials 6 and 14 produced major spikes located in the middle of the graph. This occurred due to the robotic fingertip repositioning to a more optimal position. However, these major spikes did not interfere with the results.

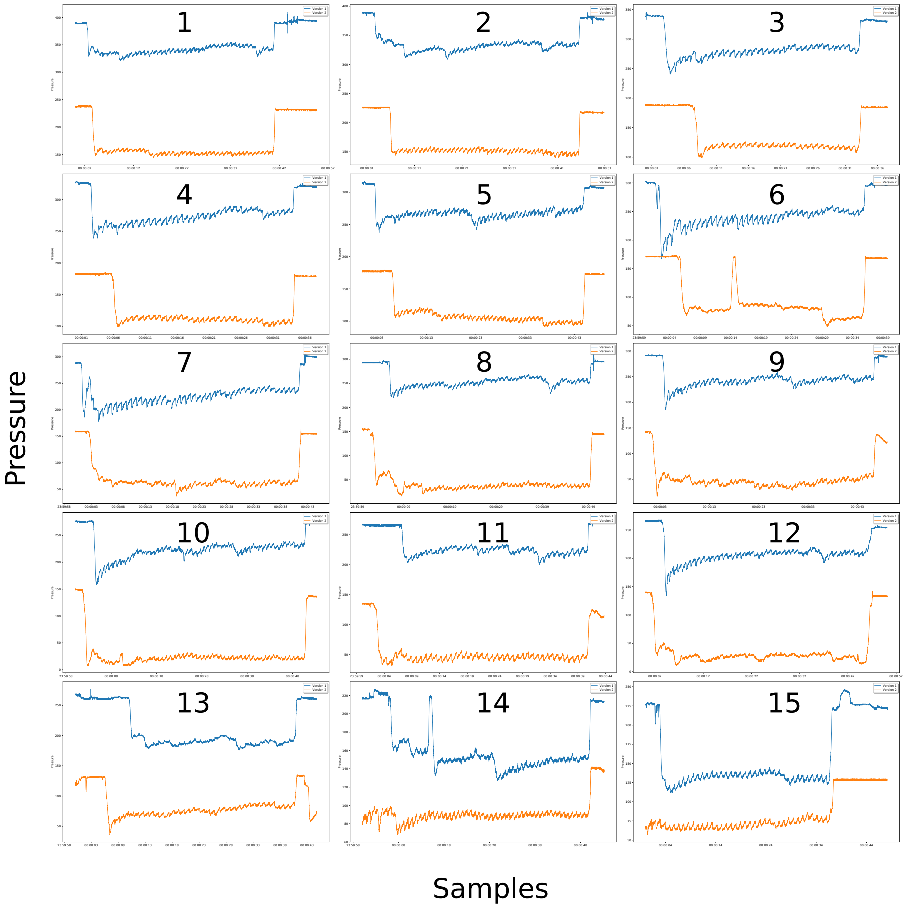

Figure 4.5: Raw pressure data from the devices of the 15 trials. In blue is the first Multimodal Tactile Sensor's version and in orange is the pressure data from its miniaturized version.

It is noticeable that the pressure lines in the case of the miniaturized version have, in general, a lower position than the first version, which is expected since the remaining initial pressure differs from different devices (caused by the compliant structure). The value itself is not important in this experiment, but the variation of it is.

The Z-score algorithm follows the trend of the mean, as shown in Figure 4.6.

The algorithm created a threshold and calculated the peaks, shown in Figure 4.7.

The heart rate was calculated using Equation 4.6. Table 4.2 summarizes the results calculated from the processed data.

Table 4.2: Second experiment: heart rate measured by the first and second version of the Multimodal Tactile Sensor and a commercially available wrist pressure monitor

Trial	Wrist Monitor (bpm)	Tactile Module V_1 (bpm)	Tactile Module V_2 (bpm)
1	72	71	71
2	71	71	71
3	70	71	72
4	72	71	71
5	71	71	72
6	66	72	71
7	65	66	64
8	67	65	65
9	64	66	63
10	65	65	64
11	66	66	66
12	63	66	58
13	63	57	64
14	64	64	65
15	62	64	62

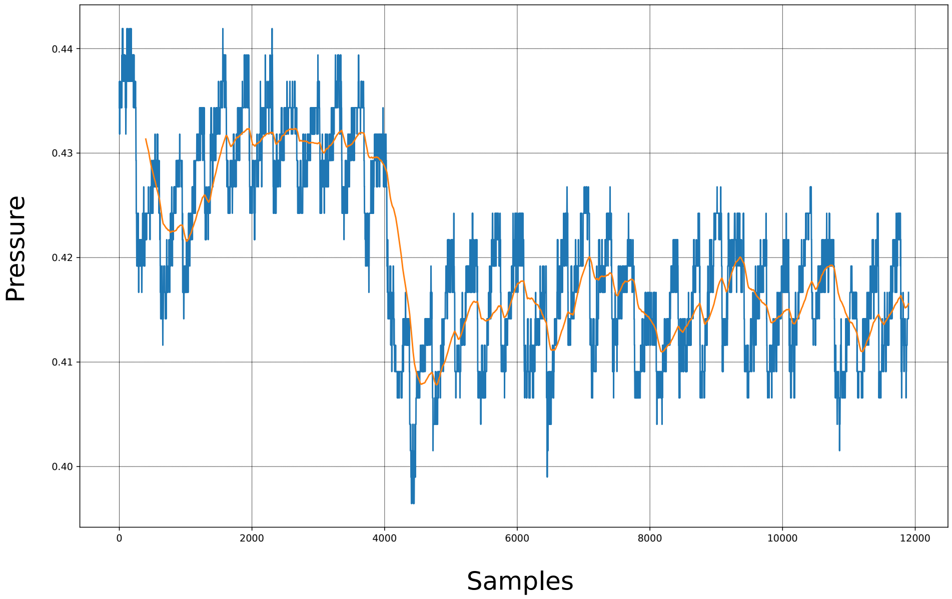

Figure 4.6: Second experiment: partial mean's trend (in orange) of the pressure signal in the case of the miniaturized tactile sensor.

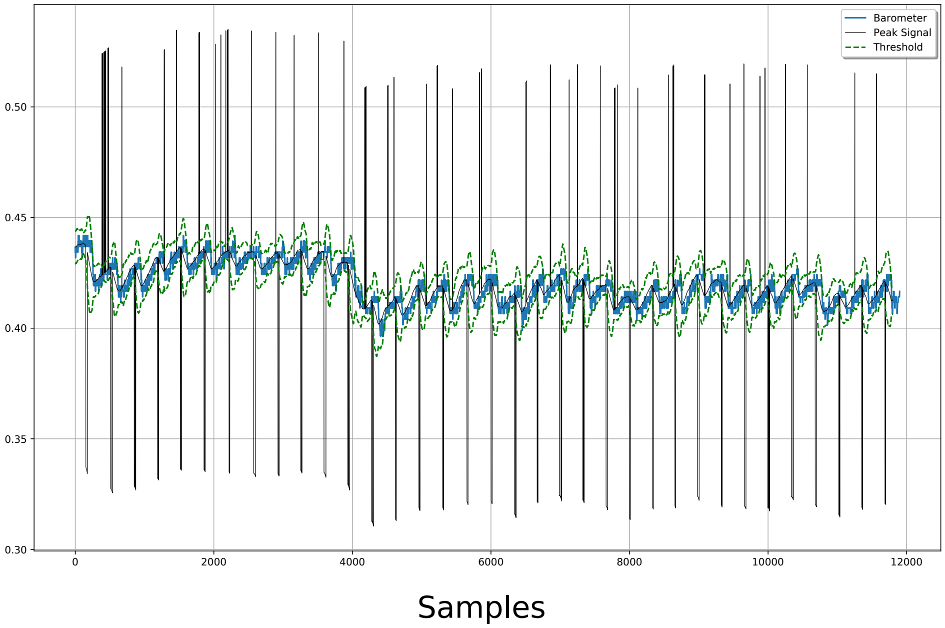

Figure 4.7: Second experiment: peaks (in black) detected by the Z-score algorithm. Data for the second experiment using the miniaturized tactile sensor.

4.5 Discussion

4.5.1 First Experiment

The raw pressure signals gathered from the tactile sensor during this experiment were quite useful for the calculation of the pulse. Peaks and trends corresponding to the cardiac cycle can be seen in Figure 4.3. The implementation of the Z-score algorithm tackled the decreasing trend problem existent in the raw data.

The heartbeats calculated were similar to the wrist monitor values. A maximum difference of 1 bpm was found for the first five trials, and a maximum difference of 7 bpm, for the last five trials. The 7 bpm difference could be explained for two reasons: (i) the respiration rate increases with the heart rate, which may have caused interference in the detection of the peaks; and (ii) the wrist monitor is only meant to work accurately in case of constant heartbeats, whereas in the second trial it was decreasing.

The mean absolute error (MAE) can be calculated as:

$$MAE = \frac{1}{N}\sum_{i=1}^{N} |y_i - \hat{y}_i| \tag{4.7}$$

where y_i is the data from the tactile sensor and $\hat{y}$ is the data from the wristwatch. Hence, the MAE for the first five trials and for the last five trials were calculated and are equal to 0.4 bpm and 3.8 bpm, respectively. Hence, the heartbeat measurements using the robotic fingertip are more reliable in normal rested conditions.

4.5.2 Second Experiment

As shown in Figure 4.5, the raw data from the barometer indicated a signal that was similar to the traditional heartbeat measurements. Hence, we can infer that the sensors have a high sensitivity, allowing it to measure the pulse effectively.

According to Table 4.2, the heartbeats measured by the first version of the sensor and its miniaturized version were similar to the values provided by the wrist monitor.

That indicates that the implementation of the Z-score algorithm tackled the decreasing or increasing trend problem observed in the raw data.

Trials 1-to-5, 7-to-11, 14 and 15 (80% of the cases) resulted in similar measurements, with only a difference up to 2 bpm between the tactile sensor and the wrist monitor (the control device). The trials that differed slightly were 6, 12 and 13. Trial 6 had a clear signal for both sensors (measuring 72 and 71 bpm, respectively).

A signal interference was observed in trials 12 and 13 (the miniaturized tactile module version in trial 12 and the original tactile module version in trial 13). The interference was due to the misplacement of the tactile sensor, which affected the measurement data.

The mean absolute errors for the first version and its miniaturized version were calculated using Equation 4.7 resulting in a value of 1.67 bpm and 1.47 bpm, respectively.

Therefore, if the device is placed correctly, an accurate measurement is expected. Therefore, the results validated the ability of both robotic fingertips to measure heart rates.

4.6 Conclusion

A tactile-enabled robotic fingertip was designed and built in order to explore the surface skin, measuring the pulse. The device used different versions of a multi-modal tactile sensor.

Two experiments were performed. The first experiment used the first version of the tactile sensor to validate its response. The experiment was performed on two occasions: rested state and then after a 10-minute regular aerobic exercise. The results showed a MAE of 0.4 bpm for the first five trials and 3.8 bpm for the last five trials. The high similarity in the outcomes indicated that the tactile sensor module responded in a promising manner.

The second experiment used both the first and second tactile sensor models. The results demonstrated high accuracy when compared to the commercially available wrist monitor, resulting in a MAE of 1.67 bpm for the first version of the tactile module and 1.47 bpm for its miniaturized version. Two trials had a slight difference of 6 bpm, apparently due to the misplacement of the tactile sensor on the subject's neck.

Even though only the deep barometer was used to measure heart rates, future work could include the IMU data to determine if the device has an appropriate contact with the skin (and, hence, ignore the irrelevant data). The IMU data could also be used to measure vibrations and directions. These changes would enhance the accuracy of the tactile-enabled fingertip.

Lastly, the miniaturized tactile sensor response to static explorations proved to have high accuracy.

4.7 Compliance with ethical requirements

The experiments were conducted in accordance with [147], section 8.2: "... Self- experimentation which involves minimal risk or less is permissible without Research Ethics Board (REB) approval if it is for purposes of quality control of research apparatus or methods.". The University of Ottawa's Ethics Board approved these experiments via e-mail.

Chapter 5

Dynamic Surface Exploration for Texture Classification

5.1 Tactile Exploration for Texture Classification

Touch is a vital sense, if not the most essential, and by nature, it is an interactive sense. While the environment can be passively perceived using both visual and auditory senses without physical contact, touching enables humans to recognize objects, surfaces, and textures through active interaction and manipulation. The tactual stimulus proved to be crucial in detecting environmental contact properties [148]. Touch sensing is highly dependent on the type of interaction. Not only does the brain interpret sensing signals, but the body must also choose how to touch objects in order to perceive them [149]. According to [150], haptic perception (integrating tactile and kinematic components) is related to six different exploratory movements: (i) sliding laterally for texture and surface detection, (ii) grasping to determine the overall shape, (iii) following edges to determine exact shape, (iv) applying pressure to identify stiffness, (v) lifting for weight measurement, and (vi) touching for thermal information gathering.

This chapter focusses on the dynamic exploration of textures through an articulated tactile-enabled robotic finger that slides on the explored object surface.

While the detection of rougher textures (having a spatial resolution higher them 0.5 mm) could be carried out by statically (no lateral movement) pressing the sensor down on the surface, the perception of finer textures requires a sliding motion of the sensor over the explored surface, which will generate vibrations that the sensor will detect [148]. Experimental evidence suggested that lateral movements appear to be efficient for fine texture classification [151].

An experimental study of the surface texture perception by humans was conducted by asking 20 subjects to slide their index finger on surfaces made of diverse materials such as wood, sandpaper, and velvet [152]. Roughness-smoothness and hardness-softness appeared to be independent characteristics of texture. Moreover, [153] has found that coarse/fine, rough/smooth, and sticky/slippery are efficient salient characteristics to be used for texture classification.

The experimental studies discussed in this thesis were conducted on textures on both coarse and smooth textures.

5.2 Tactile-Enabled Robotic Fingertip Response to External Stimuli

A tactile-enabled articulated robotic finger based on the miniaturized tactile sensor module was used for both 1D and 2D surface texture explorations. It is essential to understand how the IMU and the barometer components of this sensor module react to external stimuli.

The miniaturized tactile sensor module incorporates a barometer and a 9-DOF IMU that measures acceleration (a_x, a_y, and a_z), angular velocity (g_x, g_y, and g_z), and magnetic flux density (m_x, m_y, and m_z) in the XYZ coordinates, as shown in Figure 5.1.

The 3D components of the accelerometer readings are imu_ax, imu_ay, and imu_az. The 3D components of the gyroscope readings are imu_gx, imu_gy, and imu_gz. The 3D components of the magnetometer readings are named imu_mx, imu_my, and imu_mz.

Stimuli applied on the X-axis have a significant influence on the imu_gy and the imu_my

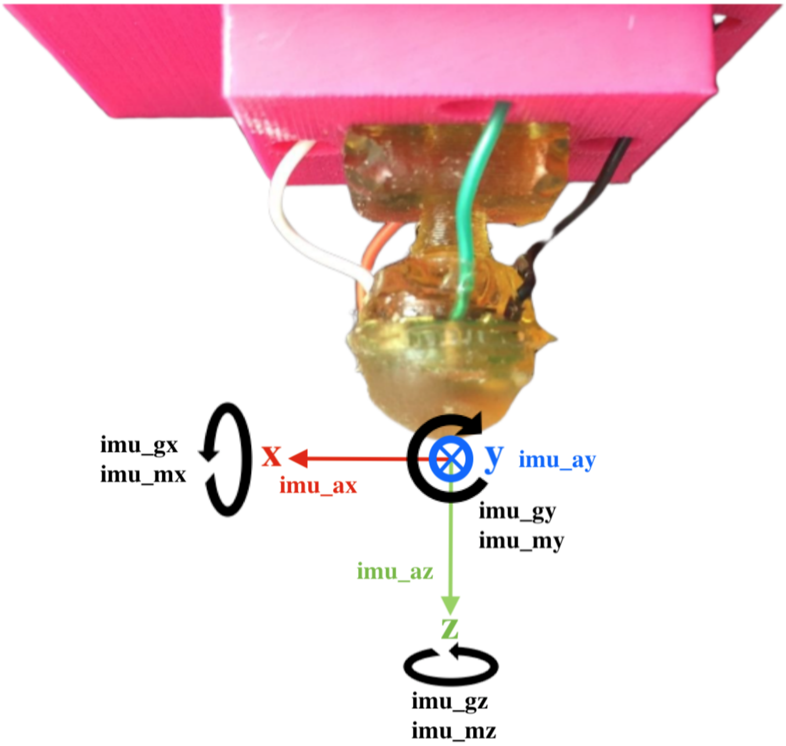

Figure 5.1: Robotic fingertip and its XYZ coordinates.

since a force applied along the X-axis makes the module spin around the Y-axis. The imu_ax and imu_az are also affected since the XZ-axes spin about the Y-axis, changing its direction. Likewise, stimuli applied along with the Y-axis impact the imu_gx, imu_mx, imu_ay, and imu_az, for similar reasons.

It is crucial to understand how the module reacts to different types of stimuli, especially in the X and Y coordinates, since the 2D dynamic exploration is conducted in both directions. Hence, a test was performed by manually stimulating the sensor in the X-axis and Y-axis. Stimuli were applied on in each axis by firstly pushing several times gently on the sensor, followed after by several flicking moments.

Figure 5.2 shows the gyroscope response to gentle and flicking stimuli. According to the first graph, imu_gy (in green) is more sensitive to interactions in the X-axis. However, the second graph indicates that imu_gx (in pink) is more sensitive to interactions on the Y-axis. The gyroscope response to flicking stimuli are shown in the last two graphs. This type of stimulus returns similar feedback to the ones obtained by exploring textures (higher frequencies feedback is expected). Following the same trend as the gentle stimuli, the third graph shows that imu_gy (in green) is more sensitive to X-axis interactions, and imu_gx (in pink) is more sensitive to Y-axis interactions.

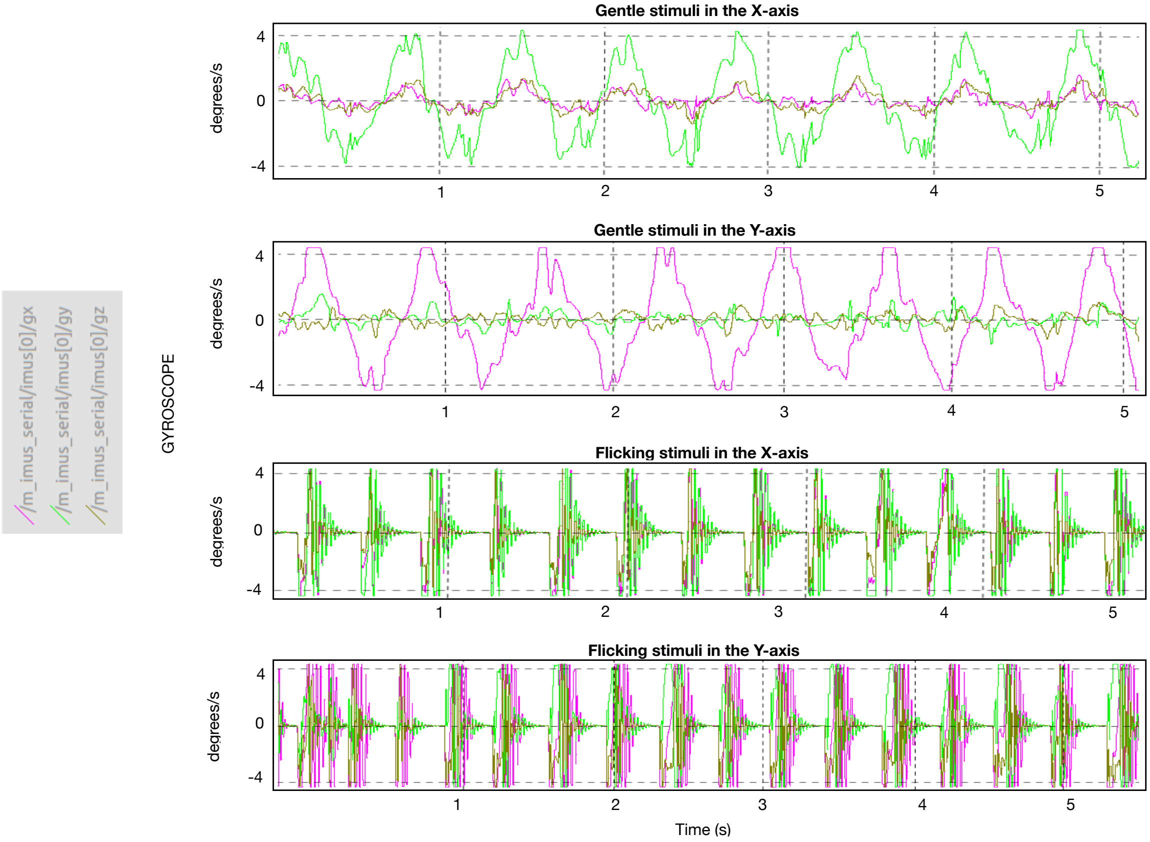

Figure 5.2: Gyroscope response (imu_gx in pink, imu_gy in light green, and imu_gz in dark green) to gentle and flicking stimuli along the X and Y axes.

Figure 5.3 shows the accelerometer response to gentle and flicking stimuli. As shown in the first graph, only the imu_ay (in green) was not affected by the stimuli along the X-axis. As shown in the second graph, it is possible to notice that imu_ax (in pink) remained unaffected by stimuli along the Y-axis. Graph three and four show the accelerometer's response to flicking stimuli. The impact of the flicking motion appears to be difficult to examine. However, some trends can be observed: while imu ay (green) does not change significantly in the third graph, it is the component that changed the utmost in the fourth graph.

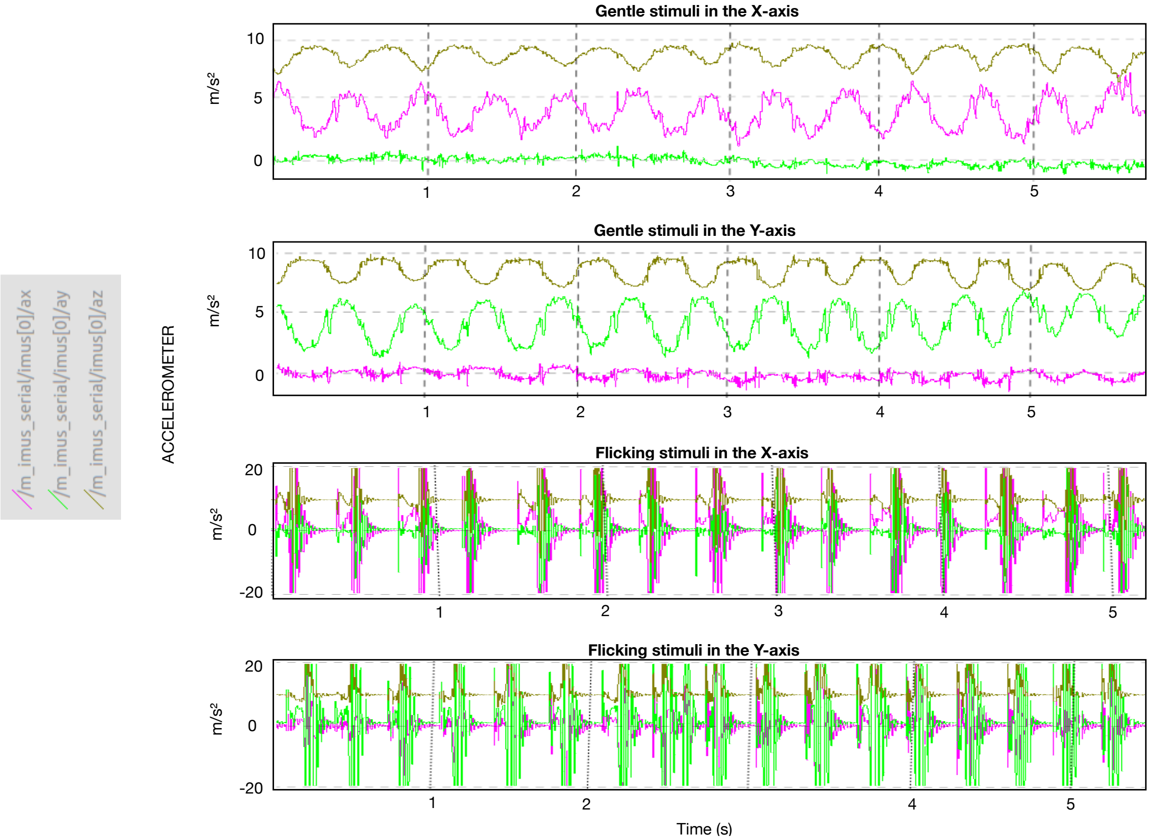

Figure 5.3: Accelerometer response (imu_ax in pink, imu_ay in light green, and imu_az in dark green) to gentle and flicking stimuli in the X and Y coordinates.

Figure 5.4 shows the magnetometer response to gentle and flicking stimuli. The components of the magnetometer seemed to react similarly in each axis in the first two graphs. An analysis revealed that the imu_my (in blue) appears to be the most sensitive to the stimuli. The magnetometer response to flicking stimuli are presented in the last two graphs. Similar to the gentle stimuli, the imu_my (in blue) seems to be slightly more sensitive than the others, especially when the responses from flicking stimuli are analyzed on the Y-axis.

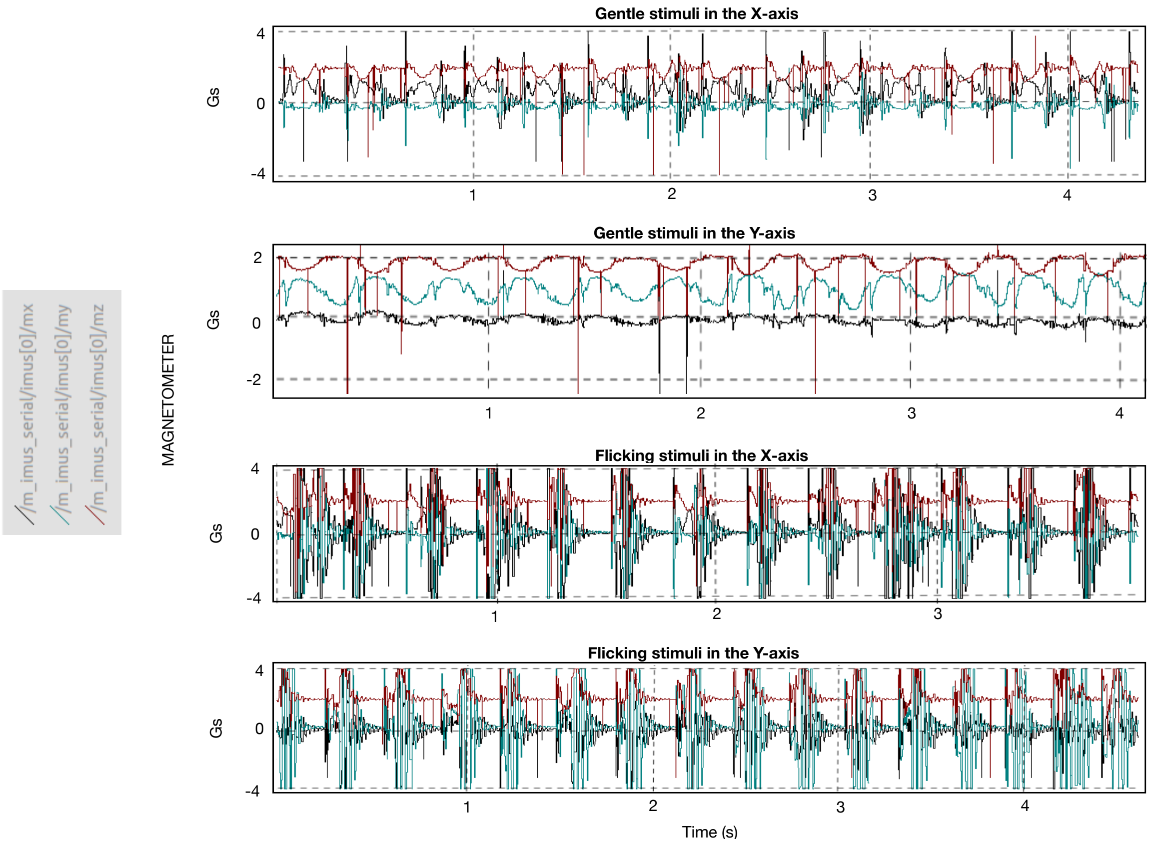

Figure 5.4: Magnetometer response (imu_mx in red, imu_my in blue, and imu_mz in black) to gentle and flicking stimuli in the X and Y coordinates.

Analyzing the barometer readings revealed that its response differed according to the stimuli's orientation, meaning that the stimuli produced in the positive orientation (i.e. positive X-axis or Y-axis) was different from the stimuli in the negative orientation (i.e. negative X-axis or Y-axis). Figure 5.5 shows the barometer's response to gentle stimuli in the positive and negative directions of the X and Y coordinates. The stimuli responses along the positive direction of the X-axis, showed in the first graph, were downwards, while the responses to the stimuli in the negative direction of the X-axis were upwards (second graph).

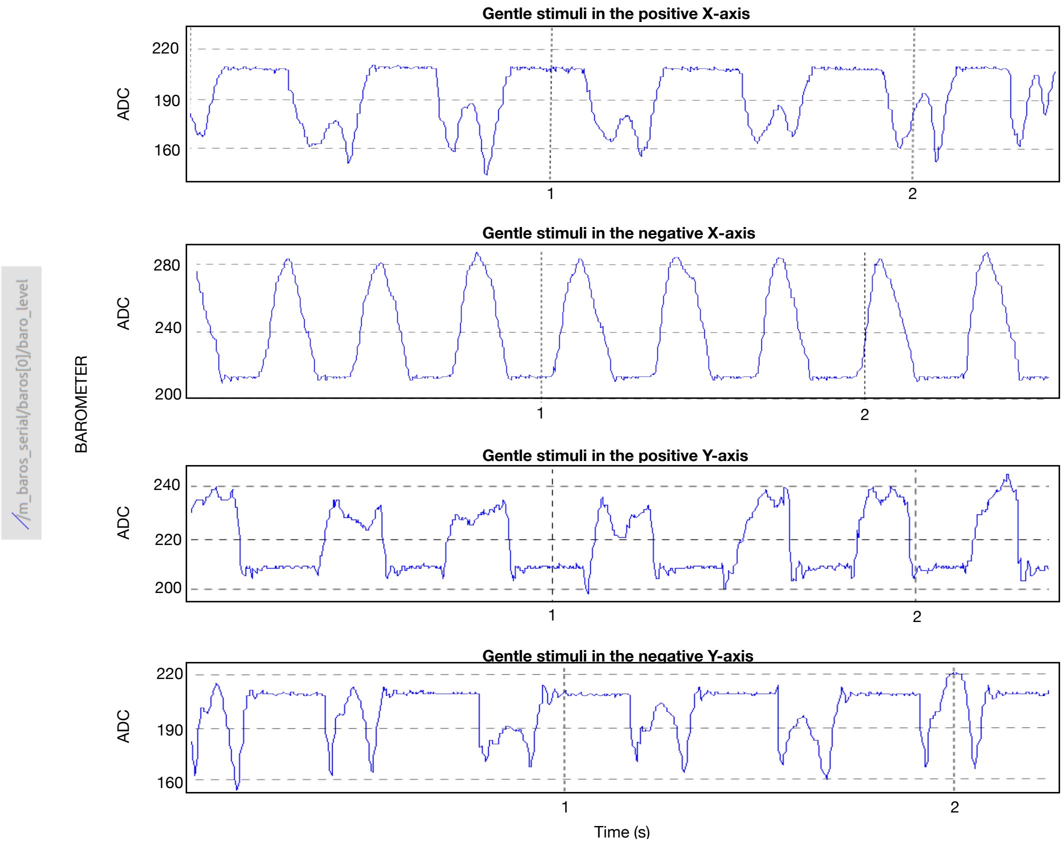

Figure 5.5: Barometer response (in blue) to gentle stimuli along the positive and negative directions of the X and Y coordinates.

A simple experiment performed by pulling and pressing the module has shown that by pulling it (positive Z direction), the feedback was upwards, while by pushing it (negative Z direction), the response was downwards. Therefore, because of the way how the tactile sensor was attached to the platform, the stimuli along the positive direction experienced a pushing movement, while the stimuli in the negative direction underwent a pulling motion. This explains the different behaviours illustrated in Figure 5.5.

Similarly, the barometer response on the Y-axis to gentle stimulations along the positive and negative directions has shown a comparable trend (last two graphs of Figure 5.5)). However, the module experienced a pulling movement as the stimuli passed through the positive Y-axis direction. Whereas, the module was pressed upon as it moved along the negative Y-axis direction

Figure 5.6 Illustrates the barometer's flicking stimuli feedback. Flicking motions combine, simultaneously, both pushing and pulling movements. Consequently, when compared to the trends illustrated in the previous figures, flicking movements results in mixed signals with no visible trend.

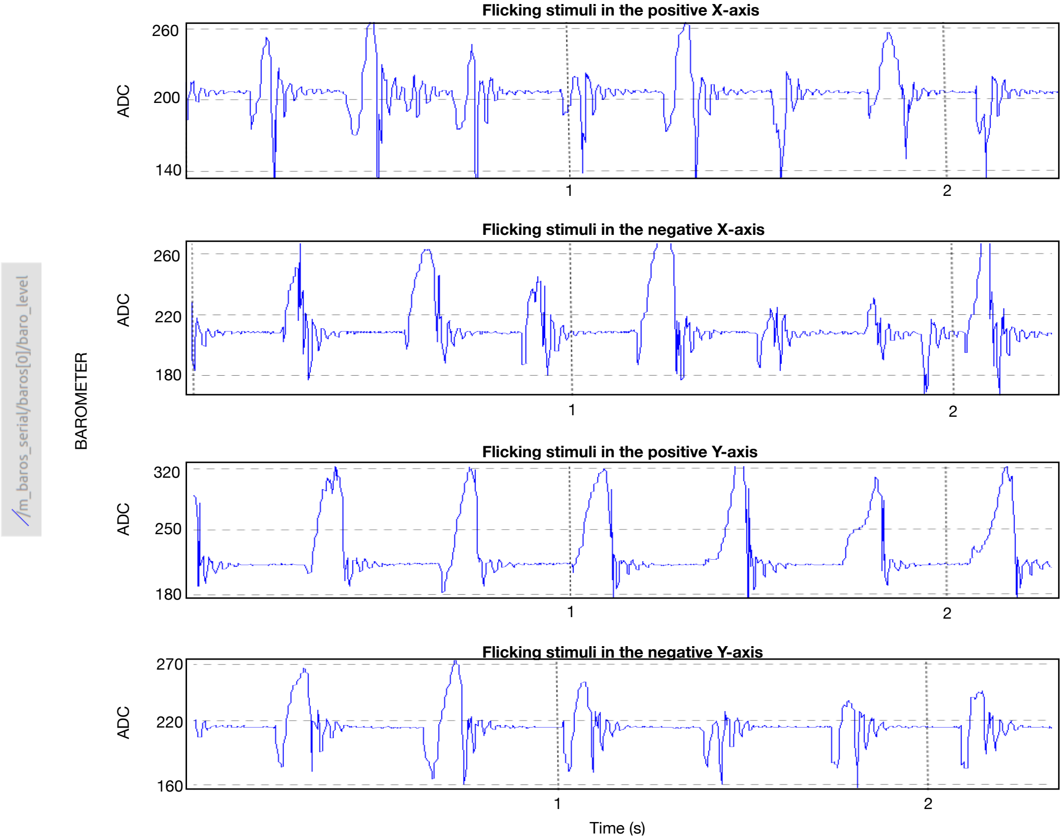

Figure 5.6: Barometer response (in blue) to flicking stimuli along the positive and negative directions of the X and Y coordinates.

5.3 One-Dimensional Exploration and Texture Classification Using an Articulated Tactile-Enabled Robotic Finger

5.3.1 Summary

An early version of the articulated tactile-enabled robotic finger, employing a flat tip miniaturized tactile sensor module, was used to collect data by exploring of thirteen different textures. The edge of the flat tip of the sensor was used to make contact with the surfaces. Different machine learning algorithms available in the *Scikit-Learn* library - *Random Forest*, Support-Vector Machine (*SVM*), Multilayer Perceptron (*MLP*), *Extra Trees*, and k-Nearest Neighbors (*kNN*) - were used for texture classification.

5.3.2 Textures

While the objects used in the previous experimental work [8], [116], and [118], had uniform low-frequency surfaces, the textures explored during the experimental work discussed in this chapter had high-frequency spatial textures (fine resolution), as usually occurs in real-world settings.

Thirteen different textures were investigated, as shown in Figure 5.7. Textures 01 and 02 are plastic pencil cases, textures 03, 04, 05, 07 and 13 are plastic placemats, texture 06 is cork, texture 08 and 09 are denim fabric, texture 10 has felt material, texture 11 is a polyester cloth, and texture 12 is a cotton scarf. Textures 04 and 13 have the same material, originated from the same placemat; nevertheless, the material is anisotropic, and since the placemat was cut in different directions, textures 04 and 13 produce different outputs when laterally explored (texture 04 is smoother and texture 13 has higher friction).

Textures 01 and 02 have irregular bumps and are hard materials. Texture 03 is a high-frequency plastic. Textures 04 and 13 will produce relevant results considering that they are the same material being explored in different directions. The correct discrimination between these two textures proves the importance of exploring materials in two dimensions. As textures 05 and 07 have uniform bumps they, theoretically, should be easier to classify. Textures 08, 09, 10, 11 and 12 are fabric materials, whereas textures 10 and 11 are the smoothest among them.

Figure 5.7: Thirteen customary textures used in the experiment.

5.3.3 Experimental Setup

An acrylic sheet was cut with a laser cutting machine in thirteen 6-by-12 cm rectangles and used as a base for the surfaces. Each texture was glued and set to rest for 24 hours on its base. Two strips of double-sided tape were placed on the back of each texture to ensure firm attachment to the moving platform during the experiment. This configuration allowed for a simple transition between textures for data collection. The sensor used in the robotic finger was the miniaturized tactile sensor with a flat tip and is exhibited in Figure 5.8.

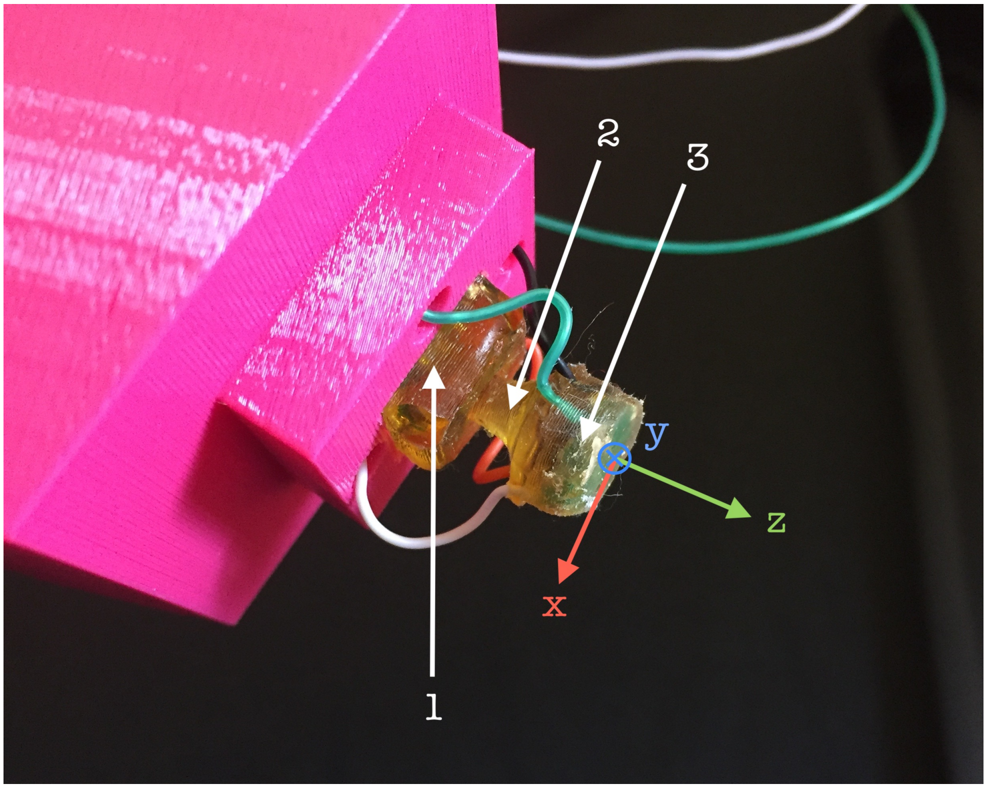

Figure 5.8: Tactile-Enabled Robotic Fingertip. (1) deep barometer, (2) compliant cone, and (3) IMU.

The robotic fingertip's construction allowed the sensor to touch the explored surface by its edge. Using the sensor's edge to slide over the surface did not create problems in the case of 1D exploration because the compliant structure of the sensor module allowed the transmission of the vibrations to the deep barometer embedded in it. However, it was found that this configuration is not optimal since the area of contact between the tactile module and the surface is small.

As shown in Figure 5.9, the distal phalanx of the finger was set in a downward position, connected to the intermediate phalanx via a distal interphalangeal joint powered by a Dynamixel-motor. The midle phalanx was mounted onto a sturdy structure. After making contact with the texture, by rotating the distal joint clockwise, the robotic finger stayed static while another motor linearly guided the texture along the robotic fingertip. This motor was set to move the textured surface at a constant speed of 30 mm/s from left to right.

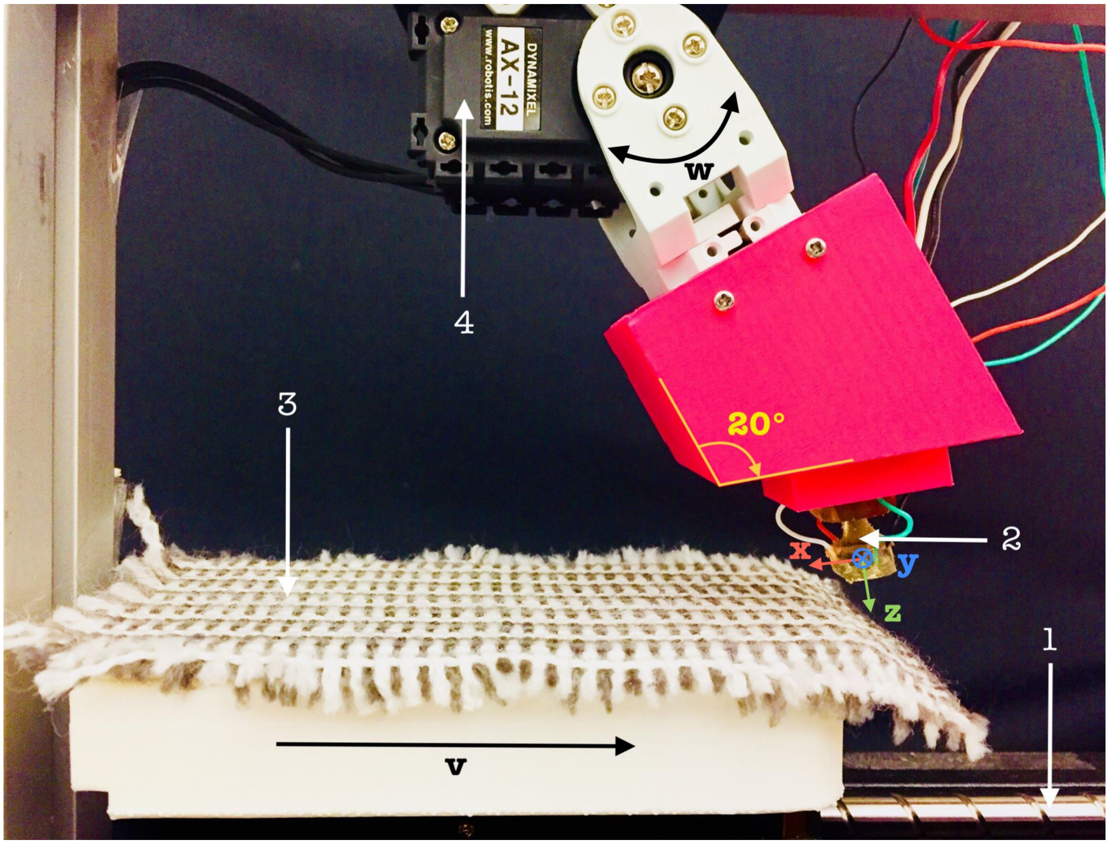

Figure 5.9: (1) Long screw actuated by a motor moving at a constant speed. (2) Miniaturized Multi-modal Tactile Sensor. (3) Texture 12 placed on the base driven by the long screw . (4) Middle phalanx and the Dynamixel-motor powered distal joint.

5.3.4 Methodology and Data Acquisition

Each trial consisted of complete sliding motion of the texture under the finger. Initially, the distal joint spun clockwise until the robotic fingertip made contact with the texture, and the deep barometer reached a specific value (empirically chosen). Controlling the initial pressure of contact ensured that the sensor touched the texture's surface correctly and that the contact between the robotic finger and each texture was the same in each trial. As soon as the pressure threshold was reached, the experimental data started to be recorded, while the textures moved linearly, from left to right, for 5 seconds. After each exploratory movement, a ROS message was published, prompting the recording to stop. For cycle-restart, the Dynamixel motor spun the distal joint counter-clockwise in order to lift the distal phalanx at a position high enough to allow the texture base to move from right to left, returning the textured surface to the initial position without touching the tactile module. One hundred trials for each texture were recorded, totalling 1,300 samples.

Each tactile sensor's component (IMU and barometer) has a dedicated micro-controller used to process the tactile data. Another micro-controller was used to control the motor that actuates the sliding base of the textured surface. ROS framework allowed the coordination of these three micro-controllers. The framework uses nodes, topics and messages to communicate with one another, allowing to have a properly controlled experimental setup. The raw sensor data collected for each texture, shown in Figure 5.10 and Figure 5.11, were stored in ROS bags.

5.3.5 Data Processing

A feature vector is defined as a vector composed of a specific IMU or barometer information.

The IMU information [a_x (imu_ax), a_y (imu_ay), a_z (imu_az), g_x (imu_gx), g_y (imu_gy), g_z (imu_gz), m_x (imu_mx), m_y (imu_my), and m_z (imu_mz)] has a signal range of 1000 Hz to 2000 Hz. The barometer has an average frequency of 350 Hz.

The difference between the barometer and IMU's frequency was a concern since the feature vectors needed to be equivalent in size in order to serve as input to the classification process. Hence, the ROS bags were recorded at a rate of 7,000 Hz and no information was lost. With this configuration, each bag file had ten feature vectors with a size of approximately 28,000 each. The size of each bag file differed slightly from bag to bag. To solve this issue, all bags were sized to a value of 18,716, corresponding to the minimum vector size among them.

Subsequently, after the bags were resized, the data was converted to the *Python Pandas* data frame. Finally, each feature vector was separated and saved into a Python-specific file (pickle). All the 1,300 bags were transformed into ten pickle files.

5.3.6 Classifiers' Settings

The classifiers used for supervised learning were *SVM*, *MLP*, *Random Forest*, *Extra Trees*, and *kNN*, available in the *Scikit-Learn* library.

The classifiers used the following settings:

- *Extra Trees*: 500 estimators with no max depth;
- *Random Forest*: 500 estimators with max depth of 30;
- *SVM*: $C = 1900$ and gamma $= 10^{-5}$;
- *MLP*: two hidden layers with 100 neurons each and max iteration of 1000;
- *kNN*: three neighbours with leaf size of 30.

These settings were empirically chosen and are most likely not to be optimal.

Out of the 100 samples per texture, 70% were used to train the classifiers and 30% to test it. This selection was done randomly to reduce bias. After that, the train and test data sets have been scaled between its minimum and maximum value, reducing the bias furthermore.

5.3.7 Results

The raw tactile data collected for each texture is shown in Figure 5.10 (barometer data) and Figure 5.11 (IMU data). There is a noticeable difference between the data collected from each texture. The data from textures 05 and 07 showed uniform peaks, which was expected since they have invariable bumps. Surprisingly, upon physical inspection, texture 10 generated a non-smooth signal. That might be the result of the hairy nature of the surface material. The tactile data collected from textures 04, 08 and 09 were similar.

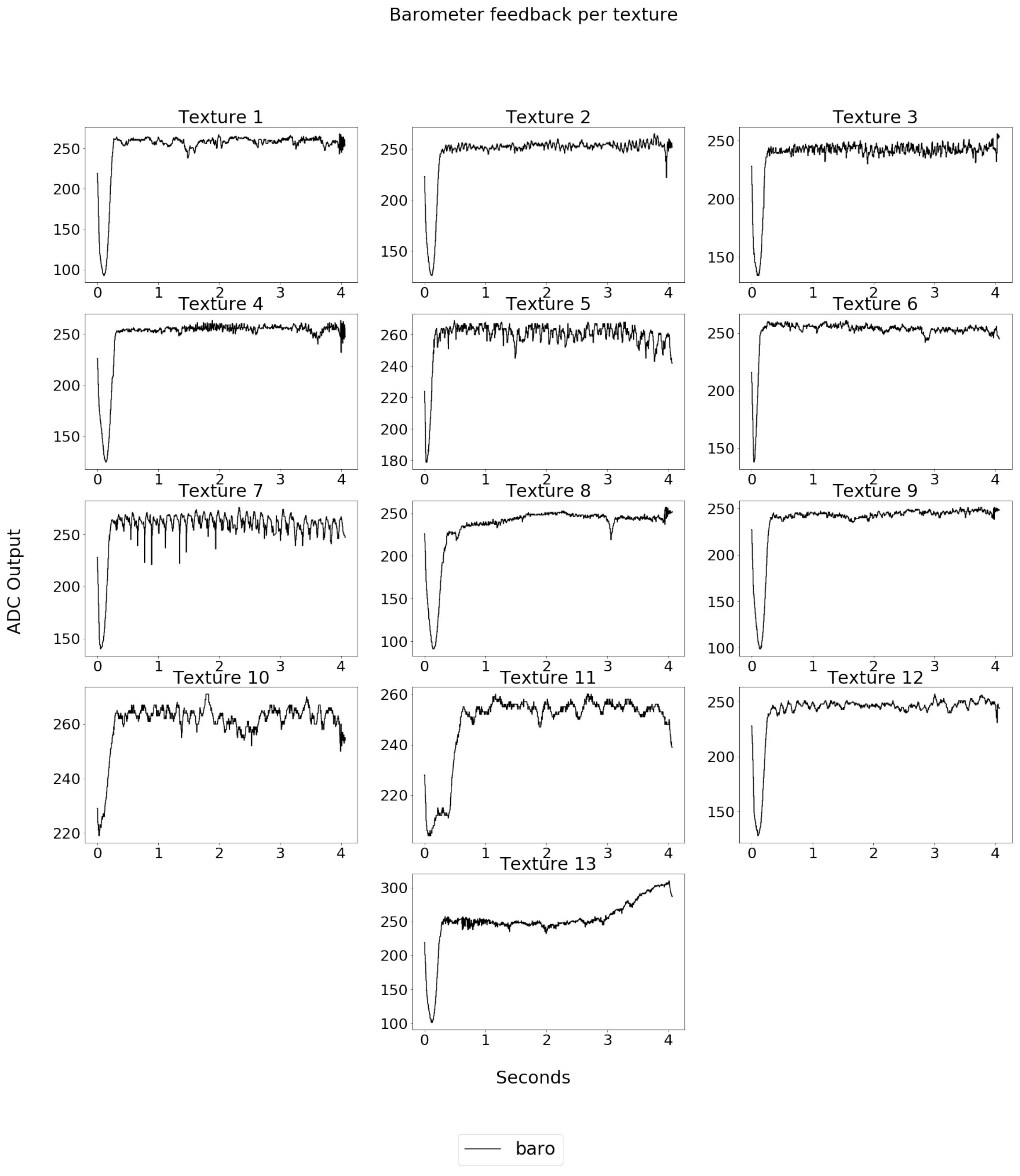

Figure 5.10: Barometer data collected for each texture.

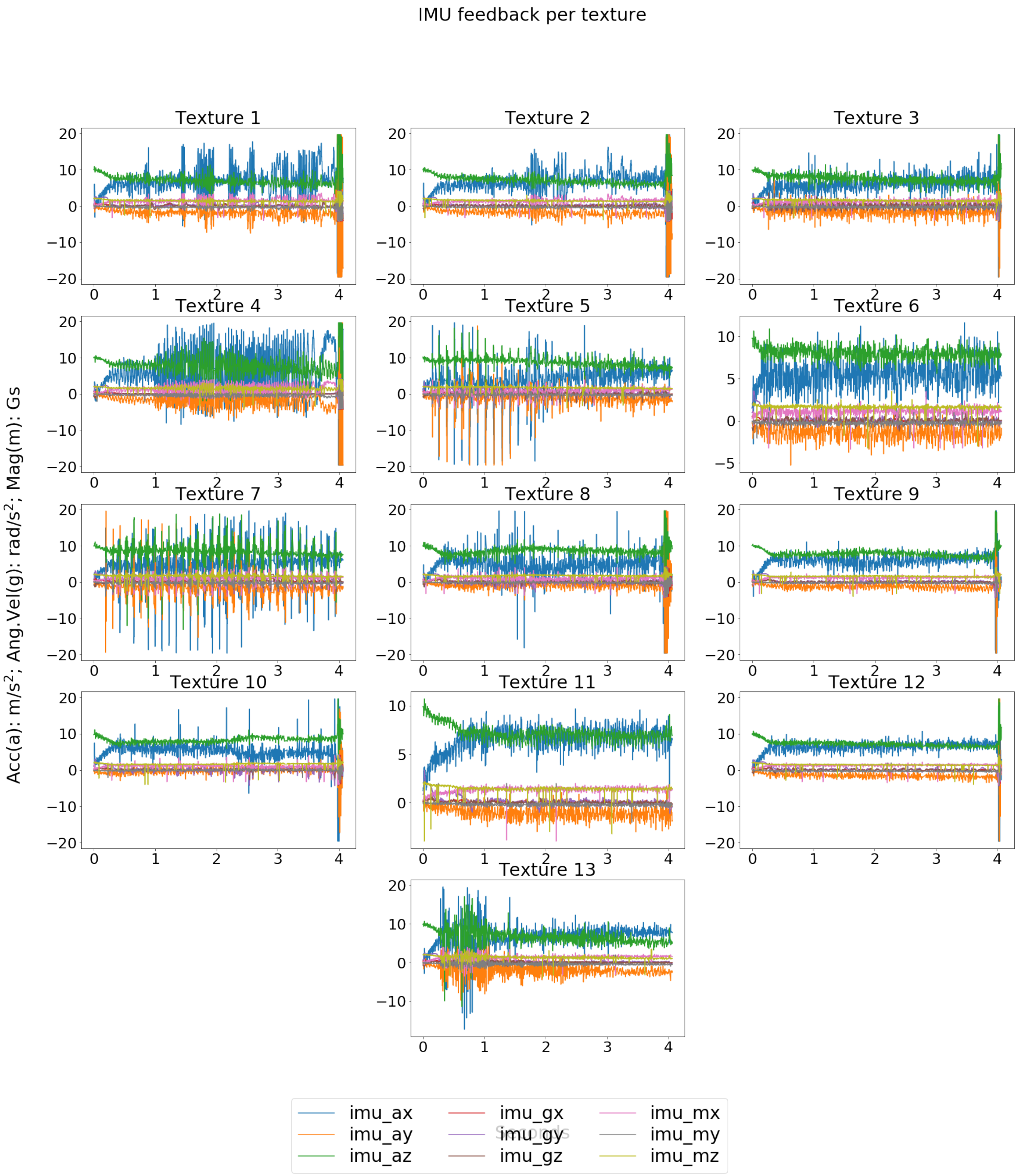

Figure 5.11: Data from the 9-DOF IMU for each texture: **acceleration** (imu_ax, imu_ay, and imu_az) measured in m/ss^2, **angular velocity** (imu_gx, imu_gy, and imu_gz) in rad/s, and **magnetic flux** (imu_mx, imu_my, and imu_mz) in Gauss.

Each feature was tested separately with each classifier. Table 5.1 shows the results from each classifier using each feature vector. The *Extra Trees* classifier outperformed all the other classifiers, achieving a maximum accuracy score of 98% (for the imu_gx feature) and a minimum of 90% accuracy score (with the imu_my feature). The second best was the *SVM* classifier that achieved an accuracy score of 98% (for the imu_gx feature) and a minimum of 84% (for the imu_my feature). The third best was the *Random Forest* classifier (a maximum of 96% for im_ gz and a minimum of 85% for imu_my). Following that, the *MLP* classifier achieved a maximum of 95% (for imu_gx) and a minimum of 64 % (for imu_my). The *kNN* classifier performed poorly and was not included in the table.

The feature that produced the most reliable precision was the angular velocity on the X-axis (imu_gx), and the less accurate feature was the magnetic flux on the Y-axis (imu_my). A sum of all the average accuracy score was done to compare the influence that each feature has in the classification. Figure 5.12 shows the influence that each feature vector had in the classification process.

Table 5.1: Accuracy score of texture classification per classifier and features.

Features	***Extra Trees***	*Random Forest*	*SVM*	*MLP*
baro	94%	91%	92%	88%
imu_ax	95%	91%	89%	73%
imu_ay	91%	89%	85%	71%
imu_az	96%	95%	96%	77%
imu_gx	**98%**	95%	**98%**	**95%**
imu_gy	95%	92%	97%	91%
imu_gz	97%	**96%**	97%	93%
imu_mx	95%	91%	85%	71%
imu_my	90%	85%	84%	64%
imu_mz	94%	94%	87%	69%
Max. Acc.	98%	96%	98%	95%
Min. Acc.	90%	85%	84%	64%
Ave. Acc.	**95%**	92%	91%	88%
Best Feature	imu_gx	imu_gz	imu_gx	imu_gx

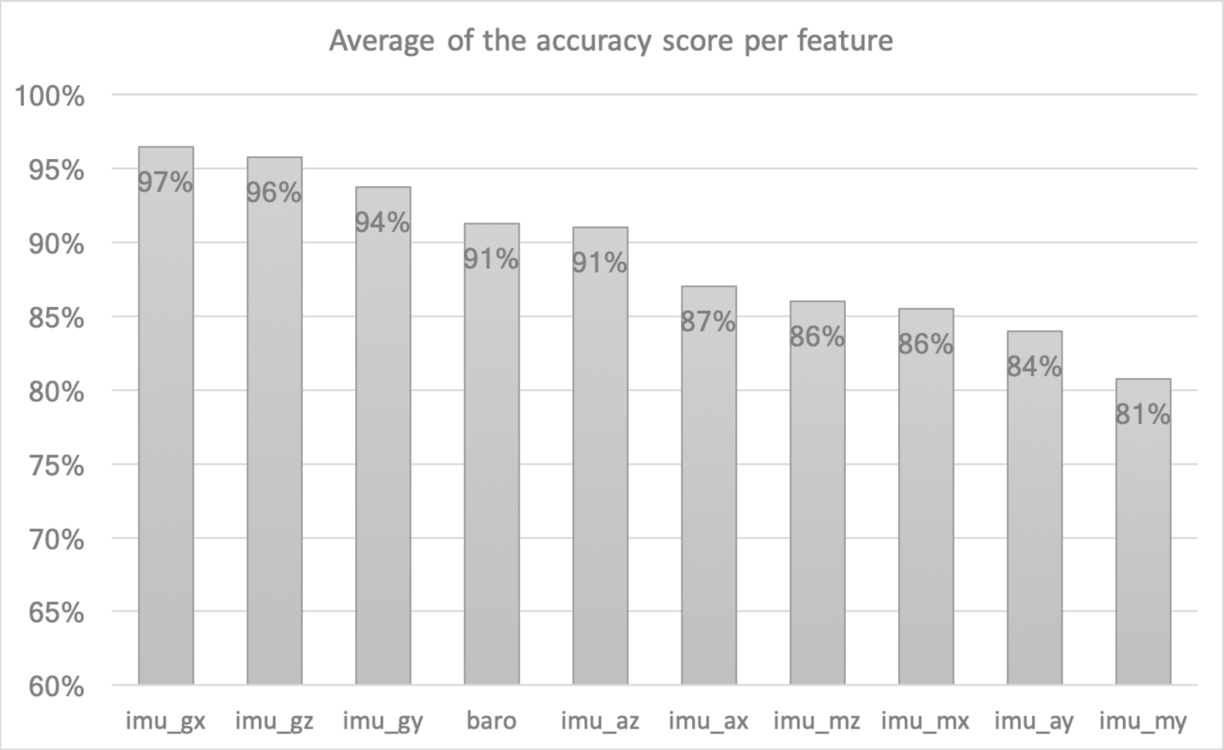

Figure 5.12: Features influence in the classification process. The imu_gx outperformed the other features and the imu_my was the least influential.

The *Extra Trees*' confusion matrix is shown in Figure 5.13. Textures 01, 03, 04, 05, 10, 11, 12 and 13 were correctly classified in 100% of the cases. Texture 08 was misclassified as texture 09 once (and vice-versa), which was expected since its materials are similar. Unexpectedly, texture 07 was misclassified as textures 05 and 06, even though it had uniform bumps. Interestingly, all the soft textures were classified correctly. Finally, texture 02 was incorrectly labelled as texture 08.

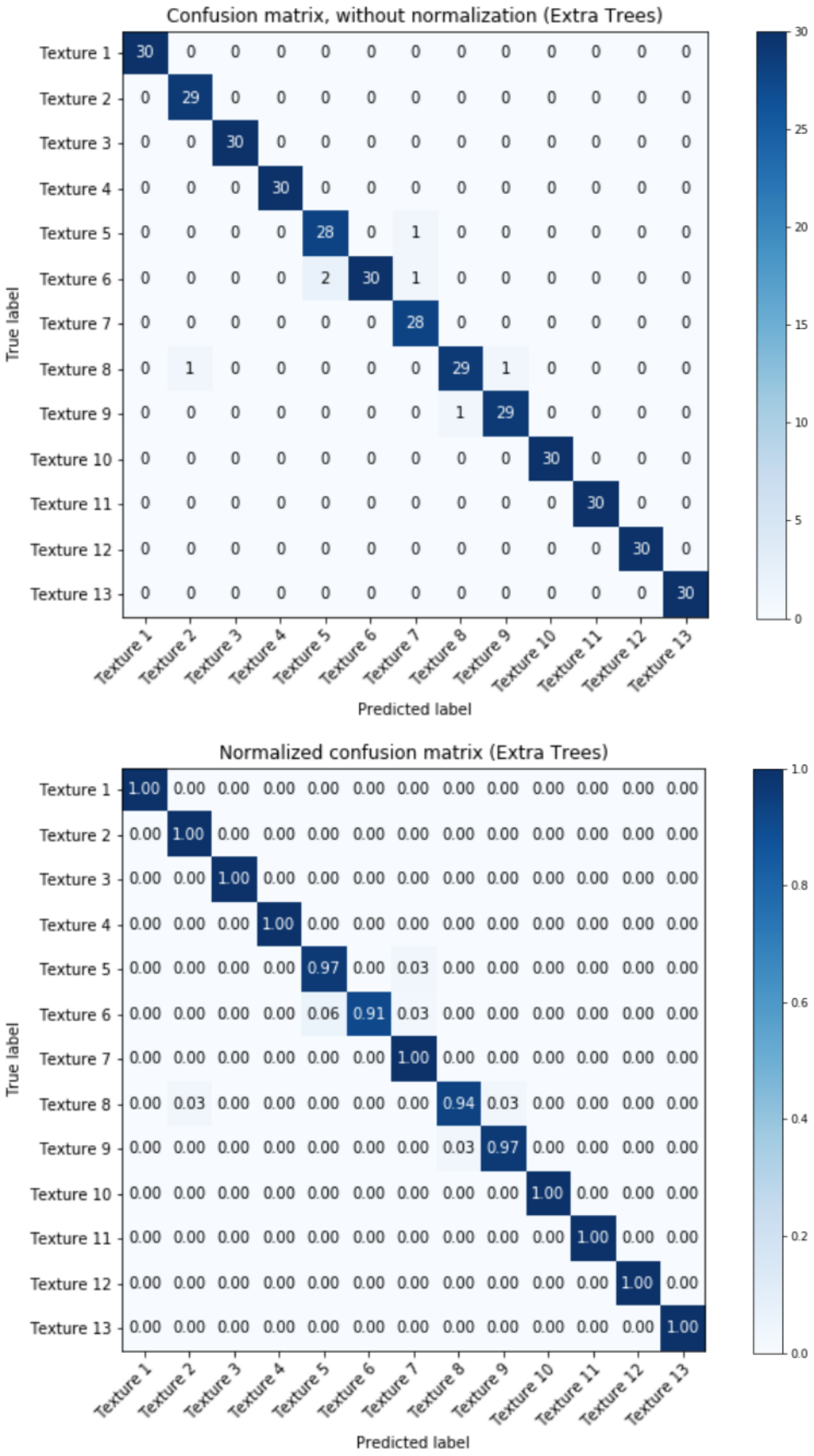

Confusion matrix, without normalization (Extra Trees)

True label \ Predicted label	Texture 1	Texture 2	Texture 3	Texture 4	Texture 5	Texture 6	Texture 7	Texture 8	Texture 9	Texture 10	Texture 11	Texture 12	Texture 13
Texture 1	30	0	0	0	0	0	0	0	0	0	0	0	0
Texture 2	0	29	0	0	0	0	0	0	0	0	0	0	0
Texture 3	0	0	30	0	0	0	0	0	0	0	0	0	0
Texture 4	0	0	0	30	0	0	0	0	0	0	0	0	0
Texture 5	0	0	0	0	28	0	1	0	0	0	0	0	0
Texture 6	0	0	0	0	2	30	1	0	0	0	0	0	0
Texture 7	0	0	0	0	0	0	28	0	0	0	0	0	0
Texture 8	0	1	0	0	0	0	0	29	1	0	0	0	0
Texture 9	0	0	0	0	0	0	0	1	29	0	0	0	0
Texture 10	0	0	0	0	0	0	0	0	0	30	0	0	0
Texture 11	0	0	0	0	0	0	0	0	0	0	30	0	0
Texture 12	0	0	0	0	0	0	0	0	0	0	0	30	0
Texture 13	0	0	0	0	0	0	0	0	0	0	0	0	30

Normalized confusion matrix (Extra Trees)

True label \ Predicted label	Texture 1	Texture 2	Texture 3	Texture 4	Texture 5	Texture 6	Texture 7	Texture 8	Texture 9	Texture 10	Texture 11	Texture 12	Texture 13
Texture 1	1.00	0.00	0.00	0.00	0.00	0.00	0.00	0.00	0.00	0.00	0.00	0.00	0.00
Texture 2	0.00	1.00	0.00	0.00	0.00	0.00	0.00	0.00	0.00	0.00	0.00	0.00	0.00
Texture 3	0.00	0.00	1.00	0.00	0.00	0.00	0.00	0.00	0.00	0.00	0.00	0.00	0.00
Texture 4	0.00	0.00	0.00	1.00	0.00	0.00	0.00	0.00	0.00	0.00	0.00	0.00	0.00
Texture 5	0.00	0.00	0.00	0.00	0.97	0.00	0.03	0.00	0.00	0.00	0.00	0.00	0.00
Texture 6	0.00	0.00	0.00	0.00	0.06	0.91	0.03	0.00	0.00	0.00	0.00	0.00	0.00
Texture 7	0.00	0.00	0.00	0.00	0.00	0.00	1.00	0.00	0.00	0.00	0.00	0.00	0.00
Texture 8	0.00	0.03	0.00	0.00	0.00	0.00	0.00	0.94	0.03	0.00	0.00	0.00	0.00
Texture 9	0.00	0.00	0.00	0.00	0.00	0.00	0.00	0.03	0.97	0.00	0.00	0.00	0.00
Texture 10	0.00	0.00	0.00	0.00	0.00	0.00	0.00	0.00	0.00	1.00	0.00	0.00	0.00
Texture 11	0.00	0.00	0.00	0.00	0.00	0.00	0.00	0.00	0.00	0.00	1.00	0.00	0.00
Texture 12	0.00	0.00	0.00	0.00	0.00	0.00	0.00	0.00	0.00	0.00	0.00	1.00	0.00
Texture 13	0.00	0.00	0.00	0.00	0.00	0.00	0.00	0.00	0.00	0.00	0.00	0.00	1.00

Figure 5.13: *Extra Trees* classification with a 98% average accuracy score using the x-axis angular velocity feature (imu_gx).

5.3.8 Discussion

Preliminary processing is a common practice in this area of research, and it is done to enhance the classification's accuracy. For example, [123] used variance, skewness, and kurtosis to produce a more concise dataset, and [153] transformed the data from the temporal domain to the frequency domain. However, the raw tactile data were largely adequate for practical texture classification, using high dimension tactile feature vectors.

The features that influenced the most in the classification process were, in order: imu_gx, imu_gz, imu_gy, barometer, imu_az, imu_ax, imu_mz, imu_mx, imu_ay, and imu_my. This result was unexpected since the imu_gy was assumed to be the most critical feature for the stimuli along the X-direction (as discussed in Section 5.2). Therefore, it is clear how complex the tactile data is and, in mathematical terms, trying to predict which feature would be the best is nontrivial. These results reinforce the concept of data-driven classification.

Another significant find was that the moving direction used during the tactile exploration is particularly important and must be considered as a variable; hence, this is a motivation to dynamically explore the texture in two dimensions, presented in Section 5.4.

5.4 Two-Dimensional Exploration and Texture Classification Using an Articulated Tactile-Enabled Robotic Finger with Hemispherical Fingertip

5.4.1 Summary

The experimental results of the one-dimensional dynamic surface exploration, discussed in Section 5.3.8, have shown that the moving direction of the exploring fingertip is a critical variable to be considered in dynamic exploration tasks. It was also found that the flat fingertip was not suitable to dynamically explore textures, due to its peculiar, tip-edge contact style. Hence, this section aims to experimentally study the two-dimensional surface exploration and texture classification using the more versatile hemispherical fingertip. The following classifiers were used: *SVM*, *MLP*, *Random Forest*, and *Extra Trees*.

5.4.2 Textures

Twelve textures, the same as the ones used in the 1D exploration, are shown in Figure 5.14. They were labelled accordingly to match the labels used in the 1D experiment.

The textures were glued on a medium-density fibreboard (MDF) cut in twelve squares with a length of 10 cm.

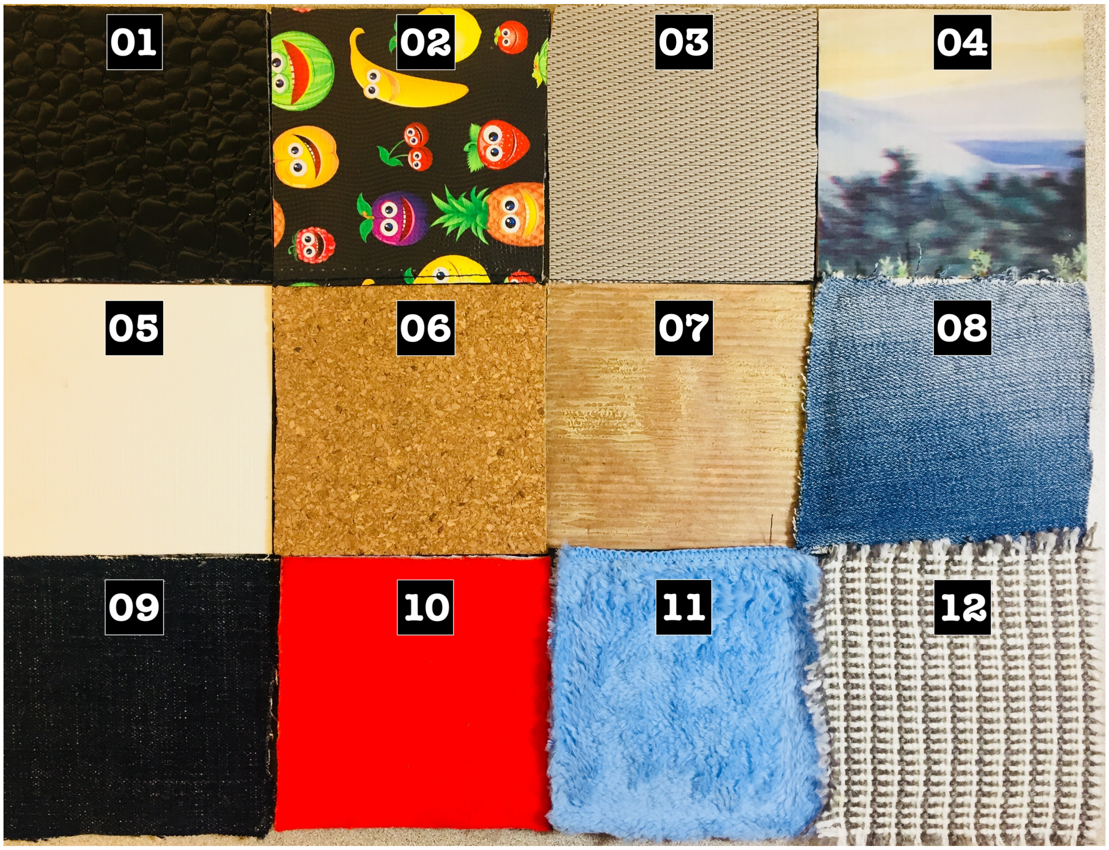

Figure 5.14: The textures, labelled from 1 to 12, used in the 2D explorations.

5.4.3 Experimental Setup

The articulated robotic finger used in these experiments had a hemispherical fingertip on top of the miniaturized tactile sensor, as shown in Figure 5.1. The rounded shape of the fingertip allowed for a more efficient 2D exploration of the textures.

The textures used in this experiment were the same as the ones used in the linear exploration. The textures were attached to the pen-carrier of an XY-recorder, shown in Figure 5.15 so that they can perform two-dimensional movements. A microcontroller was used to control the velocity and the 2D position of the XY-recorder employed to move the explored textured surface.

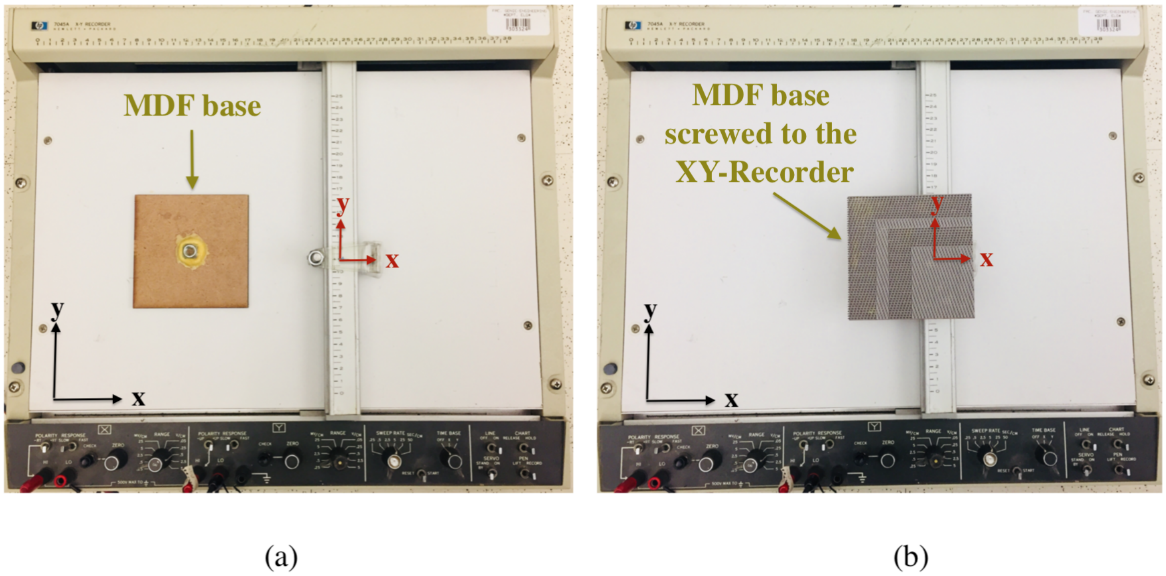

Figure 5.15: The XY-recorder with its frame of reference in black and the texture's frame of reference in red: (a) MDF base, and (b) XY-recorder placed on the recorder's pen-carrier.

As shown in Figure 5.16, the distal phalanx of the robotic finger was set in a downward position, connected to the middle phalanx via a distal interphalangeal joint powered by a computer-controlled motor. The middle phalanx was mounted onto a rigid mechanical structure. After making contact with the textured surface (mounted on the XY-recorder) by rotating the distal joint, the robotic finger did not move anymore. The XY-recorder moved the texture in a squared motion, while the finger remained in a static position. This arrangement lets the static fingertip to explore the texture that moves underneath in two dimensions dynamically. One hundred trials for each texture were made at three different velocities (30 mm/s, 35 mm/s, and 40 mm/s), for a total of 300 trials per texture.

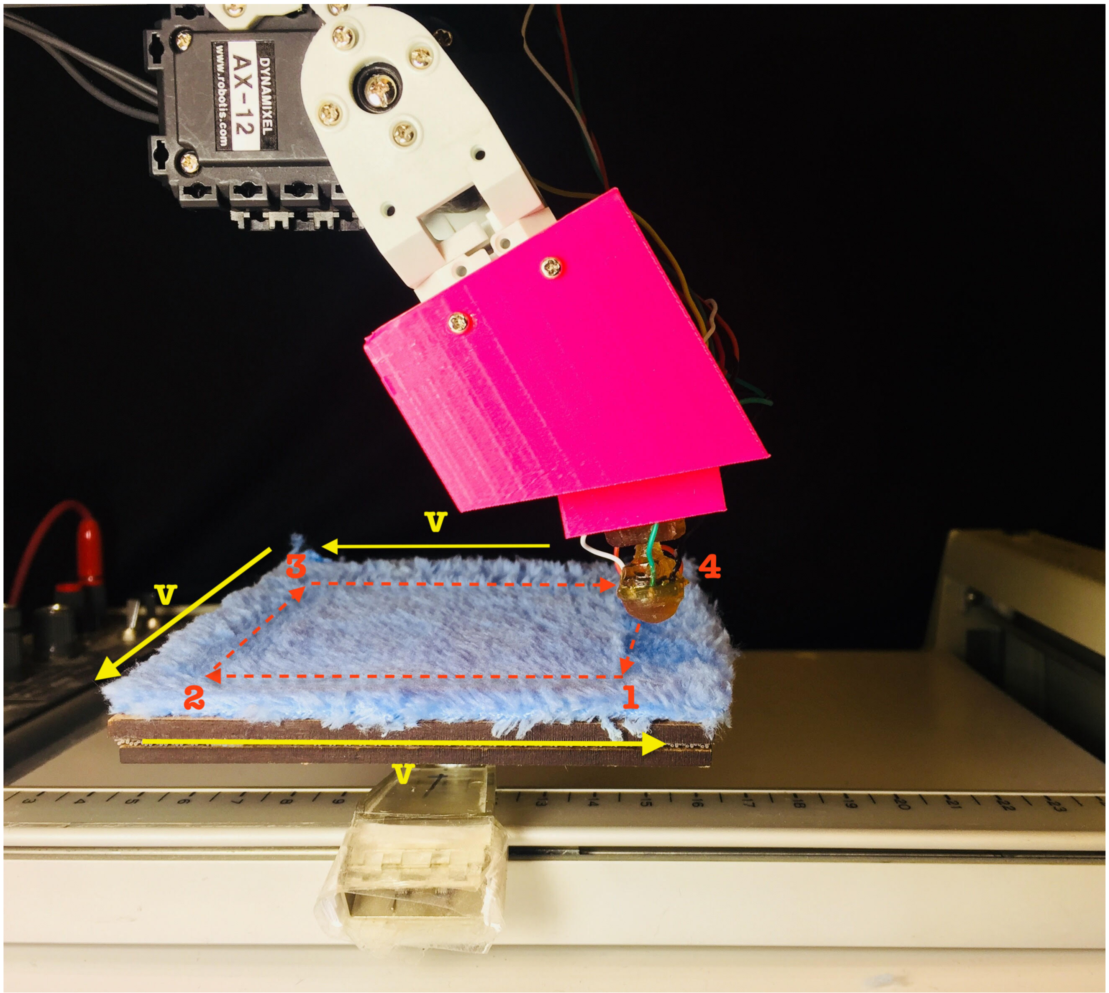

Figure 5.16: Two-dimensional exploration of textures using the articulated robotic finger with hemispherical fingertip. The textured surface moved at a constant velocity, v (30 mm/s, 35 mm/s, or 40 mm/s). The fingertip remained static, while the XY-recorder moved the textured surface so that the fingertip passed through the points 1, 2, 3, 4, and then back to 1, completing one cycle..

5.4.4 Methodology and Data Acquisition

The dynamic exploration started by rotating the fingertip downwards until it touched the texture's surface. A pressure threshold, empirically chosen, determined when the finger would stop. A small torque had to be maintained active in order to ensure that the fingertip maintained proper contact with the texture during the experiment.

Each trial involved a complete cycle of exploration, as shown in Figure 5.16. A total of 3,600 samples were recorded (1,200 for each velocity used) in ROS bags. The barometer and IMU data collected for each texture are shown in 5.17 and Figure 5.18 for an exploratory velocity of 30 mm/s. The IMU and barometer data at a velocity of 35 mm/s and 40 mm/s are available in Appendix A.

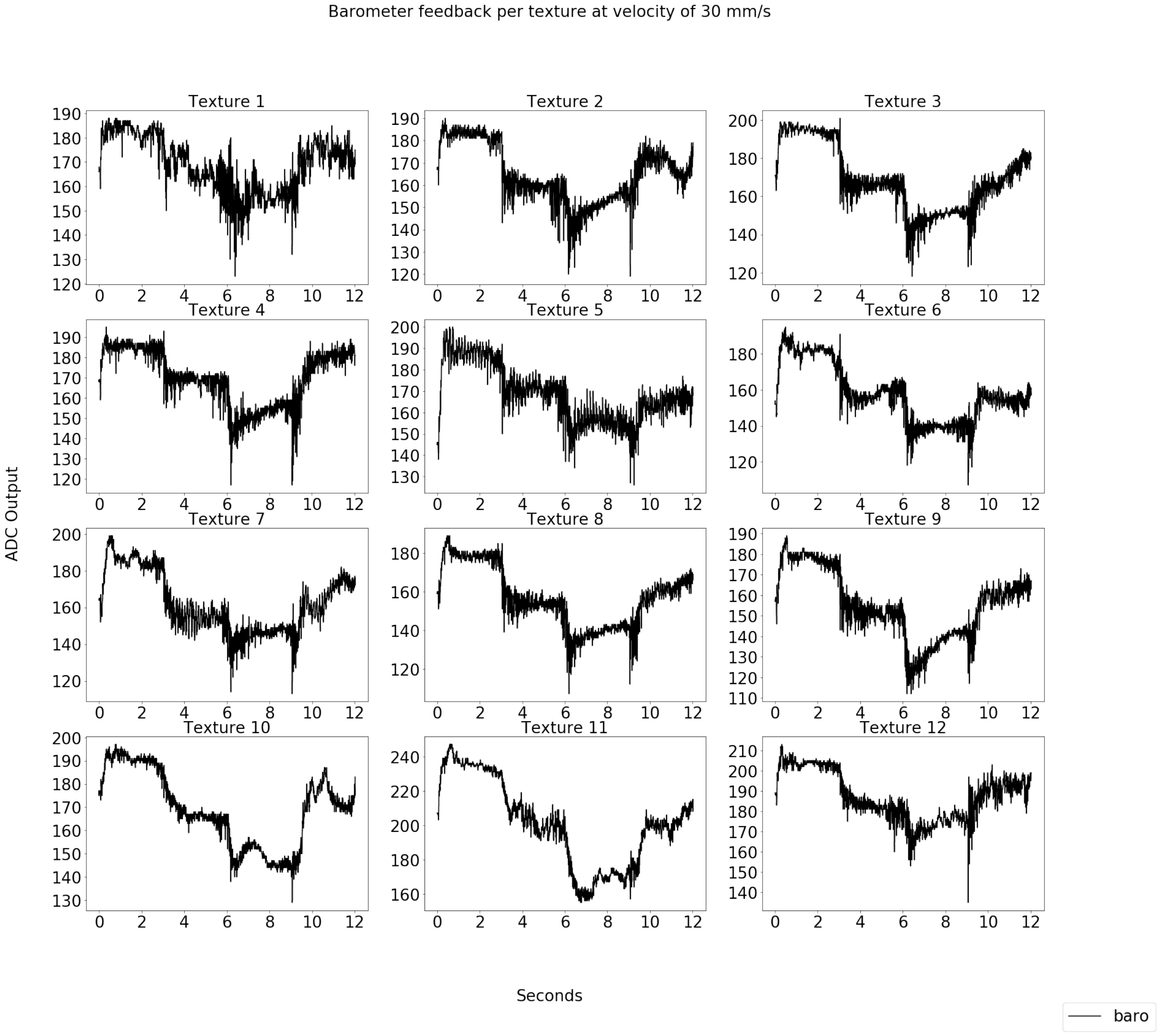

Figure 5.17: Barometer data collected for each texture during a 2D dynamic exploration at an exploratory velocity of 30 mm/s.

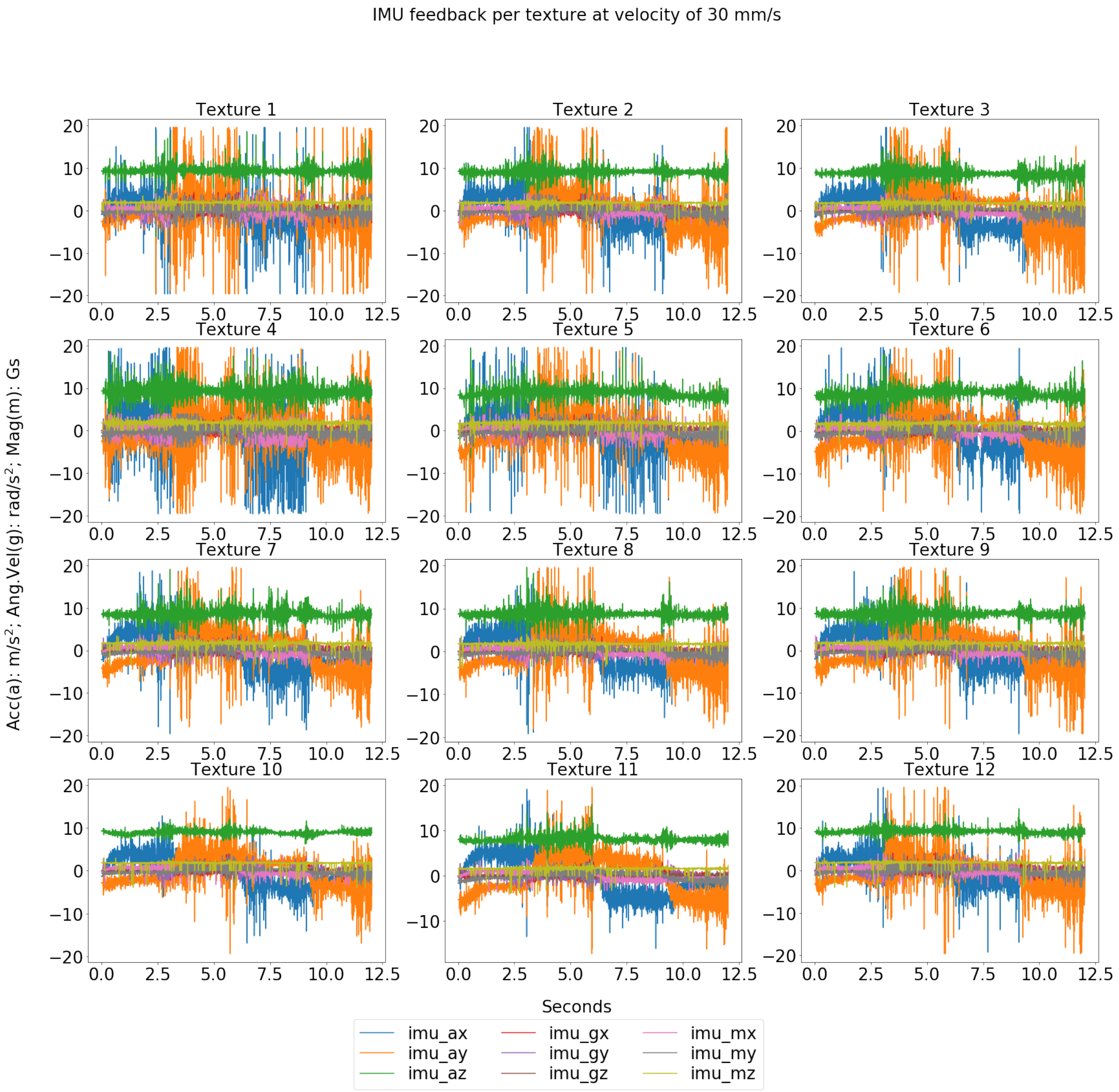

Figure 5.18: IMU data collected for each texture during a 2D dynamic exploration at an exploratory velocity of 30 mm/s.

5.4.5 Data Processing

The barometer and the IMU operated at an average frequency of 350 Hz and 1,500 Hz, respectively. The signals were recorded at a frequency of 3,000 Hz, assuring that no data was lost.

Let $A_{i,j,t,T}$ be the feature vector for each exploratory velocity, where i correspond to a transducer, j to an exploratory velocity, t the respective trial, and T the texture explored; $i \in \{\text{baro, imu\_ax, imu\_ay, imu\_az, imu\_gx, imu\_gy, imu\_gz, imu\_mx, imu\_my, imu\_mz}\}$,$j \in \{30, 35, 40\}$, and $t \in \{1, 2, ..., 100\}$, and $T \in \{01, 02, ..., 12\}$. For instance, $A_{baro,40,3,10}$ represents the feature vector coming from the barometer, after the third trial done on texture 10, at an exploratory velocity of 40 mm/s.

Each rosbag file had ten feature vectors. Therefore,

$$
\begin{aligned}
&rosbag_{j,t,T} = [A_{i,j,t,T}] \\
&j \in \{30, 35, 40\} \\
&t \in \{1, 2, ..., 100\} \\
&T \in \{1, 2, ..., 12\}
\end{aligned}
$$

The size of each rosbag had a size of approximately 37000, 31500, 26000, for the velocities of 30 mm/s, 35 mm/s, and 40 mm/s, respectively.

$$
\begin{aligned}
rosbag_{30,t,T} &= [A_{i,30,t,T}]_{10x37000} \\
rosbag_{35,t,T} &= [A_{i,35,t,T}]_{10x31500} \\
rosbag_{40,t,T} &= [A_{i,40,t,T}]_{10x26000}
\end{aligned}
$$

The size of each rosbag file, however, slightly differed. Hence, the minimum vector size of all the rosbags, for each velocity, was calculated, and all rosbags were resized.

$$\min_{\{i,t,T\}} ||A_{i,30,t,T}|| = 35910$$

$$\min_{\{i,t,T\}} ||A_{i,35,t,T}|| = 31237$$

$$\min_{\{i,t,T\}} ||A_{i,40,t,T}|| = 24085$$

The resized rosbags are represented as $rosbag^*$.

$$rosbag^*_{30,t,T} = [A_{i,30,t,T}]_{10x35910}$$

$$rosbag^*_{35,t,T} = [A_{i,35,t,T}]_{10x31237}$$

$$rosbag^*_{40,t,T} = [A_{i,40,t,T}]_{10x24085}$$

Subsequently, all the feature vectors were separated and concatenated into a Python-specific pickle file. Let the input vectors used by the classifiers be I. An input vector for the data collected at a velocity of 30 mm/s by the barometer is exemplified bellow.

$$I_{baro,30} = [[A_{baro,30}]_{1200x35910} \quad TL_{1200x1}]$$

where TL is the target label, $TL_i \in \{1, 2, ...12\}$, $i = 1, 2, ...1200$

Each classification used an input vector originated by a feature vector at a given velocity. There were 30 input vectors, one for each feature at a given velocity.

5.4.6 Classifiers' Settings

The classifiers' settings for the 2D exploration were identical to the settings used in the 1D exploration, shown in Section 5.3.6.

5.4.7 Results

The texture exploration was done in the XY-plane. Each trial had four ranges of time, going along the IMU's Cartesian coordinates. The first range (0 to 3 seconds) was performed along the positive X-axis; the second range (3 to 6 seconds) was done along the positive Y-axis; the third range (6 to 9 seconds) was completed along the negative X-axis; and the fourth range (9 to 12 seconds) was done along the negative Y-axis. The ranges mentioned above were for an exploratory velocity of 30 mm/s.

Analyzing the barometer data, from Figure 5.17, four different aspects are noted for each graph. Clearly, each trend represents an exploratory movement done in a different direction. The output difference between the ranges are explained in Section 5.2, since the sensor reacts differently in each direction to external stimuli.

A primary inspection of the barometer data indicates consistency in the tactile output. As expected, textures 05 and 07 produced uniform spiked outputs, while texture 01 exhibited nonuniform feedback. Textures 08 and 09 resulted in similar trends since they are akin jeans material. Textures 10 and 11 produced smoother outputs that are notably from soft materials. Textures 02, 03 and 04 outputs show anisotropy.

Even though it is possible to notice different trends produced by the IMU (Figure 5.17), it is not simple to identify the physical aspects of the data directly.

The classification results are shown in Table 5.2 for an exploratory velocity of 30 mm/s, in Table 5.3 for an exploratory velocity of 35 mm/s, and in Table 5.4 for an exploratory velocity of 40 mm/s.

The *SVM* classifier outperformed the other classifiers with an overall accuracy of 99.1% and 99.3% for the explorations at a velocity of 30 mm/s and 35 mm/s, respectively. How-

Table 5.2: Accuracy score of texture classification per classifier and features at an exploratory velocity of 30 mm/s

Features	*Extra Trees*	*Random Forest*	***SVM***	*MLP*
baro	**100%**	**100%**	**100%**	**100%**
imu_ax	98.1%	97.2%	99.4%	96.4%
imu_ay	99.7%	99.1%	98.6%	95.5%
imu_az	99.7%	98.9%	**100%**	96.1%
imu_gx	98.6%	98.1%	98.1%	95.6%
imu_gy	97.8%	96.9%	98.6%	95.2%
imu_gz	**100%**	99.2%	99.7%	99.4%
imu_mx	99.4%	97.5%	99.2%	91.7%
imu_my	90.6%	97.2%	97.2%	93.9%
imu_mz	**100%**	99.7%	99.7%	91.7%
Max. Acc.	100%	100%	100%	100%
Min. Acc.	90.6%	96.9%	97.2%	91.7%
Ave. Acc.	98.4%	98.4%	**99.1%**	95.6%
Best Feature	baro imu_gz imu_mz	baro	baro imu_az	baro

Table 5.3: Accuracy score of texture classification per classifier and features at an exploratory velocity of 35 mm/s

Features	*Extra Trees*	*Random Forest*	***SVM***	*MLP*
baro	**100%**	**100%**	**100%**	**99.7%**
imu_ax	98.9%	99.1%	99.7%	92.8%
imu_ay	99.2%	99.2%	98.9%	94.2%
imu_az	99.7%	99.4%	99.4%	95.0%
imu_gx	98.6%	98.6%	99.4%	95.6%
imu_gy	97.2%	97.2%	98.1%	95.8%
imu_gz	99.4%	99.7%	99.4%	99.3%
imu_mx	99.7%	99.7%	99.7%	93.6%
imu_my	98.3%	96.9%	99.7%	95.3%
imu_mz	98.9%	98.3%	99.2%	93.1%
Max. Acc.	100%	100%	100%	95%
Min. Acc.	97.2%	96.9%	98.1%	92.8%
Ave. Acc.	99.0%	98.8%	**99.3%**	95.4%
Best Feature	baro	baro	baro	baro

Table 5.4: Accuracy score of texture classification per classifier and features at an exploratory velocity of 40 mm/s

Features	***Extra Trees***	*Random Forest*	*SVM*	*MLP*
baro	99.4%	**99.4%**	**100%**	**99.4%**
imu_ax	99.4%	99.2%	98.6%	93.1%
imu_ay	99.4%	98.6%	98.3%	90.6%
imu_az	**99.7%**	99.2%	99.7%	95.6%
imu_gx	99.2%	98.9%	99.4%	98.3%
imu_gy	98.9%	98.6%	98.9%	98.9%
imu_gz	**99.7%**	99.2%	99.7%	99.2%
imu_mx	**99.7%**	**99.4%**	99.2%	89.2%
imu_my	99.2%	97.8%	99.4%	89.4%
imu_mz	**99.7%**	98.9%	98.6%	91.1%
Max. Acc.	99.7%	99.4%	100%	99.4%
Min. Acc.	98.9%	98.6%	98.3%	89.4%
Ave. Acc.	**99.4%**	98.9%	99.2%	94.5%
Best Feature	imu_az imu_gz imu_mx imu_mz	baro imu_mx	baro	baro

ever, the *Extra Trees* classifier provided the best results, with an overall accuracy of 99.4%, for an exploratory velocity of 40 mm/s.

The feature that produced the most reliable precision was the barometer with 100% correct classification of textures, in most cases. The *SVM* confusion matrix for the barometer input is shown in Figure 5.19.

The average accuracy of all the classifiers per feature was calculated and it is presented in Figure 5.20.

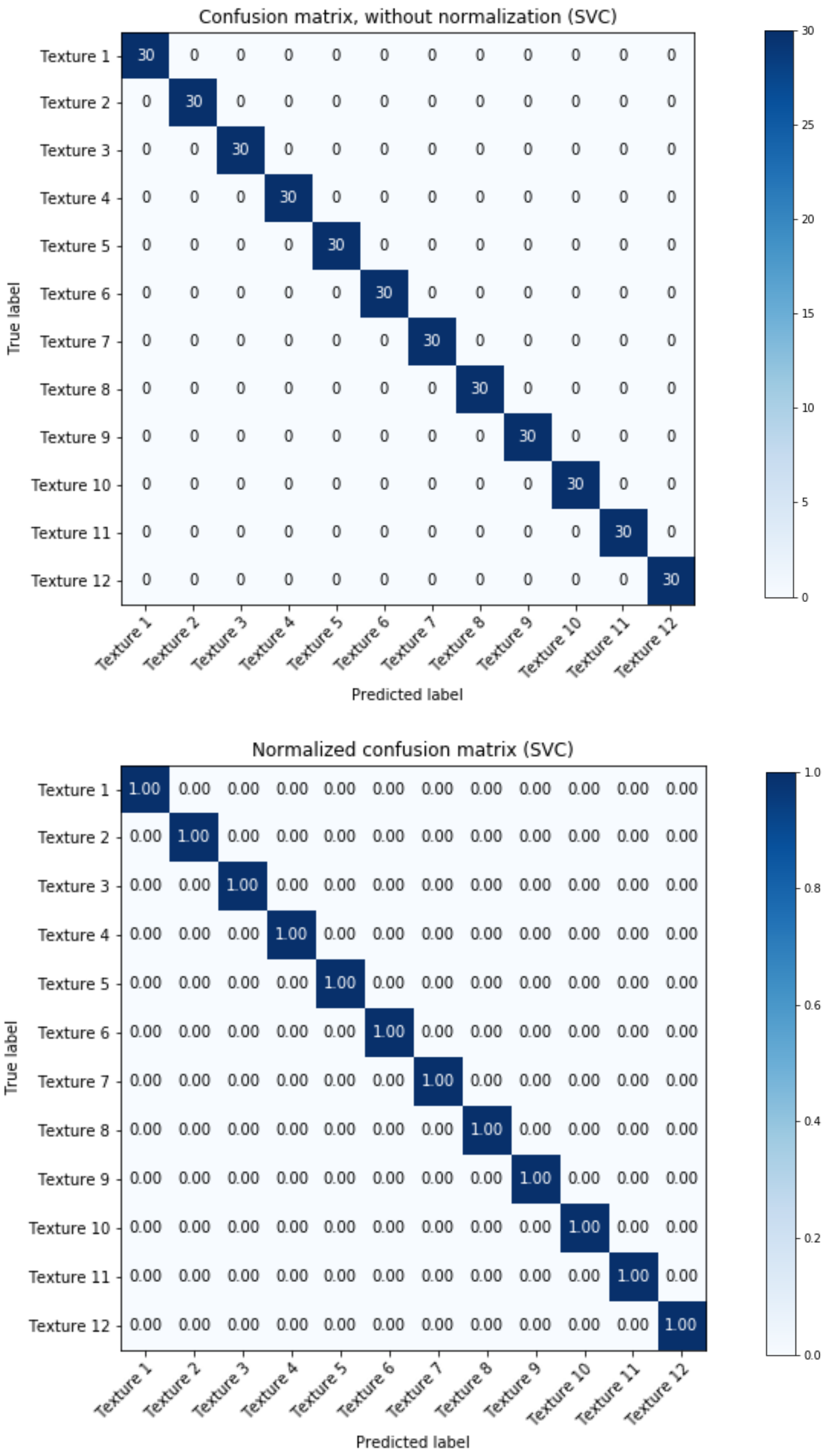

	Texture 1	Texture 2	Texture 3	Texture 4	Texture 5	Texture 6	Texture 7	Texture 8	Texture 9	Texture 10	Texture 11	Texture 12
Texture 1	30	0	0	0	0	0	0	0	0	0	0	0
Texture 2	0	30	0	0	0	0	0	0	0	0	0	0
Texture 3	0	0	30	0	0	0	0	0	0	0	0	0
Texture 4	0	0	0	30	0	0	0	0	0	0	0	0
Texture 5	0	0	0	0	30	0	0	0	0	0	0	0
Texture 6	0	0	0	0	0	30	0	0	0	0	0	0
Texture 7	0	0	0	0	0	0	30	0	0	0	0	0
Texture 8	0	0	0	0	0	0	0	30	0	0	0	0
Texture 9	0	0	0	0	0	0	0	0	30	0	0	0
Texture 10	0	0	0	0	0	0	0	0	0	30	0	0
Texture 11	0	0	0	0	0	0	0	0	0	0	30	0
Texture 12	0	0	0	0	0	0	0	0	0	0	0	30

	Texture 1	Texture 2	Texture 3	Texture 4	Texture 5	Texture 6	Texture 7	Texture 8	Texture 9	Texture 10	Texture 11	Texture 12
Texture 1	1.00	0.00	0.00	0.00	0.00	0.00	0.00	0.00	0.00	0.00	0.00	0.00
Texture 2	0.00	1.00	0.00	0.00	0.00	0.00	0.00	0.00	0.00	0.00	0.00	0.00
Texture 3	0.00	0.00	1.00	0.00	0.00	0.00	0.00	0.00	0.00	0.00	0.00	0.00
Texture 4	0.00	0.00	0.00	1.00	0.00	0.00	0.00	0.00	0.00	0.00	0.00	0.00
Texture 5	0.00	0.00	0.00	0.00	1.00	0.00	0.00	0.00	0.00	0.00	0.00	0.00
Texture 6	0.00	0.00	0.00	0.00	0.00	1.00	0.00	0.00	0.00	0.00	0.00	0.00
Texture 7	0.00	0.00	0.00	0.00	0.00	0.00	1.00	0.00	0.00	0.00	0.00	0.00
Texture 8	0.00	0.00	0.00	0.00	0.00	0.00	0.00	1.00	0.00	0.00	0.00	0.00
Texture 9	0.00	0.00	0.00	0.00	0.00	0.00	0.00	0.00	1.00	0.00	0.00	0.00
Texture 10	0.00	0.00	0.00	0.00	0.00	0.00	0.00	0.00	0.00	1.00	0.00	0.00
Texture 11	0.00	0.00	0.00	0.00	0.00	0.00	0.00	0.00	0.00	0.00	1.00	0.00
Texture 12	0.00	0.00	0.00	0.00	0.00	0.00	0.00	0.00	0.00	0.00	0.00	1.00

Figure 5.19: *SVM* texture classification with an 100% average accuracy score using the barometer data.

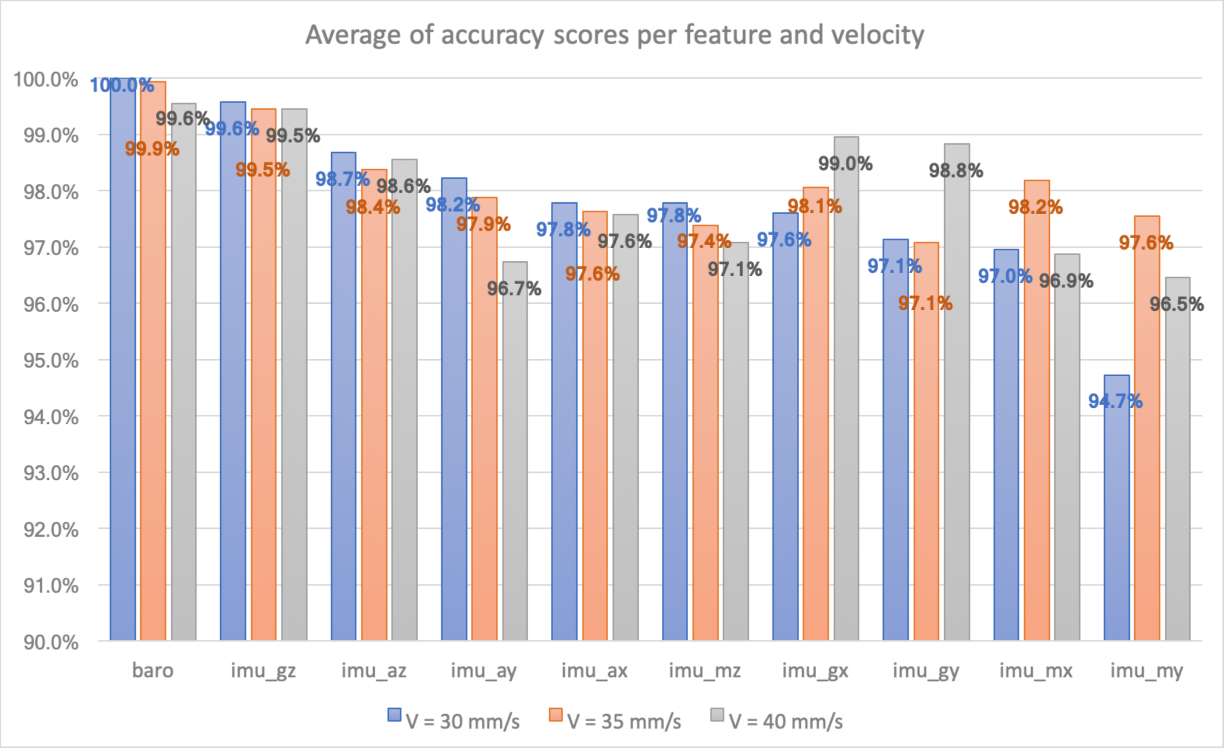

Figure 5.20: Features influence in the classification process for three velocities. No strong correlation could be found about the exploratory velocity and the classification accuracy for this range of velocities.

5.4.8 Discussion

Two significant findings emerged from this experiment. First, the classification performance was significantly higher in the 2D exploration than in the 1D exploration. This revealed the importance of exploring textures in more than one dimension. Second, no strong correlations were found by analyzing Figure 5.20. This suggests that the exploratory velocity was not a decisive factor in the texture classification for the range of velocities used.

High dimensional input vectors were used for the discussed classification techniques, even though they could not be suitable as input for traditional classification algorithms.

The classifier that produced the best accuracy was the *SVM* for exploratory velocities of 30 mm/s and 35 mm/s. However, for an exploratory velocity of 40 mm/s, the *Extra Trees* classifier performed better.

The barometer data produced the best classification result among all the exploratory velocities (except the classification done with *Extra Trees* at a velocity of 40 mm/s). A comparison between the best features produced from the 1D exploration and the ones from the 2D exploration did not reveal an overall best feature.

5.5 Conclusions

Two experiments were conducted to classify fine commonly used textures. The first experiment used an articulated tactile-enabled robotic finger with a flat fingertip to explore the textures in one dimension. The second experiment used the same robotic finger, but with a hemispherical fingertip. Each experiment produced relevant results and are summarized below.

One-dimensional exploration for texture classification

Among the classifiers used in this case, the *Extra Trees* classifier produced the most accurate classification, with an overall accuracy of 95%. The transducer that produced the most accurate classification was the IMU gyroscope in the X-axis (imu_gx), with an average accuracy of 97%. The results also showed a correct classification between two textures that were originated from the same anisotropic material. This indicated that the exploration in different directions produced distinctive outputs and, therefore, the exploration in two dimensions had to be analyzed. Finally, the exploration with the flat fingertip showed to be not efficient because of the problematic contact between the edge of the tactile sensor and the explored texture.

Two-dimensional exploration for texture classification

Three exploratory velocities were used in the 2D exploration: 30 mm/s, 35 mm/s, and 40 mm/s. Experiments have shown that the *SVM* classifier produced an overall classification accuracy of 99.1% and 99.3% for the velocities of 30 mm/s and 35 mm/s. The *Extra Trees* classifier reached an overall accuracy of 99.4% for the velocity of 40 mm/s. The barometer data produced the highest accuracy in almost all cases, achieving an accuracy of 100%. Two main findings resulted from this study: 1) the classification accuracy for the 2D exploration was substantially higher than the one obtained from the 1D exploration; 2) no strong correlation was found between the exploratory velocity and the classification of textures for the range of velocities used.

Chapter 6

Conclusions and Future Work

6.1 Conclusions

This thesis discusses the results of an experimental study of a novel tactile-enabled robotic fingertip able to perform static and dynamic tactile exploration of different object surfaces more efficiently. Two robotic fingertips (the equivalent to the human distal phalanx) versions were developed for static surface exploration applications: the version (discussed in Section 2.4.3) uses a multi-modal tactile sensor presented in [5], and the second version (discussed in Section 3.1) uses a miniaturized version of the tactile module.

Two versions of an articulated tactile-enabled robotic finger, consisting of a middle and a distal phalanx, were built: one for 1D dynamic explorations, and another for the 2D dynamic exploration of textured textures. The first finger had a flat fingertip, while the second had a semi-spherical fingertip based on the enhanced version of the miniaturized tactile module. Machine learning techniques (Support Vector Machine, Multilayer Perceptron, Random Forest, Extra Trees, and k-Nearest Neighbors) were used and compared for the classification of the explored textured surface patterns.

Static Surface Exploration for Heart Rate Detection

Static tactile exploration experiments using the multi-modal tactile-enabled robotic fingertip were carried out on the human skin (carotid artery located in the neck). Two experiments were conducted: the first used the fingertip with the original version of the tactile sensor, and the second used the fingertip with the miniaturized version of the tactile module.

The first experiment has discussed: (a) the measurement of the pulse when the human subject is in the rest state, and (b) the measurement of the heartbeat after 10 minutes of aerobic exercises. Both cases resulted in highly accurate values with a MAE of 0.4 bpm and 3.8 bpm, respectively. In the second situation, the high respiration rate and the nonuniformity of the heartbeats caused some interference in the heart rate calculation.

The second experiment used the first version of the tactile module and its miniaturized version. The results had a MAE of 1.67 bpm and 1.47 bpm, respectively.

The studies have shown that the robotic fingertip is indeed capable of measuring the pulse rate accurately by exploring the skin on the human subject's neck.

Dynamic Surface Exploration for Texture Classification

Experiments on 1D dynamic surface exploration for texture classification were carried out using the articulated tactile-enabled finger (similar to the middle and distal phalanges of a human finger) with a flat fingertip. Different machine learning classifiers were used, and the results showed that the Extra Trees classifier outperform the others, achieving an overall accuracy of 95%. The transducer that produced the best result was the gyroscope in the X-axis (imu_gx), with an accuracy of 95%. The experimental results led to two conclusions: (1) the exploration by a flat fingertip is not efficient, and (2) anisotropic texture materials may lead to different classifications results if explored in different directions, and hence 2D texture explorations need to be studied.

Experiments on 2D dynamic surface exploration for texture classification were carried out for three different exploratory velocities: 30 mm/s, 35 mm/s, and 40 mm/s. The articulated robotic finger used was identical with the one used for 1D exploration, but it was provided with a more versatile semi-spherical fingertip. The SVM classifier outperformed the other classifiers, at exploratory velocities of 35 mm/s and 40 mm/s, resulting in an overall accuracy of 99.1% and 99.3%, respectively. At a velocity of 40 mm/s, the Extra Trees classifier produced the most precise classification of 99.4%. The transducer that produced the best result was the barometer, with an accuracy of 100%. The results from the 2D dynamic explorations resulted in two significant findings: (1) the results achieved by the 2D dynamic explorations were substantially more precise than the results from the 1D explorations, and (2) no strong correlation was found between the exploratory velocity and the accuracy of the textures classification for the range of velocities used.

6.2 Suggestions for Future Work

Several aspects of the experimental research presented in this thesis could be suitable candidates for future development:

Tactile Sensor Module:

Even though the multi-modal tactile sensor was miniaturized, it is still not small enough for human-like skin deployment. The sensor should be further miniaturized and then embedded into a compliant artificial skin.

Heart Rate Measurement:

The IMU data could be used to determine if the device has an appropriate contact with the skin. Moreover, real-time pulse measurements could be further developed. Lastly, more efficient peak detection algorithms could be used to calculate the heartbeat.

Data Processing for Texture Classification:

The high dimensionality of the data used by the machine learning methods are not optimal and, therefore, could be improved by using DWT to reduce the noise and PCA to reduce the data dimensionality.

The input vectors had to be compressed in order to have the same length. Instead, a feature extraction from arbitrary length samples could be used to arrive at a fixed-length feature vector (e.g. Hidden Markov Model, Recurrent Neural Network, or Long Short-Term Memory).

Another challenge would be to find more suitable hyperparameter parameters for the classifiers. That could be done by using the k-fold cross-validation statistical method. Another advantage of this approach is that the estimated accuracy would also have a report with confidence intervals. Finally, different kernel functions could be used to determine the most suitable for texture classification.

Another improvement could be obtained by integrating the multi-modal transducers' data and utilize them as input vectors for the classification. Determining which transducer would produce the best results would be an interesting challenge.

APPENDICES

Appendix A

Data Collected from the 2D Dynamic Exploration at Velocities of 35 mm/s and 40 mm/s

This appendix presents the data collected from the 2D exploration experiments discussed in Section 5.4.

The barometer data collected for each texture are shown in Figure A.1 and Figure A.2 for an exploration velocity of 35 mm/s and 40 mm/s, respectively.

The IMU data collected for each texture are shown in Figure A.3 and Figure A.4 for an exploration velocity of 35 mm/s and 40 mm/s, respectively.

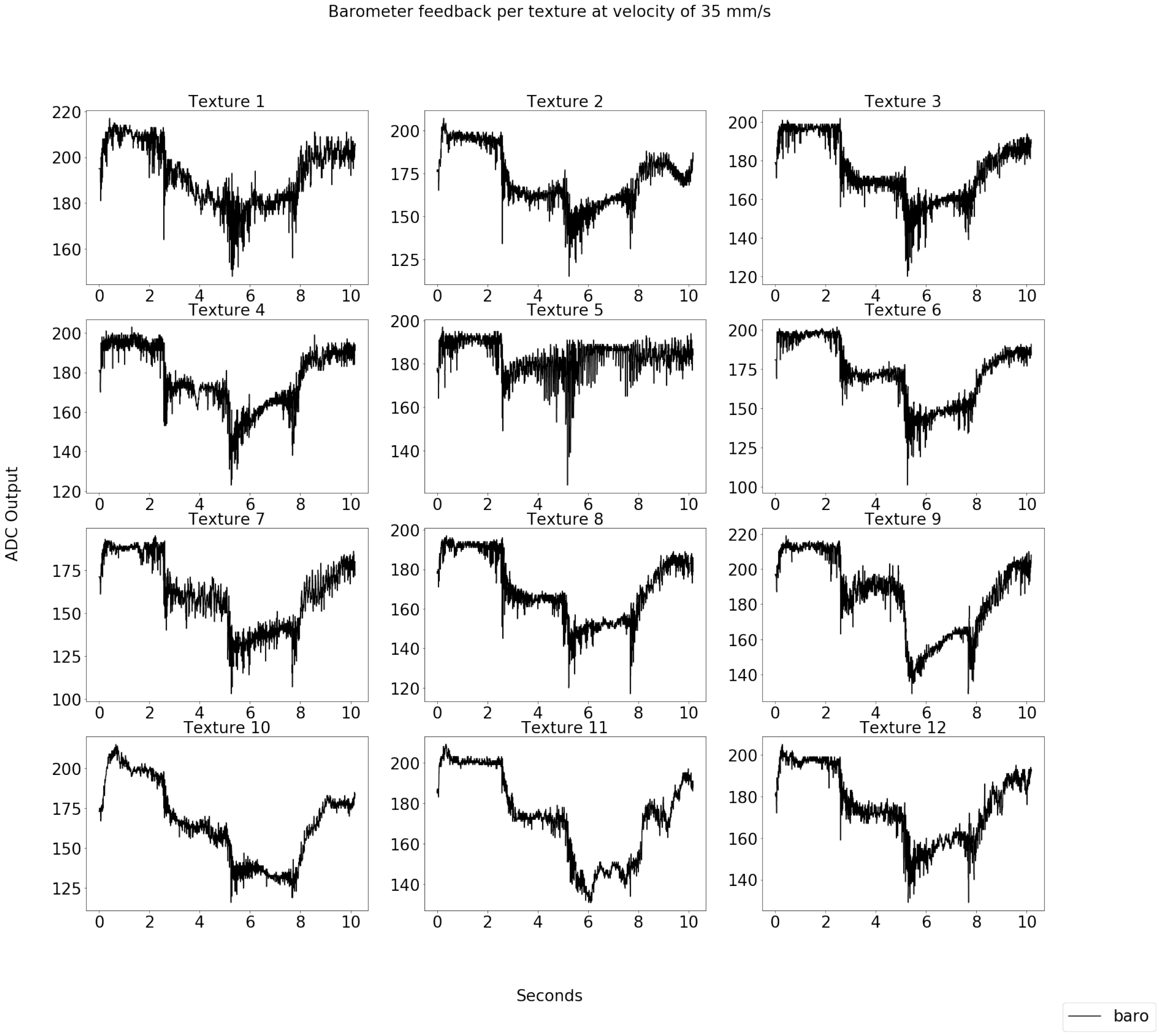

Figure A.1: Barometer data collected for each texture in a 2D dynamic exploration at an exploration velocity of 35 mm/s.

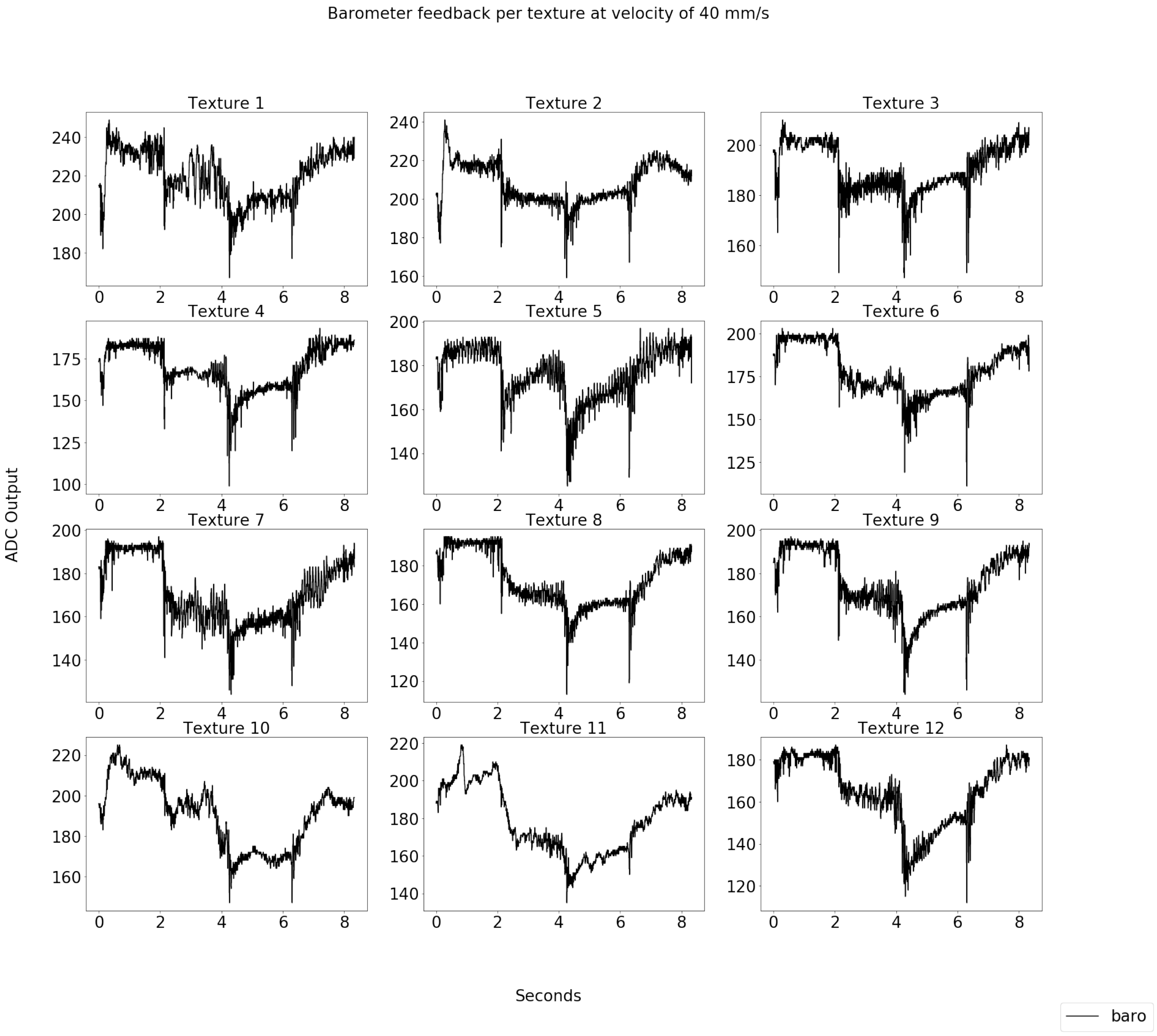

Figure A.2: Barometer data collected for each texture in a 2D dynamic exploration at an exploration velocity of 40 mm/s.

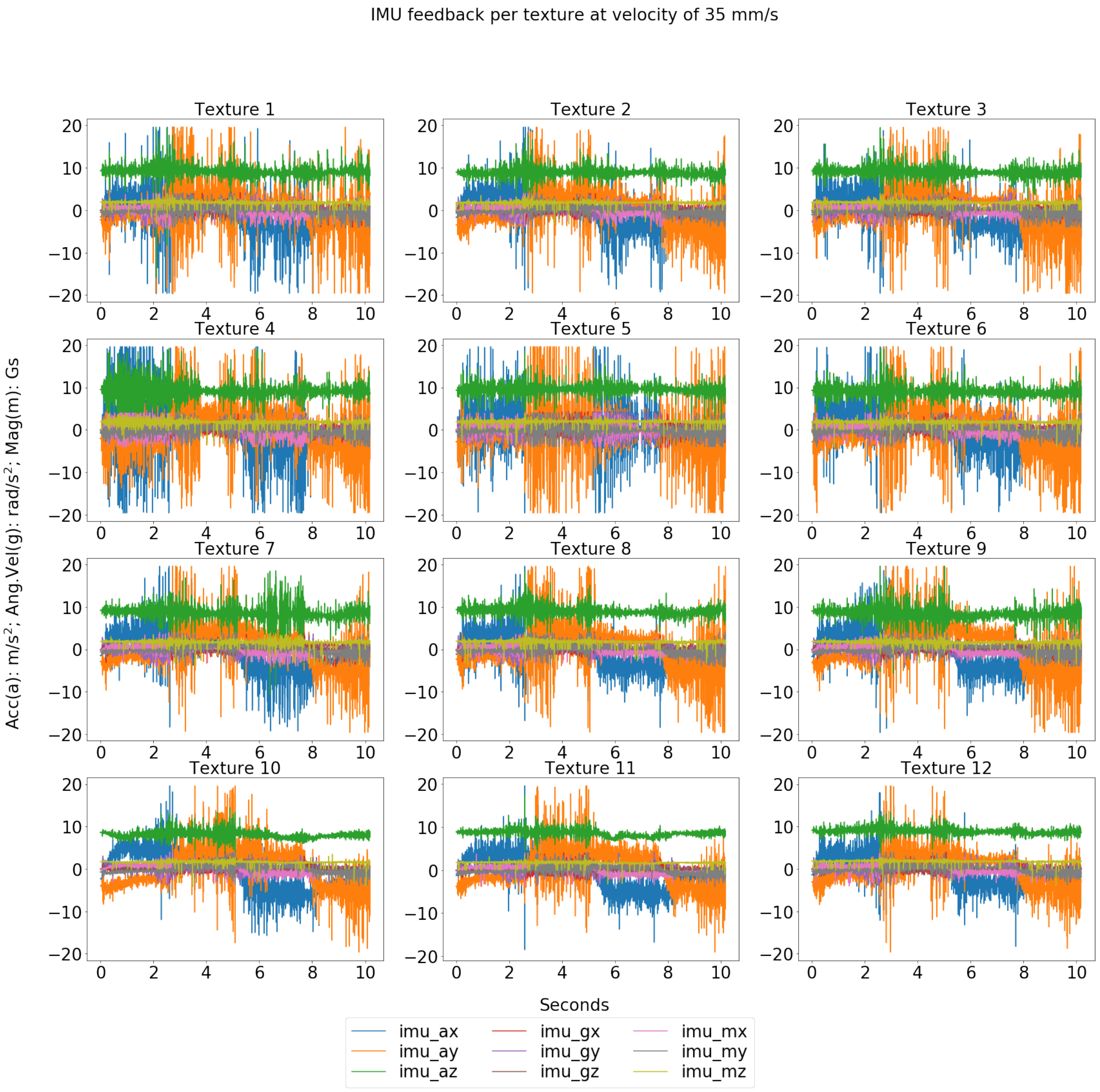

Figure A.3: IMU data collected for each texture in a 2D dynamic exploration at an exploration velocity of 35 mm/s.

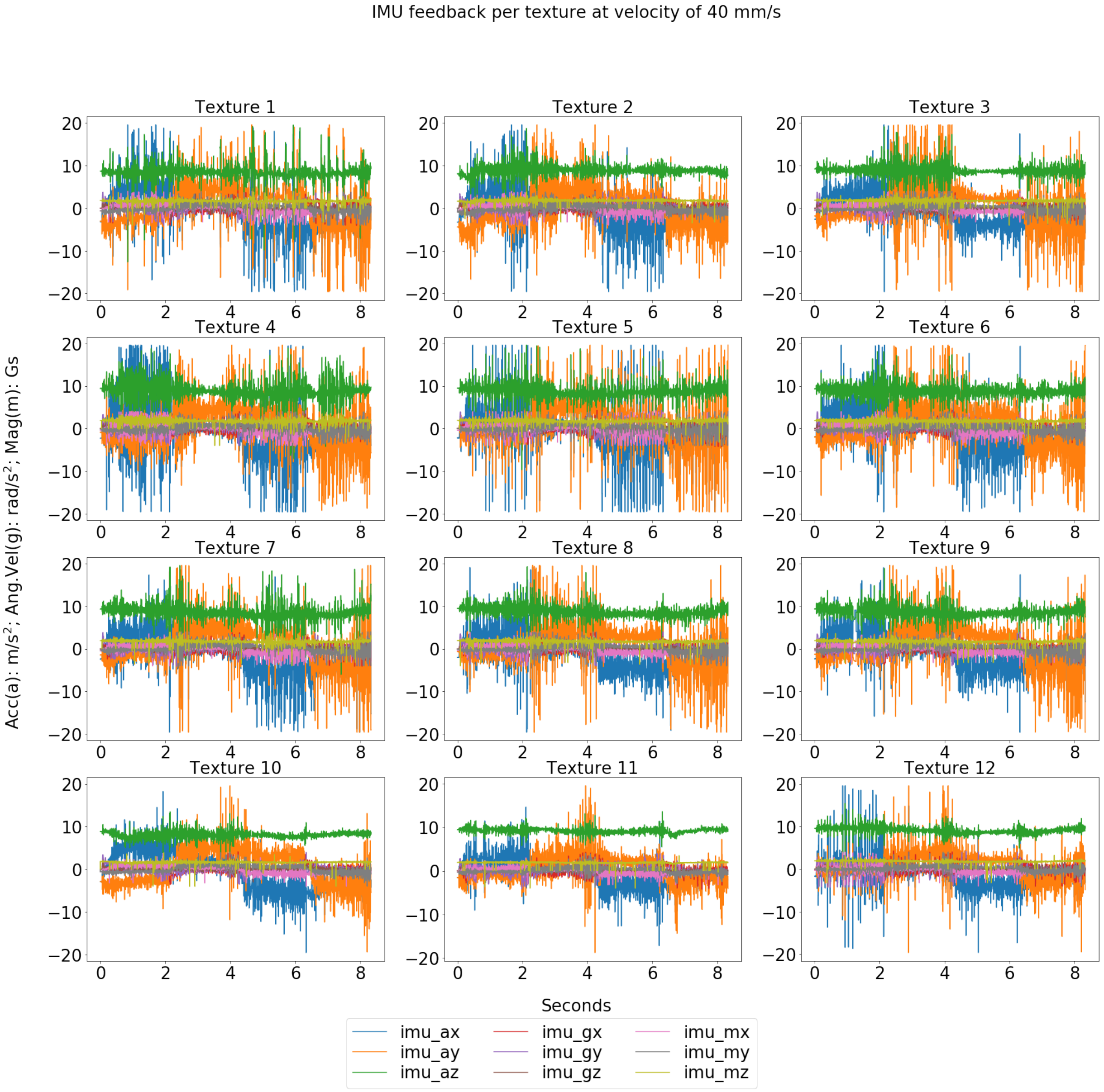

Figure A.4: IMU data collected for each texture in a 2D dynamic exploration at an exploration velocity of 40 mm/s.

References

[1] R. Sekuler and R. Balke. Touch. In *Perception*, chapter 11, pages 357–383. McGraw-Hill, 2 edition, 1990.

[2] J. C. Rothwell, M. M. Traub, B. L. Day, J. A. Obeso, P. K. Thomas, and C. D. Marsden. Manual Motor Performance in a Deafferented Man. *Brain*, 105(3):515–542, 1982.

[3] R.S. Johansson and G. Westling. Roles of Glabrous Skin Receptors and Sensorimotor Memory in Automatic Control of Precision Grip when Lifting Rougher or more Slippery Objects. *Experimental Brain Research*, 56(3), 10 1984.

[4] G. Robles-De-La-Torre. The Importance of the Sense of Touch in Virtual and Real Environments. *IEEE Multimedia*, 13(3):24–30, 7 2006.

[5] Thiago Eustaquio Alves de Oliveira, Ana-Maria Cretu, and Emil M. Petriu. Multimodal Bio-Inspired Tactile Sensing Module. *IEEE Sensors Journal*, 17(11):3231–3243, 6 2017.

[6] Bruno Monteiro Rocha Lima, Thiago Eustaquio Alves de Oliveira, Vinicius Prado da Fonseca, Qi Zhu, Miriam Goubran, Voicu Z. Groza, and Emil M. Petriu. Heart Rate Detection Using a Miniaturized Multimodal Tactile Sensor. In *2019 IEEE International Symposium on Medical Measurements and Applications (MeMeA)*, pages 1–6. IEEE, 6 2019.

[7] Bruno Monteiro Rocha Lima, Luiz Claudio Carlos Ramos Sampaio, Thiago Eustaquio Alves de Oliveira, Vinicius Prado da Fonseca, and Emil M. Petriu. Heart Rate De-

tection Using a Multimodal Tactile Sensor and a Z-score Based Peak Detection Algorithm. In *42nd Canadian Medical and Biological Engineering Conference (CMBEC)*. Canadian Medical and Biological Engineering Society (CMBES), 2019.

[8] Thiago Eustaquio Alves De Oliveira, Bruno Monteiro Rocha Lima, Ana-Maria Cretu, and Emil M. Petriu. Tactile Profile Classification Using a Multimodal MEMs-Based Sensing Module. In *Proceedings - International Electronic Conference on Sensors and Applications (ECSA)*, volume 1, page 27, Basel, 11 2016. Multidisciplinary Digital Publishing Institute.

[9] Vinicius Prado da Fonseca, Bruno Monteiro Rocha Lima, Thiago Eustaquio Alves de Oliveira, Qi Zhu, Voicu Z. Groza, and Emil M. Petriu. In-Hand Telemanipulation Using a Robotic Hand and Biology-Inspired Haptic Sensing. In *2019 IEEE International Symposium on Medical Measurements and Applications (MeMeA)*, pages 1–6. IEEE, 6 2019.

[10] Thiago Eustaquio Alves de Oliveira, Vinicius Prado da Fonseca, Bruno Monteiro Rocha Lima, Ana-Maria Cretu, and Emil M. Petriu. End-Effector Approach Flexibilization in a Surface Approximation Task Using a Bioinspired Tactile Sensing Module. In *2019 IEEE International Symposium on Robotic and Sensors Environments (ROSE)*, pages 1–6. IEEE, 6 2019.

[11] Julian F.V Vincent, Olga A Bogatyreva, Nikolaj R Bogatyrev, Adrian Bowyer, and Anja-Karina Pahl. Biomimetics: its practice and theory. *Journal of The Royal Society Interface*, 3(9):471–482, 8 2006.

[12] S. J. Lederman and R. L. Klatzky. Haptic perception: A tutorial. *Attention, Perception & Psychophysics*, 71(7):1439–1459, 10 2009.

[13] Kenneth R Boff, Lloyd Kaufman, and James P Thomas, editors. *Handbook of perception and human performance, Vol. 2: Cognitive processes and performance.* John Wiley & Sons, Oxford, England, 1986.

[14] Definition of touch - Collins English Dictionary. [Online]. Available: https://www.collinsdictionary.com/dictionary/english/touch, 2019. Accessed on: Oct. 30, 2019.

[15] Thiago Eustaquio Alves de Oliveira. *Multimodal Bioinspired Artificial Skin Module for Tactile Sensing.* PhD thesis, University of Ottawa, 2019.

[16] Siamak Najarian, Javad DargahiAli, and Abouei Mehrizi. *Artificial Tactile Sensing in Biomedical Engineering.* The McGraw-Hill Companies, Inc, 2009.

[17] Daniel Kucherhan. Tactile Feedback for Dexterous Manipulation Operations using Assistive Prosthetic Fingers. Master's thesis, University of Ottawa, 2017.

[18] Body maps in the motor cortex and somatosensory cortex of the cerebrum - Pearson Inc. [Online]. Available: http://images.slideplayer.com/14/4280670/slides/slide_23.jpg, 2013. Accessed on: Oct. 30, 2019.

[19] Randolph Blake and Robert Sekuler. *Perception.* McGraw-Hill, 5 edition, 2005.

[20] Jeremy A. Fishel. *Design and use of a biomimetic tactile microvibration sensor with human-like sensitivity and its application in texture discrimination using Bayesian exploration.* PhD thesis, University of Southern California, 2012.

[21] M. P. McKinley and V. D. OLoughlin. *Human Anatomy.* McGraw-Hill Higher Education, 2007.

[22] R. Klatzky, R. Bajcsy, and S. Lederman. Object exploration in one and two fingered robots. In *Proceedings. IEEE International Conference on Robotics and Automation*, volume 4, pages 1806–1809. Institute of Electrical and Electronics Engineers, 1987.

[23] Susan J Lederman and Roberta L Klatzky. Hand movements: A window into haptic object recognition. *Cognitive Psychology*, 19(3):342–368, 7 1987.

[24] J. Gordon Betts, Peter Desaix, Eddie Johnson, Jody E. Johnson, Oksana Korol, Dean Kruse, Brandon Poe, James A. Wise, Mark Womble, and Kelly A. Young.

The Appendicular Skeleton. In *Anatomy and Physiology*, chapter 8, pages 307–355. OpenStax, 2017.

[25] Ravinder S. Dahiya, Philipp Mittendorfer, Maurizio Valle, Gordon Cheng, and Vladimir J. Lumelsky. Directions Toward Effective Utilization of Tactile Skin: A Review. *IEEE Sensors Journal*, 13(11):4121–4138, 11 2013.

[26] Henrik I. Christensen and Gregory D. Hager. Sensing and Estimation. In *Springer Handbook of Robotics*, chapter 4, pages 87–106. Springer Berlin Heidelberg, 2008.

[27] Mark R. Cutkosky, Robert D. Howe, and William R. Provancher. Force and tactile sensors. In *Springer Handbook of Robotics*, chapter 19, pages 455–471. Springer Berlin Heidelberg, 2008.

[28] Shan Luo, Joao Bimbo, Ravinder Dahiya, and Hongbin Liu. Robotic tactile perception of object properties: A review. *Mechatronics*, 48:54–67, 12 2017.

[29] Hong Zhang and E So. Hybrid resistive tactile sensing. *IEEE Transactions on Systems, Man, and Cybernetics, Part B (Cybernetics)*, 32(1):57–65, 2 2002.

[30] Makoto Shimojo, Akio Namiki, Masatoshi Ishikawa, Ryota Makino, and Kunihiko Mabuchi. A Tactile Sensor Sheet Using Pressure Conductive Rubber With Electrical-Wires Stitched Method. *IEEE Sensors Journal*, 4(5):589–596, 10 2004.

[31] Hassan Alirezaei, Akihiko Nagakubo, and Yasuo Kuniyoshi. A highly stretchable tactile distribution sensor for smooth surfaced humanoids. In *2007 7th IEEE-RAS International Conference on Humanoid Robots*, pages 167–173. IEEE, 11 2007.

[32] Yo Kato, Toshiharu Mukai, Tomonori Hayakawa, and Tetsuyoshi Shibata. Tactile Sensor without Wire and Sensing Element in the Tactile Region Based on EIT Method. In *2007 IEEE Sensors*, pages 792–795. IEEE, 2007.

[33] David Silvera Tawil, David Rye, and Mari Velonaki. Improved Image Reconstruction for an EIT-Based Sensitive Skin With Multiple Internal Electrodes. *IEEE Transactions on Robotics*, 27(3):425–435, 6 2011.

[34] L. Chen, G. H. Chen, and L. Lu. Piezoresistive Behavior Study on Finger-Sensing Silicone Rubber/Graphite Nanosheet Nanocomposites. *Advanced Functional Materials*, 17(6):898–904, 4 2007.

[35] Z Chu, P.M Sarro, and S Middelhoek. Silicon three-axial tactile sensor. *Sensors and Actuators A: Physical*, 54(1-3):505–510, 6 1996.

[36] M. Adam, E. Vazsonyi, I. Barsony, G. Vasarhelyi, and Cs. Ducso. Three dimensional single crystalline force sensor by porous Si micromachining. In *Proceedings of IEEE Sensors*, pages 501–504. IEEE, 2004.

[37] C. Liu. Recent Developments in Polymer MEMS. *Advanced Materials*, 19(22):3783–3790, 11 2007.

[38] Hyung Kew Lee, Sun Il Chang, and Euisik Yoon. A Flexible Polymer Tactile Sensor: Fabrication and Modular Expandability for Large Area Deployment. *Journal of Microelectromechanical Systems*, 15(6):1681–1686, 12 2006.

[39] Marco Maggiali. Artificial Skin for Humanoid Robots. *Ph. D. Disseration, University of Genova*, pages 2–6, 2008.

[40] Giorgio Cannata, Marco Maggiali, Giorgio Metta, and Giulio Sandini. An embedded artificial skin for humanoid robots. In *2008 IEEE International Conference on Multisensor Fusion and Integration for Intelligent Systems*, volume 231500, pages 434–438. IEEE, 8 2008.

[41] ChiaHua Ho, Wang-Shen Su, Chih-Fan Hu, Chia-Min Lin, Weileun Fang, and Fu-Liang Yang. A flexible, highly-sensitive, and easily-fabricated carbon-nanotubes tactile sensor on polymer substrate. In *2010 10th IEEE International Conference on Solid-State and Integrated Circuit Technology*, pages 1388–1391. IEEE, 11 2010.

[42] R.S. Dahiya, A. Adami, C. Collini, and L. Lorenzelli. POSFET tactile sensing arrays using CMOS technology. *Sensors and Actuators A: Physical*, 202:226–232, 11 2013.

[43] Yoshiyuki Ohmura, Yasuo Kuniyoshi, and Akihiko Nagakubo. Conformable and scalable tactile sensor skin for curved surfaces. In *Proceedings. IEEE International Conference on Robotics and Automation (ICRA)*, pages 1348–1353. IEEE, 2006.

[44] Masahiro Ohka, Hiroaki Kobayashi, Jumpei Takata, and Yasunaga Mitsuya. Sensing Precision of an Optical Three-axis Tactile Sensor for a Robotic Finger. In *ROMAN 2006 - The 15th IEEE International Symposium on Robot and Human Interactive Communication*, pages 214–219. IEEE, 9 2006.

[45] Hanafiah Yussof, Jumpei Takata, and Masahiro Ohk. Measurement Principles of Optical Three-Axis Tactile Sensor and its Application to Robotic Fingers System. In *Sensors: Focus on Tactile Force and Stress Sensors*. InTech, 12 2008.

[46] Ravinder S. Dahiya, G. Metta, and M. Valle. Development of fingertip tactile sensing chips for humanoid robots. In *2009 IEEE International Conference on Mechatronics*, pages 1–6. IEEE, 2009.

[47] T. Nelson, R. VanDover, S. Jin, S. Hackwood, and G. Beni. Shear-sensitive magnetoresistive robotic tactile sensor. *IEEE Transactions on Magnetics*, 22(5):394–396, 9 1986.

[48] Lorenzo Jamone, Lorenzo Natale, Giorgio Metta, and Giulio Sandini. Highly Sensitive Soft Tactile Sensors for an Anthropomorphic Robotic Hand. *IEEE Sensors Journal*, 15(8):4226–4233, 8 2015.

[49] Kiyoshi Sawahata, Jian Ping Gong, and Yoshihito Osada. Soft and wet touch-sensing system made of hydrogel. *Macromolecular Rapid Communications*, 16(10):713–716, 10 1995.

[50] T. Someya, T. Sekitani, S. Iba, Y. Kato, H. Kawaguchi, and T. Sakurai. A large-area, flexible pressure sensor matrix with organic field-effect transistors for artificial skin applications. *Proceedings of the National Academy of Sciences*, 101(27):9966–9970, 7 2004.

[51] S. Ando, H. Shinoda, A. Yonenaga, and J. Terao. Ultrasonic six-axis deformation sensing. *IEEE Transactions on Ultrasonics, Ferroelectrics and Frequency Control*, 48(4):1031–1045, 7 2001.

[52] H. Shinoda, K. Matsumoto, and S. Ando. Tactile sensing based on acoustic resonance tensor cell. In *Proceedings of International Solid State Sensors and Actuators Conference (Transducers '97)*, volume 1, pages 129–132. IEEE, 1997.

[53] A. Bonfiglio, D. DeRossi, T. Kirstein, I.R. Locher, F. Mameli, R. Paradiso, and G. Vozzi. Organic Field Effect Transistors for Textile Applications. *IEEE Transactions on Information Technology in Biomedicine*, 9(3):319–324, 9 2005.

[54] J. Dargahi, M. Parameswaran, and S. Payandeh. A micromachined piezoelectric tactile sensor for an endoscopic grasper-theory, fabrication and experiments. *Journal of Microelectromechanical Systems*, 9(3):329–335, 9 2000.

[55] Paolo Dario and Giorgio Buttazzo. An Anthropomorphic Robot Finger for Investigating Artificial Tactile Perception. *The International Journal of Robotics Research*, 6(3):25–48, 9 1987.

[56] Koh Hosoda, Yasunori Tada, and Minoru Asada. Anthropomorphic robotic soft fingertip with randomly distributed receptors. *Robotics and Autonomous Systems*, 54(2):104–109, 2 2006.

[57] G.L. Kenaley and M.R. Cutkosky. Electrorheological fluid-based robotic fingers with tactile sensing. In *Proceedings, International Conference on Robotics and Automation*, pages 132–136. IEEE Comput. Soc. Press, 1989.

[58] R.M. Voyles, G. Fedder, and P.K. Khosla. Design of a modular tactile sensor and actuator based on an electrorheological gel. In *Proceedings of IEEE International Conference on Robotics and Automation*, volume 1, pages 13–17. IEEE, 1996.

[59] E.P. Scilingo, N. Sgambelluri, D. De Rossi, and A. Bicchi. Haptic displays based on magnetorheological fluids: design, realization and psychophysical validation. In *11th*

Symposium on Haptic Interfaces for Virtual Environment and Teleoperator Systems. IEEE Comput. Soc, 2003.

[60] Interlink. FSR 402. [Online]. Available: https://www.interlinkelectronics.com/fsr-402, 2019. Accessed on: Oct. 30, 2019.

[61] Tekscan. Pressure Mapping, Force Measurement and Tactile Sensors. [Online]. Available: https://www.tekscan.com/product-group/embedded-sensing/force-sensors, 2019. Accessed on: Oct. 30, 2019.

[62] Peratech. SP200-10. [Online]. Available: https://www.peratech.com/what-is-qtc.html, 2019. Accessed on: Oct. 30, 2019.

[63] Ravinder S. Dahiya and Maurizio Valle. *Robotic Tactile Sensing.* Springer Netherlands, Dordrecht, 2013.

[64] PPS. Case Study: Capacitive Tactile Sensors In Robotics. [Online]. Available: https://pressureprofile.com/oem-robotics#twendy-one, 2016. Accessed on: Oct. 30, 2019.

[65] SynTouch. SynTouch Announces the BioTac SP. [Online]. Available: https://www.syntouchinc.com/en/syntouch-announces-the-biotac-sp/, 2019. Accessed on: Oct. 30, 2019.

[66] Sina Youssefian, Nima Rahbar, and Eduardo Torres-Jara. Contact Behavior of Soft Spherical Tactile Sensors. *IEEE Sensors Journal*, 14(5):1435–1442, 5 2014.

[67] W.C. Nowlin. Experimental results on Bayesian algorithms for interpreting compliant tactile sensing data. In *Proceedings IEEE International Conference on Robotics and Automation*, pages 378–383. IEEE Comput. Soc. Press, 1991.

[68] Janmenjoy Nayak, Bighnaraj Naik, and H. S. Behera. A Comprehensive Survey on Support Vector Machine in Data Mining Tasks: Applications & Challenges. *International Journal of Database Theory and Application*, 8(1):169–186, 2 2015.

[69] H. Gish. A probabilistic approach to the understanding and training of neural network classifiers. In *International Conference on Acoustics, Speech, and Signal Processing*, pages 1361–1364. IEEE, 1990.

[70] G P Zhang. Neural networks for classification: a survey. *IEEE Transactions on Systems, Man, and Cybernetics, Part C (Applications and Reviews)*, 30(4):451–462, 11 2000.

[71] Donald Michie, D J Spiegelhalter, C C Taylor, and John Campbell, editors. *Machine Learning, Neural and Statistical Classification.* Ellis Horwood, Upper Saddle River, NJ, USA, 1994.

[72] Desmond Fletcher and Ernie Goss. Forecasting with neural networks: An application using bankruptcy data. *Information & Management*, 24(3):159–167, 3 1993.

[73] J.T. Connor, R.D. Martin, and L.E. Atlas. Recurrent neural networks and robust time series prediction. *IEEE Transactions on Neural Networks*, 5(2):240–254, 3 1994.

[74] Wilpen L. Gorr. Editorial: Research prospective on neural network forecasting. *International Journal of Forecasting*, 10(1):1–4, 6 1994.

[75] M. Cottrell, B. Girard, Y. Girard, M. Mangeas, and C. Muller. Neural modeling for time series: A statistical stepwise method for weight elimination. *IEEE Transactions on Neural Networks*, 6(6):1355–1364, 1995.

[76] Keith B. Church and Stephen P. Curram. Forecasting consumers' expenditure: A comparison between econometric and neural network models. *International Journal of Forecasting*, 12(2):255–267, 6 1996.

[77] Jeffrey L Callen, Clarence C.Y Kwan, Patrick C.Y Yip, and Yufei Yuan. Neural network forecasting of quarterly accounting earnings. *International Journal of Forecasting*, 12(4):475–482, 12 1996.

[78] Monica Adya and Fred Collopy. How effective are neural networks at forecasting and prediction? A review and evaluation. *Journal of Forecasting*, 17(5-6):481–495, 9 1998.

[79] Julian J Faraway. Time series forecasting with neural networks : a comparative study using the airline data. In *Applied Statististic*, 1998.

[80] H.S. Hippert, C.E. Pedreira, and R.C. Souza. Neural networks for short-term load forecasting: a review and evaluation. *IEEE Transactions on Power Systems*, 16(1):44–55, 2001.

[81] Seyed M. Hosseini-Nezhad, Toyoko S. Yamashita, Roger A. Bielefeld, Steven E. Krug, and Yoh-Han Pao. A Neural Network Approach for the Determination of Interhospital Transport Mode. *Computers and Biomedical Research*, 28(4):319–334, 8 1995.

[82] L G Portney and M P Watkins. *Foundations of Clinical Research: Applications to Practice*. F. A. Davis Company, 2015.

[83] P J G Lisboa. A review of evidence of health benefit from artificial neural networks in medical intervention. *Neural networks : the official journal of the International Neural Network Society*, 15(1):11–39, 1 2002.

[84] Rainer Osswald and Wiebke Petersen. A Logical Approach to Data-Driven Classification. In *Advances in Artificial Intelligence*, pages 267–281. Springer, 2003.

[85] S. Sumathi and S. N. Sivanandam. Data Mining Tasks, Techniques, and Applications. In *Introduction to Data Mining and its Applications*, pages 195–216. Springer Berlin Heidelberg, Berlin, Heidelberg, 2006.

[86] Vladimir Naumovich Vapnik. *Statistical learning theory*. Wiley, 1998.

[87] Corinna Cortes and Vladimir Vapnik. Support-vector networks. *Machine Learning*, 20(3):273–297, 9 1995.

[88] Scikit-Learn. Scikit-learn: Machine Learning in Python. [Online]. Available: `https://scikit-learn.org/stable/index.html`, 2019. Accessed on: Oct. 30, 2019.

[89] Shutao Li, James T. Kwok, Hailong Zhu, and Yaonan Wang. Texture classification using the support vector machines. *Pattern Recognition*, 36(12):2883–2893, 12 2003.

[90] Chih-Fong Tsai. Training support vector machines based on stacked generalization for image classification. *Neurocomputing*, 64:497–503, 3 2005.

[91] Jin-Hyuk Hong, Jun-Ki Min, Ung-Keun Cho, and Sung-Bae Cho. Fingerprint classification using one-vs-all support vector machines dynamically ordered with nave Bayes classifiers. *Pattern Recognition*, 41(2):662–671, 2 2008.

[92] Wen Zhang, Taketoshi Yoshida, and Xijin Tang. Text classification based on multi-word with support vector machine. *Knowledge-Based Systems*, 21(8):879–886, 12 2008.

[93] Chin Heng Wan, Lam Hong Lee, Rajprasad Rajkumar, and Dino Isa. A hybrid text classification approach with low dependency on parameter by integrating K-nearest neighbor and support vector machine. *Expert Systems with Applications*, 39(15):11880–11888, 11 2012.

[94] Yiqiang Zhan and Dinggang Shen. Design efficient support vector machine for fast classification. *Pattern Recognition*, 38(1):157–161, 1 2005.

[95] Yuchun Tang, Bo Jin, Yi Sun, and Yan-Qing Zhang. Granular support vector machines for medical binary classification problems. In *IEEE International Geoscience and Remote Sensing (IGARSS)*, pages 73–78. IEEE, 2004.

[96] Bo-Suk Yang, Won-Woo Hwang, Dong-Jo Kim, and Andy Chit Tan. Condition classification of small reciprocating compressor for refrigerators using artificial neural networks and support vector machines. *Mechanical Systems and Signal Processing*, 19(2):371–390, 3 2005.

[97] Rung-Ching Chen and Chung-Hsun Hsieh. Web page classification based on a support vector machine using a weighted vote schema. *Expert Systems with Applications*, 31(2):427–435, 8 2006.

[98] Xulei Yang, Qing Song, and A. Cao. Weighted support vector machine for data classification. In *Proceedings. IEEE International Joint Conference on Neural Networks*, volume 2, pages 859–864. IEEE, 2005.

[99] Chin-Teng Lin, Chang-Mao Yeh, Sheng-Fu Liang, Jen-Feng Chung, and N. Kumar. Support-vector-based fuzzy neural network for pattern classification. *IEEE Transactions on Fuzzy Systems*, 14(1):31–41, 2 2006.

[100] Sandeep Chaplot, L.M. Patnaik, and N.R. Jagannathan. Classification of magnetic resonance brain images using wavelets as input to support vector machine and neural network. *Biomedical Signal Processing and Control*, 1(1):86–92, 1 2006.

[101] Kemal Polat and Salih Güneş. Breast cancer diagnosis using least square support vector machine. *Digital Signal Processing*, 17(4):694–701, 7 2007.

[102] Scikit-Learn. Support Vector Machines. [Online]. Available: `https://scikit-learn.org/stable/modules/svm.html`, 2019. Accessed on: Oct. 30, 2019.

[103] Robert J. Schalkoff. *Pattern Recognition: Statistical, Structural, and Neural Approaches*. John Wiley & Sons, 1992.

[104] Kurt Hornik, Maxwell Stinchcombe, and Halbert White. Multilayer feedforward networks are universal approximators. *Neural Networks*, 2(5):359–366, 1 1989.

[105] M.W Gardner and S.R Dorling. Artificial neural networks (the multilayer perceptron)a review of applications in the atmospheric sciences. *Atmospheric Environment*, 32(14-15):2627–2636, 8 1998.

[106] Scikit-Learn. Neural network models (supervised). [Online]. Available: `https://scikit-learn.org/stable/modules/neural_networks_supervised.html#multi-layer-perceptron`, 2019. Accessed on: Oct. 30, 2019.

[107] Pooja Rani. A Review of various KNN Techniques. *International Journal for Research in Applied Science and Engineering Technology*, V(VIII):1174–1179, 8 2017.

[108] R. W. Hamming. Error Detecting and Error Correcting Codes. *Bell System Technical Journal*, 29(2):147–160, 4 1950.

[109] Leif Peterson. K-nearest neighbor. *Scholarpedia*, 4(2), 2009.

[110] Scikit-Learn. Decision Trees. [Online]. Available: https://scikit-learn.org/stable/modules/tree.html, 2019. Accessed on: Oct. 30, 2019.

[111] Andy Liaw, Matthew Wiener, and others. Classification and regression by randomForest. *R news*, 2(3):18–22, 2002.

[112] Gilles Louppe. *Understanding Random Forests: From Theory to Practice*. PhD thesis, University of Liège, 2014.

[113] Scikit-Learn. Random Forest Classifier. [Online]. Available: https://scikit-learn.org/stable/modules/generated/sklearn.ensemble.RandomForestClassifier.html. Accessed on: Oct. 30, 2019.

[114] Pierre Geurts, Damien Ernst, and Louis Wehenkel. Extremely randomized trees. *Machine Learning*, 63(1):3–42, 4 2006.

[115] S. Ballesteros, J.M. Reales, L. Ponce de Leon, and B. Garcia. The Perception of Ecological Textures by Touch: Does the Perceptual Space Change under Bimodal Visual and Haptic Exploration? In *First Joint Eurohaptics Conference and Symposium on Haptic Interfaces for Virtual Environment and Teleoperator Systems*, pages 635–638. IEEE, 2005.

[116] Thiago Eustaquio Alves De Oliveira, Ana Maria Cretu, Vinicius Prado Da Fonseca, and Emil M. Petriu. Touch sensing for humanoid robots. *IEEE Instrumentation and Measurement Magazine*, 18(5):13–19, 2015.

[117] S.K. Yeung, E.M. Petriu, W.S. McMath, and D.C. Petriu. High sampling resolution tactile sensor for object recognition. *IEEE Transactions on Instrumentation and Measurement*, 43(2):277–282, 4 1994.

[118] Thiago Alves de Oliveira, Ana-Maria Cretu, and Emil Petriu. Multimodal Bio-Inspired Tactile Sensing Module for Surface Characterization. *Sensors*, 17(6), 5 2017.

[119] S.G. Mallat. A theory for multiresolution signal decomposition: the wavelet representation. *IEEE Transactions on Pattern Analysis and Machine Intelligence*, 11(7):674–693, 7 1989.

[120] Rasmus Bro and Age K. Smilde. Principal component analysis. *Anal. Methods*, 6(9):2812–2831, 2014.

[121] P Giguere and G Dudek. A Simple Tactile Probe for Surface Identification by Mobile Robots. *IEEE Transactions on Robotics*, 27(3):534–544, 6 2011.

[122] Ian T. Nabney. *NETLAB: Algorithms for Pattern Recognition*. Springer-Verlag, New York, 2002.

[123] Patrick Dallaire, Philippe Giguère, Daniel Émond, and Brahim Chaib-draa. Autonomous tactile perception: A combined improved sensing and Bayesian nonparametric approach. *Robotics and Autonomous Systems*, 62(4):422–435, 4 2014.

[124] Chih-Chung Chang and Chih-Jen Lin. LIBSVM – A Library for Support Vector Machines. [Online]. Available: `https://www.csie.ntu.edu.tw/~cjlin/libsvm/`, 2019. Accessed on: Oct. 30, 2019.

[125] J Sinapov, V Sukhoy, R Sahai, and A Stoytchev. Vibrotactile Recognition and Categorization of Surfaces by a Humanoid Robot. *IEEE Transactions on Robotics*, 27(3):488–497, 6 2011.

[126] Ian H. Witten, Eibe Frank, and Mark A. Hall. Introduction to Weka. In *Data Mining: Practical Machine Learning Tools and Techniques*. Elsevier, 2011.

[127] Jivko Sinapov and Alexander Stoytchev. The Boosting Effect of Exploratory Behaviors. In *Proceedings of the Twenty-Fourth Conference on Artificial Intelligence (AAAI)*, pages 1–6. Twenty-Fourth AAAI Conference on Artificial Intelligence, 2010.

[128] Florian de Boissieu, Christelle Godin, Bernard Guilhamat, Dominique David, Christine Servière, and Daniel Baudois. Tactile texture recognition with a 3-axial force

MEMS integrated artificial finger. In *Proceedings in Robotics: Science and Systems*, 2009.

[129] Damith Suresh Chathuranga, Van Anh Ho, and Shinichi Hirai. Investigation of a biomimetic fingertip's ability to discriminate fabrics based on surface textures. In *2013 IEEE/ASME International Conference on Advanced Intelligent Mechatronics*, pages 1667–1674. IEEE, 7 2013.

[130] C M Oddo, M Controzzi, L Beccai, C Cipriani, and M C Carrozza. Roughness Encoding for Discrimination of Surfaces in Artificial Active-Touch. *IEEE Transactions on Robotics*, 27(3):522–533, 6 2011.

[131] N Jamali and C Sammut. Majority Voting: Material Classification by Tactile Sensing Using Surface Texture. *IEEE Transactions on Robotics*, 27(3):508–521, 6 2011.

[132] A. Gómez Eguíluz, I. Rañó, S.A. Coleman, and T.M. McGinnity. Multimodal Material identification through recursive tactile sensing. *Robotics and Autonomous Systems*, 106:130–139, 8 2018.

[133] J. Gordon Betts, Peter Desaix, Eddie Johnson, Jody E. Johnson, Oksana Korol, Dean Kruse, Brandon Poe, James A. Wise, Mark Womble, and Kelly A. Young. The Cardiovascular System: The Heart. In *Anatomy and Physiology*, chapter 19, page 1410. OpenStax, 2017.

[134] Marek Malik. Heart Rate Variability. *Annals of Noninvasive Electrocardiology*, 1(2):151–181, 4 1996.

[135] Jorge Armony and Patrik Vuilleumier. *The Cambridge handbook of human affective neuroscience*. Cambridge University Press, 2013.

[136] John Allen. Photoplethysmography and its application in clinical physiological measurement. *Physiological Measurement*, 28(3):R1–R39, 3 2007.

[137] J. Dawson, C. Kamlin, C. Wong, A. te Pas, M. Vento, T. Cole, S. Donath, S. Hooper, P. Davis, and C. Morley. Changes in heart rate in the first minutes after birth.

Archives of Disease in Childhood - Fetal and Neonatal Edition, 95(3):F177–F181, 5 2010.

[138] M Sekine and K Maeno. Non-contact heart rate detection using periodic variation in Doppler frequency. In *2011 IEEE Sensors Applications Symposium*, pages 318–322, 2 2011.

[139] W Hu, Z Zhao, Y Wang, H Zhang, and F Lin. Noncontact Accurate Measurement of Cardiopulmonary Activity Using a Compact Quadrature Doppler Radar Sensor. *IEEE Transactions on Biomedical Engineering*, 61(3):725–735, 3 2014.

[140] S Zaunseder, A Heinke, A Trumpp, and H Malberg. Heart beat detection and analysis from videos. In *2014 IEEE 34th International Scientific Conference on Electronics and Nanotechnology (ELNANO)*, pages 286–290, 4 2014.

[141] Hui-Sup Cho and Young-Jin Park. Detection of Heart Rate through a Wall Using UWB Impulse Radar. *Journal of Healthcare Engineering*, 2018:1–7, 2018.

[142] Bruno Siciliano and Oussama Khatib. *Springer Handbook of Robotics*. Springer-Verlag, Berlin, Heidelberg, 2007.

[143] Morgan Quigley, Ken Conley, Brian P Gerkey, Josh Faust, Tully Foote, Jeremy Leibs, Rob Wheeler, and Andrew Y Ng. ROS: an open-source Robot Operating System. In *ICRA Workshop on Open Source Software*, 2009.

[144] Lovely Chhabra, Narender Goel, Laxman Prajapat, David H. Spodick, and Sanjeev Goyal. Mouse Heart Rate in a Human: Diagnostic Mystery of an Extreme Tachyarrhythmia. *Indian Pacing and Electrophysiology Journal*, 12(1):32–35, 1 2012.

[145] J-P.V. Brakel. Peak signal detection in realtime timeseries data - Robust peak detection algorithm (using z-scores). [Online]. Available: `https://stackoverflow.com/questions/22583391/peak-signal-detection-in-realtime-timeseries-data/2264036222640362-2014`, 2014. Accessed on: Oct. 30, 2019.

[146] M C Catalbas, T Cegovnik, J Sodnik, and A Gulten. Driver fatigue detection based on saccadic eye movements. In *2017 10th International Conference on Electrical and Electronics Engineering (ELECO)*, pages 913–917, 11 2017.

[147] Carleton University. Policy on the Responsible Conduct of Research. [Online]. Available: `https://carleton.ca/researchethics/wp-content/uploads/Responsible-Conduct-of-Research..pdf`, 2014. Accessed on: Oct. 30, 2019.

[148] David Katz and Lester E. Krueger. *The World of Touch*. Psychology Press, New York, 5 1989.

[149] Gerald E. Loeb, George A. Tsianos, Jeremy A. Fishel, Nicholas Wettels, and Stefan Schaal. Understanding haptics by evolving mechatronic systems. In *Progress in Brain Research*. Elsevier, 2011.

[150] Susan J Lederman and Roberta L Klatzky. Hand movements: A window into haptic object recognition. *Cognitive Psychology*, 19(3):342–368, 7 1987.

[151] Mark Hollins and S Ryan Risner. Evidence for the duplex theory of tactile texture perception. *Perception & Psychophysics*, 62(4):695–705, 1 2000.

[152] Mark Hollins, Richard Faldowski, Suman Rao, and Forrest Young. Perceptual dimensions of tactile surface texture: A multidimensional scaling analysis. *Perception & Psychophysics*, 54(6):697–705, 11 1993.

[153] Jeremy A. Fishel and Gerald E. Loeb. Bayesian exploration for intelligent identification of textures. *Frontiers in Neurorobotics*, 6:1–20, 2012.